Title

Nanoscale Chemical Interrogation of Surfaces using Tip-Enhanced Near-field Optical Microscopy

Author

Hermann, Richard

Publication Date

2018

UNIVERSITY OF CALIFORNIA

Santa Barbara

Nanoscale Chemical Interrogation of Surfaces using Tip-Enhanced Near-field Optical Microscopy

A dissertation submitted in partial satisfaction of the
requirements for the degree Doctor of Philosophy
in Chemical Engineering

by

Richard James Hermann

Committee in charge:
Professor Michael J. Gordon, Chair
Professor Michael Doherty
Professor Matt Helgeson
Professor Horia Metiu

September 2018

The dissertation of Richard James Hermann is approved.

Michael Doherty

Matthew Helgeson

Horia Metiu

Michael J. Gordon, Committee Chair

September 2018

ACKNOWLEDGEMENTS

I'd like to start by acknowledging the person who's had the biggest impact on my graduate career and on my growth as a scientist: Mike Gordon. When I first considered joining the Gordon group in 2013, I was immediately struck by two things: the shear amount of stuff packed into one laboratory, and the enthusiasm Mike had for working directly with students in that chaotic space. That enthusiasm has never wavered, and I have benefited from it in too many ways to count over the past five years. The attention to detail across all our work together has been invaluable in helping me advance as a technical writer and speaker. Mike, for all the late nights and weekends working with me, and all the other nights out with the group paying more than your fair share of the tab, thank you!

I'd also like to acknowledge the other Gordonites (past and present) who have helped make my time in lab feel more like fun and less like work. The social environment of this group is special, and is continuously reinforced through our lunches, dinners, and beach barbeques. In particular, I'd like to thank Isaac Riisness for designing many of the core components of the near-field microscope used in this work and for writing a detailed instruction manual on its operation. Those efforts gave me a head start on this project and allowed successful experimental results to start coming in by the time candidacy arrived. Thanks as well to Alex Heilman for helping me get up to speed on all things TERS and optics related, and for being a great friend and coworker in the optics corner for more than three years.

As for all the other friends I've made in Santa Barbara, I don't know how I got lucky enough to find a group like this, but I'm incredibly thankful for it. The memories we've made on trips together, or just at Hollister on a Friday night, are irreplaceable. Regardless of the ups and downs of grad school, being surrounded by compassionate, intelligent, and motivated friends has kept me grounded and focused on the most important things in life. I'm excited to see what our next adventures have in store and look forward to future visits and reunions as we disperse around the country and start new careers.

I would also like to thank the Dow Chemical Company for their direct support of this work via a Dow Discovery Fellowship awarded through the Chemical Engineering department. This fellowship supported my research from 2015-2018 and gave me the freedom to take on some of the fundamental challenges associated with near-field microscopy techniques.

Last, but not least, my parents. They have supported me with love and interest in all of my academic and life pursuits. Five years ago, the three of us loaded my car with everything that would fit and made the trip from Minnesota to Santa Barbara together. Being halfway across the country hasn't stopped them from coming back for a visit every year. We've had great times golfing, wine tasting, and scarfing down seafood. Thank you to them and to my grandparents for making one more trip to Santa Barbara to support me on the day of my defense; it means the world to me.

VITA OF RICHARD JAMES HERMANN

EDUCATION

Doctor of Philosophy in Chemical Engineering, University of California, Santa Barbara, September 2018 (expected)
Bachelor of Chemical Engineering, University of Minnesota, Twin Cities, May 2013
Bachelor of Chemistry, University of Minnesota, Twin Cities, May 2013

PROFESSIONAL EMPLOYMENT

2014-2017: Teaching Assistant, Department of Chemical Engineering, University of California, Santa Barbara
2011-2013: Research Assistant, Dept. of Chem. Eng. and Mat. Sci., University of Minnesota

PUBLICATIONS

[1] R. J. Hermann and M. J. Gordon, “Rational design of localized surface plasmon resonances in optical near-field probes”, submitted to *Optics Express,* Aug. 2018.

[2] R. J. Hermann and M. J. Gordon, “Using physically relevant minimum length scales to predict local field enhancements of plasmonic nanoparticle dimers”, submitted to *ACS Applied Nano Materials*, July 2018.

[3] R. J. Hermann and M. J. Gordon, “Imaging intermolecular exciton coupling in metal-free phthalocyanine nanofilms using tip-enhanced near-field optical microscopy”, *J. Phys. Chem. C*, 2018, vol. 122, pgs. 14796-14804.

[4] R. J. Hermann and M. J. Gordon, “Nanoscale Optical Microscopy and Spectroscopy Using Near-Field Probes”, *Annual Review of Chemical and Biomolecular Engineering*, 2018, vol. 9, pgs. 365-387.

[5] R. J. Hermann and M. J. Gordon, “Sub-diffraction limited chemical imaging of patterned phthalocyanine films using tip-enhanced near-field optical microscopy”, *J. Raman Spec.*, 2016, vol. 47, pgs. 1287–1292.

[6] S. D. Blass, R. J. Hermann, N. E. Persson, A. Bhan, Lanny D. Schmidt, "Conversion of glycerol to light olefins and gasoline precursors", *Applied Catalysis A: General*, 2014, vol. 475, pgs. 10-15.

[7] A. R. Teixeira, R. J. Hermann, W. J. Suszynski, L. D. Schmidt, D. P. Schmidt, and P. J. Dauenhauer, "Microexplosions in evaporation of biomass-derived pyrolysis oils and the effects of simple fuel processing", *ACS Sustainable Chemistry & Engineering*, 2013, vol. 1, pgs. 341-348.

[8] J. S. Kruger, R. Chakrabarti, R. J. Hermann, and L. D. Schmidt, "Autothermal partial oxidation of butanol isomers", *Applied Catalysis A: General*, 2012, vol. 411-412, pgs. 87-94.

[9] R. Chakrabarti, J. S. Kruger, R. J. Hermann, and L. D. Schmidt, "Autothermal reforming of isobutanol", *RSC Advances*, 2012, vol. 2, pgs. 2527-2533.

AWARDS

DOW Chemical Company graduate student fellowship	2015-2018
Best talk award at Clorox-Amgen Graduate Student Symposium	2017
University of Minnesota Honors Program	2009-2013
National Merit Scholarship Corporation Finalist	2009

ABSTRACT

Nanoscale Chemical Interrogation of Surfaces using Tip-Enhanced Near-field Optical Microscopy

by

Richard James Hermann

As our ability to engineer, design, and modify nanoscale systems continues to advance, characterization methods must keep pace. Light-matter interactions, in particular optical spectroscopy, provide a wealth of information on the vibrational and electronic structure of matter and can be directly related to physical properties such as phase, chemistry, charge transport, etc. However, the fundamental wave-like nature of light prevents radiation from being focused to arbitrarily small length scales using traditional optics. This is known as the diffraction limit, and is on the order of several hundred nanometers for optical wavelengths (~λ/2). One method of overcoming diffraction is to couple light to nanostructures (e.g., optical antennae) that support resonant oscillations of conduction electrons (plasmons). These charge oscillations generate intense optical fields that are spatially controlled by the antenna size, rather than the radiation wavelength. The set of related techniques utilizing nanoscale optical antennae to interrogate and image surfaces are known as tip-enhanced near-field optical microscopy (TENOM).

This work details the design, construction, and experimental validation of a TENOM instrument, and demonstrates specific applications in near-field spectroscopy and super-resolution chemical imaging. A commercial inverted optical microscope was integrated with

a custom-built shear-force atomic force microscope (AFM). The inverted microscope geometry enables high excitation and collection efficiency of light from the antenna apex, while the shear-force AFM ensures the antenna is always positioned at the sample surface, allowing analytes to interact with the locally enhanced optical fields. Experimental validation of the completed TENOM instrument was accomplished using both copper (CuPc) and metal-free phthalocyanine (H_2Pc) species. Chemical images of patterned CuPc and H_2Pc were obtained with lateral spatial resolutions below 50 nm ($<\lambda/10$), unambiguously demonstrating the super-resolution capabilities of the instrument. Multimode imaging of H_2Pc was performed with simultaneous collection of spatially correlated fluorescence, Raman, and topographic data. The combination of these measurements allowed nanoscale mapping of the H_2Pc aggregation state across a wide range of surface coverages, including isolated molecules, molecular dimers, and continuous films.

Additionally, finite-difference time-domain (FDTD) optical simulations were used to study the fundamental physics of plasmonic optical antennae relevant for near-field spectroscopy. For TENOM applications, tuning the optical properties of support structures with attached plasmonic nanocavities was shown to be critical for either enhancing or quenching local electric field strengths. Support structures with low extinction coefficients were found to produce the largest field enhancements, with the refractive index of the material being further tuned to optimize antenna performance as a function of the specific geometry considered. A quantitative comparison of several antenna designs was carried out, which has not been possible experimentally due to the low reproducibility of nanostructure fabrication procedures and variability in methods of measuring local optical fields. Two promising architectures were identified that both involve focused ion-beam milling a groove near the antenna apex. Methods of tuning the resonance energy of these structures over the full visible spectrum, using different plasmonic metals (Au/Ag) and by varying the groove positions relative to the apex, were also demonstrated.

FDTD simulations were also used to study pairs of plasmonic nanoparticles relevant for surface-enhanced Raman spectroscopy applications. Previous work on this system was shown to significantly overestimate field enhancements due to numerical effects present at nano-gap features. Metal bridging structures were used to halt the field divergence at physically relevant lengths scales, allowing accurate study of experimentally relevant parameters including the fused contact area and presence of a dielectric encapsulation layer. It was found that fused dimer antennae are capable of producing large enhancements at infrared energies, but may be challenging to reproducibly fabricate due to the high sensitivity of the supported plasmon resonances to changes in local morphology.

Advancements across multiple scientific and engineering disciplines are helping push the TENOM technique forward. Improvements in high-intensity broadband laser sources will enable flexible measurement of both the electronic and vibrational structure of materials, and general improvements in nano-manufacturing are expected to reduce the time and cost of producing high-enhancement resonant antennae with well-defined plasmonic structure. The future is bright for TENOM to find use as a versatile optical and physical surface characterization technique.

TABLE OF CONTENTS

LIST OF FIGURES

Chapter I. Introduction to Scanning Near-field Optical Microscopy

Adapted from: R. J. Hermann and M. J. Gordon, “Nanoscale Optical Microscopy and Spectroscopy Using Near-Field Probes”, *Annual Review of Chemical and Biomolecular Engineering*, 2018, vol. 9, pgs. 365-387.

Abstract

Light-matter interactions can provide a wealth of detailed information about the structural, electronic, optical, and chemical properties of materials through various excitation and scattering processes that occur over different length, energy, and timescales. Unfortunately, the wavelike nature of light limits the achievable spatial resolution for interrogation and imaging of materials to roughly λ/2 because of diffraction. Scanning near-field optical microscopy (SNOM) breaks this diffraction limit by coupling light to nanostructures that are specifically designed to manipulate, enhance, and/or extract optical signals from very small regions of space. Progress in the SNOM field over the past 30 years has led to the development of many methods to optically characterize materials at lateral spatial resolutions well below 100 nm. We review these exciting developments and demonstrate how SNOM is truly extending optical imaging and spectroscopy to the nanoscale.

Scanning near-field optical microscopy (SNOM), also commonly permuted as NSOM, is an umbrella term for methods and instrumentation that combine high-resolution, submicron-scale spatial imaging of a material surface with some form of simultaneous optical interrogation to extract physicochemical information at a local level. Because light can interact with matter over different length, energy, and timescales, there are many ways to gather structural, optical, electronic, and chemical information about materials. This introduction provides an overview of this task, with specific emphasis on light-matter interactions at nanoscale dimensions, types and behaviors of various near-field optical probes, SNOM instrument design considerations, and current scattering-type SNOM techniques for subdiffraction-limited materials characterization and imaging.

A. Breaking the Diffraction Limit with Optical Antennae

Diffraction places a fundamental limit on the spatial dimensions to which light can be focused using traditional macroscopic lenses ($\sim\lambda/2$) [1], and therefore the dimensions over which small objects can be resolved and ultimately imaged. One method to circumvent this limit is to directly couple radiation to an optical antenna, or near-field probe, with characteristic dimensions that are much smaller than the optical wavelength of interest. In this configuration, optical fields can be manipulated (e.g., created, transduced, scattered, confined, concentrated) over very small length scales, with focal characteristics largely dictated by the size of the optical antenna rather than the wavelength of light. The SNOM methods reviewed here allow subdiffraction-limited interrogation and imaging of surfaces in a myriad of ways by manipulating light over spatial distances $<\lambda$, in the so-called near-field vicinity of an object or surface (see **Figure 1.1**).

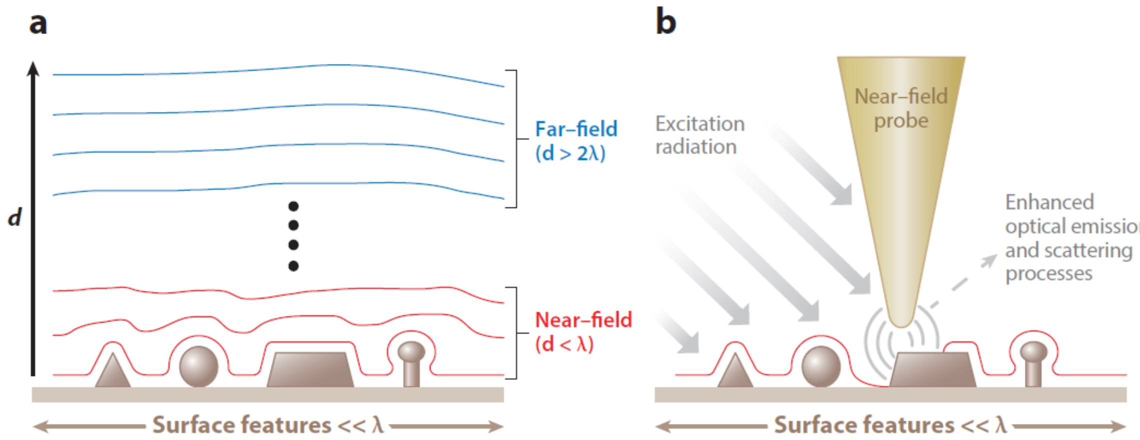

Figure 1.1 Graphical depiction of physical processes important to near-field optical microscopy. *(a)* The near-field encompasses the region of space very close to a radiating surface at distances less than the optical wavelength λ. High–spatial frequency components of the electromagnetic fields in this region (evanescent waves) are bound to the surface and cannot propagate into free space. *(b)* A near-field probe couples to local optical processes (e.g., scattering, absorption, photoluminescence, Raman) and transduces them to the far-field. The spatial resolution of this process is controlled by the dimension of the optical antenna probe rather than the optical wavelength (diffraction limit).

In the optical near-field regime, the distribution of electric and magnetic fields can be very complex, changing rapidly in both magnitude and direction over short distances <<λ [2]. The near-field can be expressed as a superposition of electromagnetic waves of varying spatial frequencies, with high spatial frequencies containing information about the smallest surface features. These high-frequency fields are non-propagating or evanescent; that is, they are bound to the surface and cannot transport energy away from it [3]. The intensity of these evanescent fields decays exponentially with distance away from the emitting or scattering surface, and fine spatial information about the surface is lost at distances >λ. For distances beyond a few λ away, only low–spatial frequency fields remain; these fields propagate out into space where they can be transduced using traditional, far-field, lens-based optical microscopy techniques. Because of the inherent short-range nature of evanescent waves, interacting with the near-field of a surface requires placing a probe very close to an emitting structure. **Figure 1.1b** illustrates this concept, where a near-field probe smaller than λ interacts with a surface. The probe can locally enhance or transduce optical fields via several mechanisms discussed below and reviewed in Reference 4, allowing multimodal information gathering at the nanoscale.

Electric Field Enhancement

The main function of a near-field probe is to locally change (enhance) the magnitude of an optical field through geometric and/or plasmonic effects. Geometric enhancement, also known as the lightning rod effect [5], occurs when the optical antenna probe has high local curvature over distances <<λ (e.g., corners, sharp edges, small gaps). In this case, the sharp boundaries of the probe restrict the motion of electrons responding to the applied electric (optical) field, causing charge concentration along the probe surface [6]. In practice, geometric enhancement produces fields typically two to ten times larger than their free-space excitation sources [7-9].

The second, and often more important, contribution to electric field enhancement with a near-field probe comes from the excitation of plasmon resonances. Plasmons are collective oscillations of free electrons in a material, typically excited with radiation in the UV-Vis-NIR wavelength range, that are confined to a metal-dielectric interface, e.g., on flat surfaces or nanostructures or within a nanoscale dielectric gap [10, 11]. **Figure 1.2** shows the charge and field distributions associated with basic plasmon resonance modes, known as surface plasmon polaritons (SPPs), localized surface plasmons (LSPs), and gap-mode plasmons (GMPs), respectively. In all three cases, collective electron oscillations generate local charge separation that creates strong electric fields at the surfaces of the plasmonic material.

Reference 12 gives an overview of the diverse applications plasmon are now finding use in, with spectroscopy being only one of many uses.

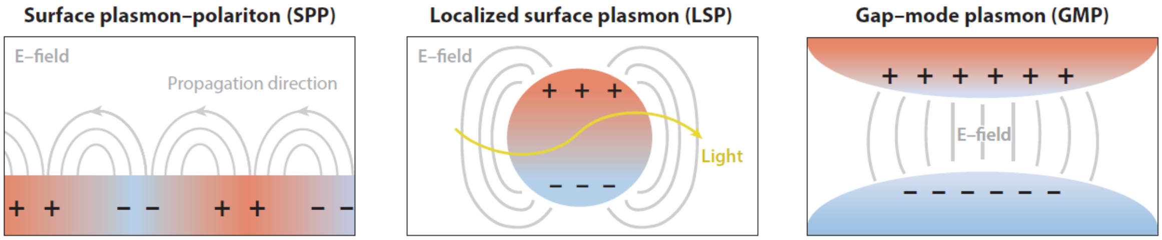

Figure 1.2 Illustrations of the geometries and electric fields associated with common plasmon resonance modes. Scanning near-field optical microscopy experiments use light to excite these plasma oscillations, which may then decay via radiative or nonradiative pathways. For each of the plasmon resonances shown, charge separation at the surface of the plasmonic material leads to the formation of intense, localized electric fields, which may be used to enhance optical processes.

Probe-Surface Optical Interactions

The optical interactions with a near-field probe discussed thus far essentially ignore the dielectric environment surrounding the probe. As one might imagine, the presence of a sample within the near-field of the probe, as well as the complex dielectric response of the sample [i.e., the complex refractive index, $\tilde{n}\,(\lambda) = n(\lambda) + ik(\lambda)$, or permittivity, $\tilde{\epsilon}\,(\lambda) = \epsilon_1\,(\lambda) + \epsilon_2(\lambda)$], can have a dramatic effect on how light couples to, is enhanced by, and/or is scattered by the probe and surface. In fact, it is these very interactions that encode information about the subwavelength details of the surface and serve as a basis for SNOM-based interrogation and imaging. Moreover, the intense optical field of the probe can influence radiative emission, Rayleigh and Raman scattering processes, and plasmonic properties of the sample under interrogation. For example, the amplitude/phase of light elastically scattered by a near-field probe contains information about the local refractive index of a nearby sample, Raman scattering from molecules or phonons can be enhanced by several orders of magnitude [13], and fluorescence can be enhanced or quenched depending on the distance between the fluorophore and metal probe [14]. The following sections highlight all of these effects in the context of various subdiffraction-limited sample interrogation and imaging modalities with near-field probes that provide insight into the local morphology, chemistry, and optoelectronic properties of a heterogeneous material.

Chemical Enhancement

Near-field probes are normally extremely close (less than a few nanometers) to the analytes and surfaces they study, sometimes to the point of direct contact. Changes in electronic structure and bonding may occur over such short distances, modifying the inherent optical properties of the sample under study; these effects are collectively referred to as chemical enhancements. Predicting chemical enhancement is a difficult task because it requires a full quantum mechanical treatment of the interacting probe-sample system. Some headway has been made for extremely simple systems, such as a single molecule near a small metal cluster [15], and theoretical results suggest that chemical enhancements can be large (1,000×) [16, 17]. However, Van Duyne et al. [18, 19] have observed chemical enhancements in the range of only 10× to 100× using different chemical moieties in contact with Au/Ag surface-enhanced Raman scattering substrates. Overall, strong arguments can be made that chemical enhancements have so far played a minimal role in near-field spectroscopy when compared to the electric field enhancement mechanism [20].

B. Components of a Scanning Near-field Optical Microscope

SNOM instruments are complex systems that combine a scanning probe microscope platform [e.g., scanning tunneling microscope (STM), atomic force microscope (AFM), or fiber-based hybrid scanning probe microscope] with optical interrogation of a sample using lasers or broadband light sources from the UV to infrared (IR) and include collection and analysis of transmitted, reflected, and/or scattered light with dispersive or interferometer-based (Fourier transform) optical spectroscopy. This instrument design space is enormous. However, this versatility is one of the strengths of SNOM, as it allows multiple information gathering and imaging modalities to be applied to all types of materials and sample configurations. Below, we provide an overview of SNOM instrument design considerations and then highlight various SNOM characterization and imaging modalities.

(i) Selecting a Near-Field Probe

As described earlier, the electric field enhancement mechanism is the most important factor to consider in near-field probe selection. Because these enhancements depend on excitation frequency, probe shape and material, dielectric environment, sample substrate, and analyte, selecting an optimal near-field probe is both challenging and often application specific. Nevertheless, most researchers use standard designs [i.e., nanoscale apertures or scattering-type (s-SNOM) probes (**Figure 1.3**)] that are easy to fabricate and applicable to a broad range of experiments.

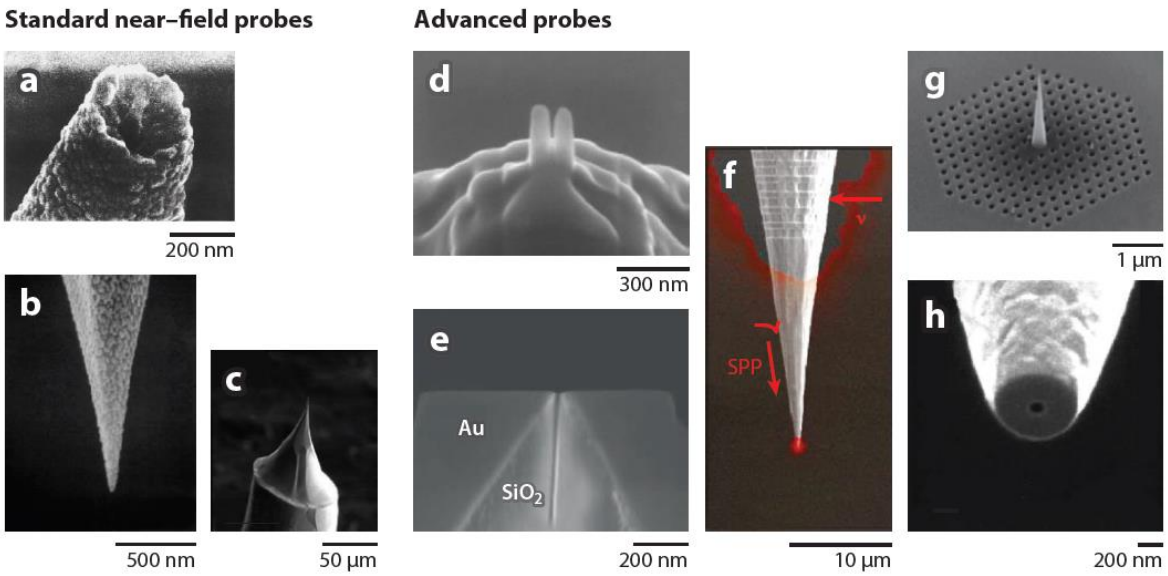

Figure 1.3 Near-field probe designs used in scanning near-field optical microscopy experiments. The most common variants are (*a*) metal-coated tapered optical fibers, (*b*) metal-coated AFM tips, and (*c*) electrochemically etched metal wires. More complex shapes can be formed using focused ion beam (FIB) milling. These include (*d*) dipole antennas, (*e*) campanile structures, (*f*) surface plasmon-polariton waveguides, (*g*) nanohole arrays, and (*h*) flat-cut apertures. Figures were reproduced or adapted from the following with permission: (*a*) Reference 21, Am. Inst. Phys.; (*b*) Reference 24, Elsevier; (*c*) Reference 25, Am. Chem. Soc.; (*d*) Reference 27, IOP Publ.; (*e*) Reference 28, AAAS; (*f*) Reference 29, Am. Chem. Soc.; (*g*) Reference 30, MacMillan Publ. Ltd.; (*h*) Reference 31, Am. Inst. Phys.

Aperture probes

The most intuitive method to confine light to very small spatial dimensions is through the use of subwavelength-sized apertures (**Figure 1.3a**), such as pulled optical fibers or sub-λ-diameter holes that are focused ion beam (FIB) milled into monolithic Si AFM tips [21]. A quantitative description of the interaction of radiation with such apertures is surprisingly complicated and is still an area of active research [3, 22]. Simple theoretical analysis predicts that the optical power density transmitted through a small aperture of diameter d scales as $(d/\lambda)^4$ [22], and that the taper angle of the probe before the aperture should be kept wide to achieve higher transmission [23]. Increasing the source power can partially make up for probes with low transmission, but only up to the point at which the sample or probe itself is damaged by the high intensity. The lateral surface of pulled probes is metallized (usually with Al) to confine the light, with the sub-λ-diameter end of the fiber (the aperture) left uncoated. This is accomplished by evaporating metal onto a rotating fiber at an oblique angle or by purposefully FIB machining the probe end.

Aperture-less (scattering-type) probes

Most near-field probes used today are of the scattering, or s-SNOM, variety. An advantage of s-SNOM probes is that they usually generate local optical fields that are more intense than the incident radiation, in stark contrast to aperture-based geometries. Common designs are metal-coated AFM tips [24] or electrochemically etched, fine metal wires [25] (**Figure 1.3*b,c***). These probes are fast and cheap to make but suffer from poor reproducibility, giving highly variable field enhancements. In fact, fabrication of s-SNOM probes with large and reproducible field enhancements is a current area of research, and the bane of many experimentalists. Another challenge with s-SNOM probes is that they do not filter out optical signals originating from sample material outside of the probe near-field region. When light is focused onto an s-SNOM probe, a portion of the sample surface around the probe is also illuminated. Scattering or emission from this larger area is considered undesired background [26]. Fortunately, there are instances in which the magnitude of the near-field signal can be made larger than the background using plasmonic probes that support extremely large local fields and/or lock-in demodulation [e.g., modulating probe-surface distance (dithering the probe vertically) and detecting scattered light with a lock-in amplifier].

Advanced near-field probes

More complicated near-field probe designs have also been explored (**Figure 1.3*d–h***) in an effort to increase local electric field strength and spatial resolution, as well as bias detection to the near-field. These include sub-λ dipole antennas [27], campanile structures [28], SPP waveguides [29], nano-hole arrays [30], and flat-cut apertures [31]. As an example, the SPP-waveguide probe uses a FIB-machined grating-like structure on the probe shaft, some tens of microns away from the probe apex, to couple light via SPPs down to the apex; because the probe-surface gap is not directly illuminated with the pump laser spot, background signals generated away from the apex can be significantly reduced. Unfortunately, FIB machining is required to make many of these complex geometries, which is both costly and time consuming on an individual probe basis.

Probe longevity

A final consideration when selecting a near-field probe is how it will interact, both physically and chemically, with the sampling environment and substrate under interrogation. Thiol-functionalized Au tips have been shown to resist contamination that may be present in ambient or liquid environments [32]. For tapping- or contact-mode AFM measurements, probes can be mechanically damaged from surface forces during use [33], which can be circumvented in some cases with hard, transparent oxide coatings [34]. Unfortunately, coating a near-field probe (i.e., intentionally, from environmental contamination, or via imaging a surface) almost always reduces the local field enhancements that can be obtained [35]. Optical absorption in the probe itself can also lead to large temperature changes that modify probe morphology and affect field enhancement [36, 37]. All these factors contribute to probe degradation; the result is that most near-field probes tend to be highly active for a short time, often lasting for only a single day of experimentation.

(ii) Nano-Positioning Systems

The near-field probe, sample surface, and illumination/collection optics must all be aligned to perform a SNOM experiment. This is easiest with aperture-based SNOM, as the fiber-based illuminator/collector is usually raster scanned across the surface with probe-surface distance regulation provided by a quartz tuning fork sensor. In this case, the aperture (fiber) is attached to a tuning fork that is excited mechanically or electrically in shear mode (horizontal to the surface) with amplitude, phase, or frequency (phase-locked loop) regulation. It is possible to implement sample scanning in this case, but it is rather uncommon. For s-SNOM, many instrument configurations are possible, but they generally involve coupling an optical microscope with an STM or AFM. For these instruments, distance regulation is based on probe-surface current (STM), normal force (AFM contact mode), or oscillation amplitude/phase/frequency (AFM tapping mode, tuning fork shear force). Most s-SNOM systems are configured for sample (rather than probe) scanning so excitation and collection optics only have to be statically aligned with the probe-surface junction at the beginning of an experiment.

(iii) Light Sources

Specific physical processes of interest determine what light source to use in a near-field experiment, as with spectroscopy in general. UV and visible sources have energies well suited for direct study of electronic structure through absorption, fluorescence, and photoluminescence processes. Vibrational excitations can be observed either with inelastic Raman scattering or via direct absorption of IR radiation. Many coherent (laser) sources are now available throughout the UV-vis-IR frequency range with pulsed or continuous wave operation. The wavelength tunability of these sources continues to increase with advances in laser engineering, but the only truly broadband, tunable optical sources remain free-electron lasers or optical emission from synchrotron beam lines [38-40]. Since the diffraction limit is proportional to the incident wavelength (~λ/2), it is reasonable to ask what sets a lower limit on wavelengths commonly used. The main factor is that sample damage increases rapidly with the use of UV sources, as the energy becomes sufficient to break bonds and cause reactions. Additionally, materials with the strongest plasmon responses (Ag/Au), crucial for near-field applications, have resonances limited to the visible and NIR ranges. Finally, there is the practical reality that it is much easier to work with and align visible light compared to UV or IR.

(iv) Photodetectors

For optical detection, the primary considerations are what energy range will be measured and whether single-channel or energy-resolved spectra are needed. For instance, if the total intensity of a fluorescence band, or Rayleigh scattering, is being used for near-field imaging, a single-channel detector (photomultiplier tube or avalanche photodiode) will be sufficient. However, if Raman or IR spectra are being acquired, a dispersive or interferometer-based spectrometer is needed to analyze multiple wavelengths simultaneously. In the former case, a grating-based spectrometer with a thermoelectrically or liquid nitrogen cooled CCD camera is commonly used, allowing a full optical spectrum to be obtained at each spatial imaging point on the sample. Temporal studies are also possible with pulsed light sources and time-correlated photon counting.

(v) Putting It All Together

The aforementioned hardware can be arranged in several different configurations, as shown in **Figure 1.4**. These include side-on, inverted, top-down, and parabolic [41] illumination/collection geometries. Inverted geometries allow the use of high–numerical aperture (>1) oil-immersion objectives that have a large solid angle of light collection, but these systems are restricted to transparent samples. Total-internal reflection illumination has also been used, enabling direct excitation of SPPs in metal films [42].

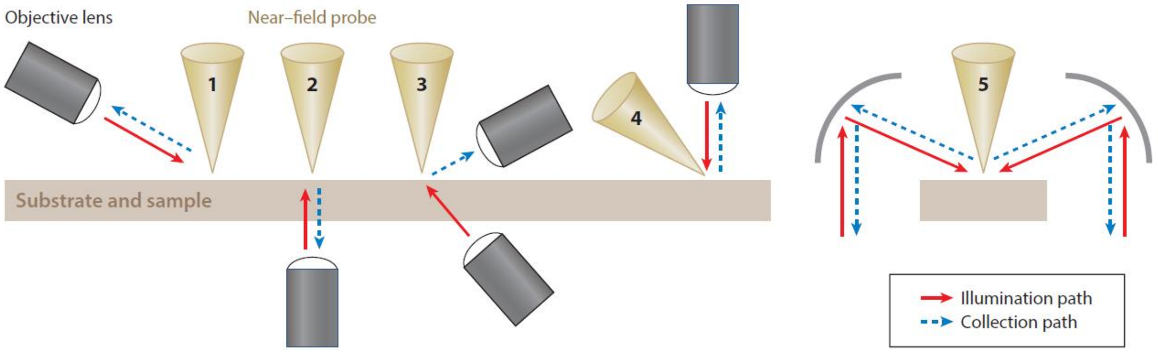

Figure 1.4 Schematic of various scanning near-field optical microscopy instrument configurations, including ① side-on, ② and ③ inverted, ④ top-down, and ⑤ parabolic illumination/collection designs.

C. Overview of Current SNOM Techniques

The following presentation of various SNOM techniques is broadly divided into those using aperture versus scattering (s-SNOM) near-field probes. Between these two approaches, s-SNOM probes are more suitable for a wider range of applications and thus garner the majority of the discussion. The reader is referred to Reference 43 for a review on aperture-based SNOM instrumentation and methods, but we briefly mention them below for completeness.

Aperture-Based SNOM

Aperture-based SNOM has been carried out in different illumination-collection configurations, as schematically shown in **Figure 1.5a**. The SNOM fiber (**Figure 1.5b**) itself can be used to deliver and/or collect light to and from a surface or can be combined with a microscope objective for illumination or collection. Aperture-SNOM studies have been performed using Rayleigh scattering [44-46], fluorescence [47-49], and Raman optical signals [50, 51]. For Raman studies, the combination of low aperture transmission efficiencies and inherently small scattering cross-sections leads to very lengthy collection times that prohibit 2D imaging [52, 53]. For higher signal scattering experiments, the full spectrum of light transmitted through the aperture can be analyzed. As an example, Kuipers and colleagues [54] collected and mapped the evanescent light escaping from a laterally excited nanohole waveguide with a metallized SNOM tip (**Figure 1.5c**). In other work, Wang et al. [55] demonstrated excitation and focusing of surface plasmons by a specially engineered probe that increased fiber transmission by 20–40 times compared with that of traditional aperture probes (**Figure 1.5d**).

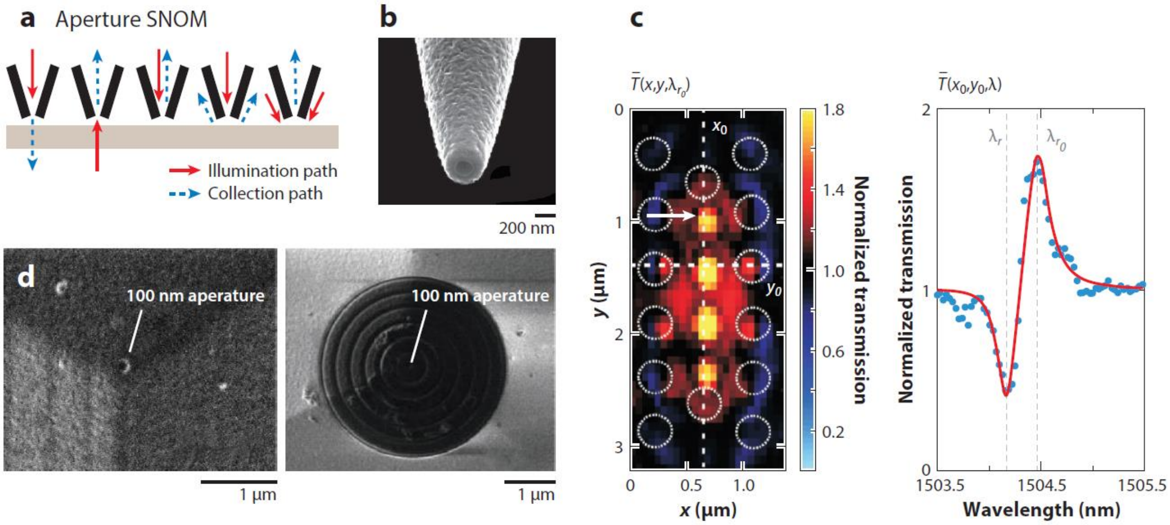

Figure 1.5 Aperture scanning near-field optical microscopy (ASNOM) instruments geometrically restrict the spatial dimensions of propagating light waves using a nanoscale opening. (*a*) Various illumination and collection pathways used in aperture SNOM (adapted from the research group site of Dr. Hans Hallen at North Carolina State University). (*b*) Aperture probe fabricated from an Al-coated tapered optical fiber. (*c*) Near-field image of evanescent optical fields above a silicon photonic nanocavity and the appearance of a transmission minimum caused by coupling between the probe and cavity. (*b*,*c*) Reproduced with permission from Reference 54, Am. Physical Soc. (*d*) A plasmonic grating is used to concentrate surface plasmons into a single aperture, leading to increased transmission efficiencies (reproduced with permission from Reference 55, Am. Chem. Soc.).

Scattering SNOM

As mentioned earlier, s-SNOM probes are designed to generate locally enhanced (subdiffraction-limited) optical fields via the lightning-rod effect and/or plasmonic coupling. However, the probe and sample surfaces are usually bathed in a large laser excitation spot (best case is a diffraction-limited spot) that ultimately generates considerable and unwanted background [26]. In some cases, such as with tip-enhanced Raman scattering (TERS), the near-field signal (S_{NF}) can be made much larger than the background (S_{BG}) using strongly enhancing plasmonic probes.

In many cases, however, $S_{NF} \leq S_{BG}$, and more sophisticated methods are necessary. The first strategy devised was to exploit the very short spatial extent of the near-field. If the probe is retracted a short distance from the surface, the near-field signal strength will decrease significantly, but the background should change very little [56]. Fortuitously, this is exactly what occurs in tapping-mode AFM operation, wherein the probe oscillates normal to the sample surface, usually on the order of tens of nanometers. Hence, by demodulating the photodetector signal at some harmonic of the cantilever oscillation frequency, the near-field signal can be selectively extracted [57]. Demodulating at higher harmonics will provide greater selectivity for the near-field signal, but at the cost of decreased signal-to-noise ratio [58]. This lock-in demodulation scheme has been employed successfully for sample imaging across multiple s-SNOM experiments [59-61].

It turns out that lock-in demodulation is not a complete solution to the problem of separating near-field and background signals. The demodulated near-field signal will still include a constant component of background scattering as interference [62, 63]. Circumventing this requires what is now referred to as pseudo-heterodyne detection (see section titled Near-Field Infrared Interferometry), first demonstrated by Hillenbrand & Keilmann [64]. The sample is positioned in one arm of a Michelson interferometer, with a vibrating mirror placed in the other arm (see **Figure 1.6a**). The combination of lock-in demodulation and changing phase of the reference beam allows extraction of the pure near-field signal that contains information about the entire probe-sample-substrate system. To remove contributions from the probe or substrate, a reference measurement must also be made on a region of bare substrate. Dividing out this reference leaves only the sample response, which can then be connected to local optical properties using various models.

Elastic (Rayleigh) Scattering–Based SNOM Techniques

We begin our discussion on specific s-SNOM techniques by examining methods based on measuring the amplitude, phase, or polarization change of light that is elastically (Rayleigh) scattered ($\lambda_{in} = \lambda_{out}$) by the probe-sample system. The ultimate goal is to relate changes in Rayleigh scattering to local sample properties, such as refractive index, absorbance, film thickness, and molecular/crystal orientation. For scattering-based SNOM imaging at a single wavelength, the reader is referred to References 65 and 66. We focus instead on more advanced and recent methods that can provide morphological and/or chemically specific information about a sample.

Scanning near-field ellipsometric microscopy

In scanning near-field ellipsometric microscopy (SNEM), polarized, monochromatic light from a laser is focused onto the end of a metal-coated near-field probe [67], and a portion of the scattered light is directed to a single-channel photodetector with polarization analysis. The scattered optical signal usually contains three parts: (*a*) a constant background, (*b*) the desired near-field signal that varies exponentially with probe-surface distance, and (*c*) a sinusoidal-like interference term due to Fabry-Perot effects [68] from the cavity formed by the probe/cantilever and sample surface. These signals can be deconvolved by varying the probe-surface distance in an approach curve to reveal a near-field optical signal [69]. Unfortunately, quantitatively connecting this near-field signal to the complex refractive index (*n* and *k*), thickness, crystal structure, and/or dopant concentration [70] of the sample is extremely challenging. Several attempts at this have been made, and Soh and coauthors [71] have demonstrated that the thickness and optical constants of Au can indeed be accurately extracted from SNEM measurements of thin Au films on a transparent substrate. More complex and heterogeneous samples can be imaged with SNEM, but the exact origin of image contrast is often unclear. An edited collection of SNEM research articles can be found in Reference 72.

Near-field infrared interferometry

Nano-FTIR, or IR-nanospectroscopy, is a powerful SNOM modality that has seen a burst of innovation and development over the past decade. The technique can measure broadband IR absorption spectra of surfaces with spatial resolutions as low as 10–20 nm, a truly remarkable feat as the excitation wavelengths used are on the order of microns. Near-field probes are typically metal coated, and the sample substrate may also be metal coated to further increase scattering intensities. Measurements can be made using a monochromatic or broadband optical source, and both configurations employ a pseudo-heterodyne detection scheme [73] to isolate near-field optical signals (**Figure 1.6a**). The amplitude and phase of scattered light can be related to the local IR absorption bands of the sample, and the spectra obtained agree very well with bulk FTIR data for a wide range of samples [74].

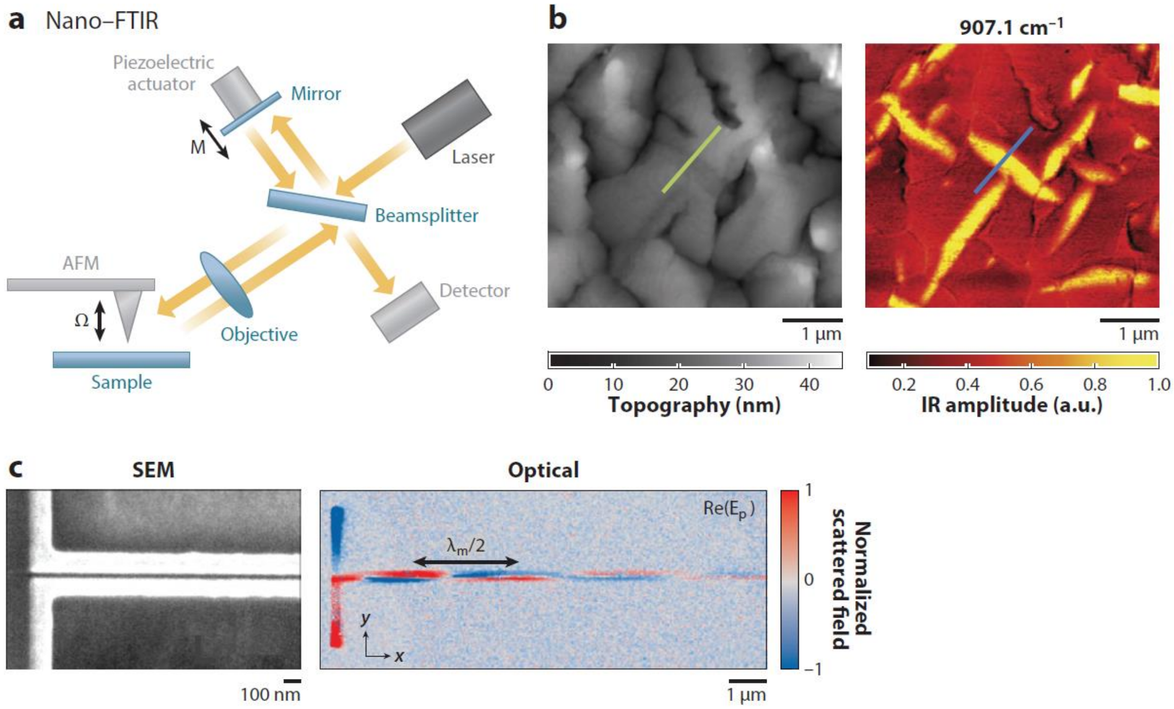

Figure 1.6 Nano-FTIR (Fourier transform infrared spectroscopy) uses interferometry-based detection to measure changes in local scattering intensity. (*a*) Pseudo-heterodyne detection scheme wherein the probe-sample system is placed in one arm of an asymmetric Michelson interferometer. Both the atomic force microscopy (AFM) cantilever and interferometer mirror are vibrated (adapted with permission from Reference 73, Am. Inst. Phys.). (*b*) Topography and near-field absorption images of pentacene nanocrystals (reproduced with permission from Reference 75, MacMillan Publ. Ltd). (*c*) Scanning electron microscopy (SEM) and p-polarized electric field images of a transmission line structure with a 25-nm gap width excited using 9.3-µm incident radiation (adapted with permission from Reference 76, Am. Chem. Soc.).

The advent of tunable lasers has proven very useful in nano-FTIR experiments, as the excitation energy can be exactly matched to specific absorption bands of the sample. For instance, the intensity of Rayleigh-scattered light at a specific wavelength can be recorded as the probe scans, providing a chemical- or analyte-specific map of the surface. For broadband illumination, an interferogram must be collected at each probe location by scanning the interferometer mirror position. This process typically takes on the order of 10 min to obtain reasonable signal-to-noise with a lab-based, thermionic light source, making nano-FTIR imaging with a broadband source time consuming and often unrealistic. This problem can be circumvented using high-intensity broadband IR from a synchrotron beam line, allowing interferograms to be taken in only a few seconds [38, 39].

Figure 1.6 presents images from two different applications of the nano-FTIR technique. Keilmann and colleagues [75] resolved interpenetrating phases of pentacene by exploiting a small vibrational band energy shift (**Figure 1.6b**). At an energy of 907.1 cm^{-1}, absorption in the bulk phase is roughly 3x greater than that in the thin film phase. A nano-FTIR scan at this carefully selected energy revealed discrete domains of bulk-phase pentacene that are hard to see based on the topography data alone. In addition to measuring local absorption, nano-FTIR can also be used to monitor how optical energy is transported along surfaces. For example, Hillenbrand et al. successfully imaged a subwavelength transmission line using mid-IR radiation (**Figure 1.6c**) [76]. In this experiment, the excitation laser was fixed at the location of an input-coupling antenna, with the s-SNOM probe scanned along the top of the waveguide. The probe acted as a local transducer of the confined optical fields in the waveguide gap, allowing them to be scattered into the far-field and detected. Reference 74 provides a review of other recent nano-FTIR work; commercial s-SNOM instruments are available from both Bruker and neaspec GmbH.

Photothermal-induced resonance microscopy

Infrared mapping of chemical moieties on a surface at nanoscale spatial dimensions has also been accomplished using non-optical detection. Specifically, absorption of light by material directly beneath a near-field probe can lead to local heating—and thermal expansion. This expansion is detected by observing how the cantilever amplitude rings down after being mechanically bumped during the expansion event. The technique is referred to as photothermal-induced resonance (PTIR), or AFM-IR (**Figure 1.7**). Unlike other SNOM methods, in PTIR, both the thermomechanical and optical properties of the sample are important. For the technique to work, the sample must efficiently convert light to heat through absorption, and this heat must result in expansion of the sample in the direction normal to the surface, so as to be detected by the cantilever probe. As such, PTIR is inherently more sensitive for the study of materials with high thermal expansion coefficients, such as polymers. Both probe sharpness and the thermal diffusion properties of the sample determine the lateral spatial resolution of the technique [77]. The use of fast pulsed lasers (less than a few microseconds, short compared to the AFM cantilever oscillation period) has led to spatial resolutions consistently below 50 nm, because heat does not have time to laterally diffuse before the expansion is measured [78]. Another advance, termed resonance-enhanced PTIR, tunes the repetition rate of a pulsed laser to match a harmonic of the tapping-mode AFM cantilever (**Figure 1.7a**) [79, 80], greatly increasing cantilever deflection and leading to faster detection.

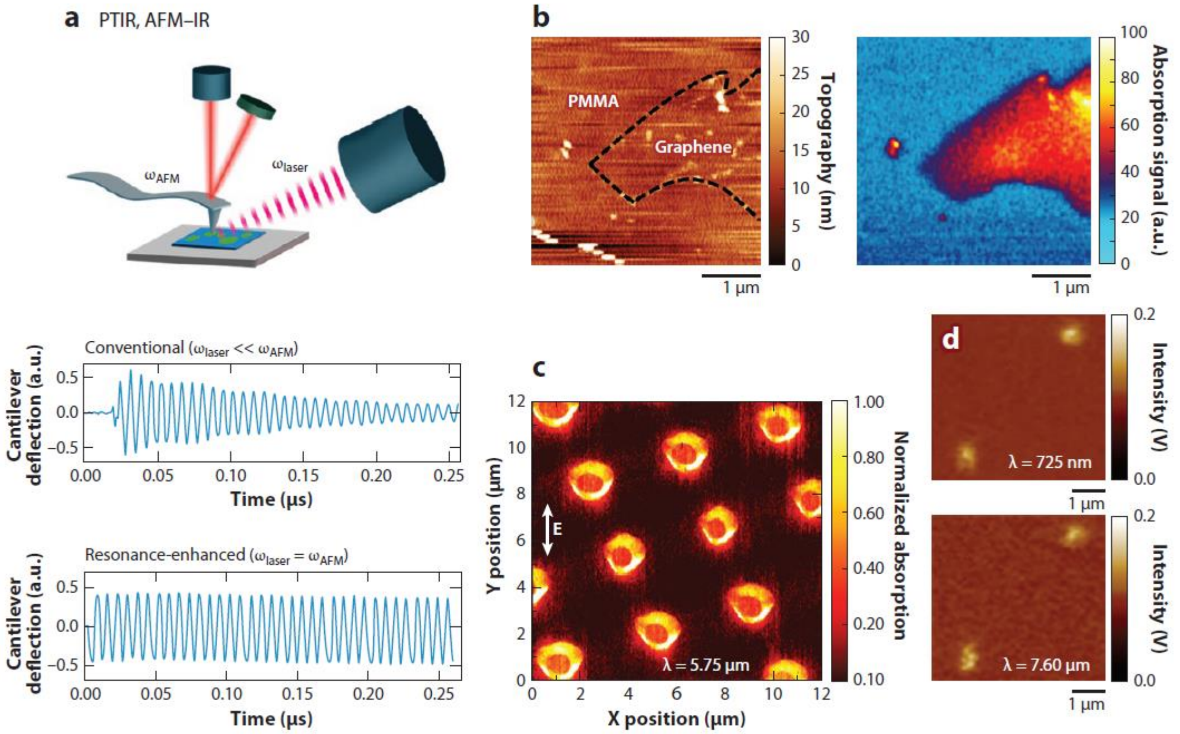

Figure 1.7 Photothermal-induced resonance microscopy (PTIR) detects the local thermal expansion of materials caused by optical absorption using tapping-mode atomic force microscopy (AFM). (*a*) Diagram of a standard side-on PTIR instrument, with temporal plots (*below*) showing how the magnitude of cantilever deflection can be greatly increased by matching the laser pulse (ω_{laser}) and AFM cantilever oscillation frequencies ω_{AFM} (reproduced with permission from Reference 84, Am. Chem. Soc.). (*b*) Topography and PTIR images of graphene deposited on a 100-nm-thick poly(methyl methacrylate) film (reproduced with permission from Reference 81, IOP Publ.). (*c*) PTIR image of InAs micropillars showing plasmonic resonances at the indicated mid-infrared (IR) wavelength (reproduced with permission from Reference 82, Am. Inst. Phys.). (*d*) PTIR imaging at both visible and mid-IR wavelengths of dye molecules loaded in a PMMA matrix (reproduced with permission from Reference 83, Am. Chem. Soc.).

Although organic samples tend to have the highest thermal expansion coefficients, thermal imaging of inorganic samples is also possible. Rosenberger et al. [81] suggested placing a thin film with a high thermal expansion coefficient underneath the sample. The authors were then able to image both carbon nanotubes and graphene flakes deposited on top of ~100-nm-thick polymer films (polystyrene or poly(methyl methacrylate)) (**Figure 1.7b**). Felts et al. [82] produced an array of InAs micropillars with surface plasmon resonances in the mid-IR range. Thermal expansion of InAs would normally be challenging to detect, but the additional optical energy coupled into the plasmon modes produce enough local heating to successfully form a PTIR image of the array (**Figure 1.7c**). While PTIR has seen the most use at mid-IR frequencies, the thermal expansion mechanism is applicable over a wide spectral range. For example, Centrone et al. [83] have designed an instrument integrating three different optical sources spanning wavelengths from 400 to 9,000 nm. Poly(methyl methacrylate) films loaded with dye molecules were then imaged at both visible and mid-IR frequencies (**Figure 1.7d**). This type of broadband instrument provides an extremely flexible means of investigating electronic and vibrational structure over a wide range of energies. Reference 84 provides a recent review and commercial PTIR instruments are available from Anasys Instruments.

Inelastic Scattering-Based SNOM Techniques (Photoluminescence and Raman)

The previous sections showcased the breadth of information that can be obtained by monitoring elastic scattering, absorption, and transmission processes of incident light interacting with the probe-sample near-field region. These processes are a limited subset of light-matter interactions that can be leveraged to interrogate and image materials. For example, numerous inelastic optical processes involving electronic, vibrational, and vibronic excitations of molecules and crystals, such as luminescence and Raman scattering, can reveal very detailed information about physicochemical properties of materials. The following sections highlight SNOM methods based on these types of inelastic optical interactions.

Tip-enhanced photoluminescence and fluorescence

Photoluminescence is a broad term for any process that involves the emission of radiation following optical absorption. Fluorescence is one type of photoluminescence, specifically used for radiative emission by individual molecules or small clusters of atoms with distinct electronic energy levels. To have fluorescence, there must first be absorption to generate excited states. As was shown in the previous sections, near-field probes increase absorption through local electric field enhancement. The more challenging piece is to understand how the radiative decay of the molecular excited state is influenced by the presence of the near-field probe. Lakowicz [85] provides an excellent summary on this topic as part of the *Radiative Decay Engineering* series. Any modification of a fluorophore's spontaneous emission rate caused by its local environment is known as the Purcell effect. For a metallized near-field probe, this effect is not monotonic, and fluorescence can be either enhanced or quenched depending on the fluorophore-probe separation. At short distances, the fluorophore may excite plasmon resonances in the metal that cannot decay radiatively. Novotny and colleagues [14] clearly observed this effect while scanning a gold particle at the end of an optical fiber tip over individual Nile blue dye molecules buried 2 nm beneath an SiO_2 surface (**Figure 1.8a**i-iii). When the probe was directly over the molecules, the fluorescence decreased in agreement with theoretical predictions. Tip-enhanced photoluminescence can also be collected for 2D materials and thin films. Roy and colleagues [86] recently reported tip-enhanced photoluminescence images of an MoS_2 flake, in which photoluminescence was measured at length scales down to 20 nm (**Figure 8*b***i-iv); using spectral deconvolution, they spatially imaged the relative intensities of various exciton decay modes. The full *Radiative Decay Engineering* text can be found in Reference 87; a recent review of work involving plasmonic structures and fluorophores is available in Reference 88.

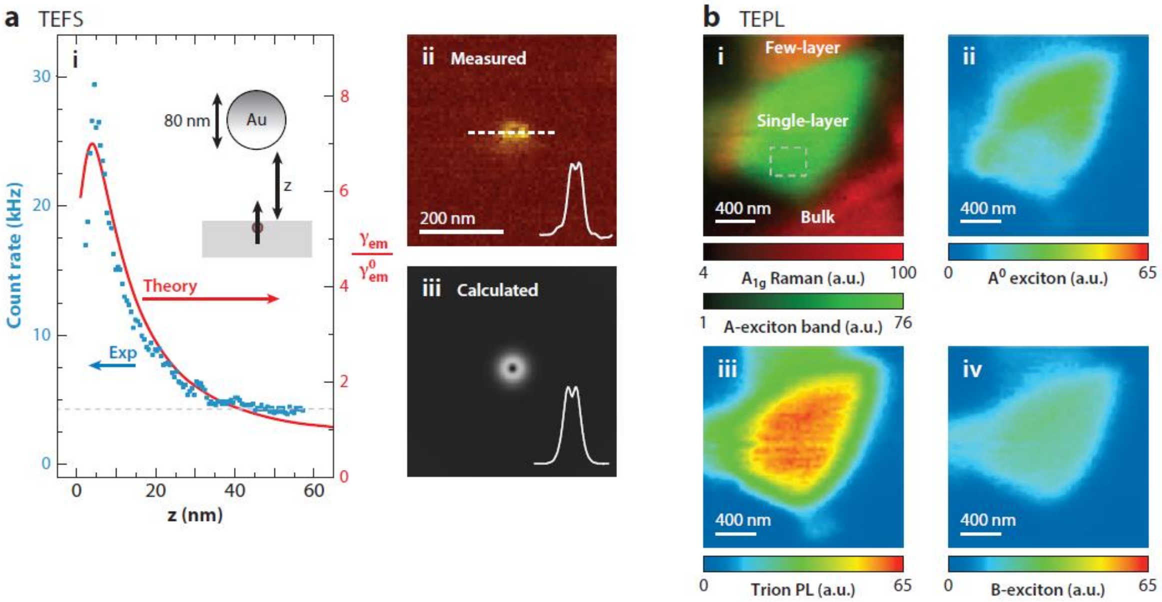

Figure 1.8 Both tip-enhanced fluorescence spectroscopy (TEFS) and tip-enhanced photoluminescence (TEPL) use near-field probes to increase the radiative decay rate of excited states of molecules and materials. (*a*) Comparison of measured and predicted fluorescence enhancements of a single Nile blue molecule buried 2 nm beneath a glass surface, interacting with a single Au sphere. Fluorescence intensity was collected both as a function of the molecule-sphere separation distance (i) and as images along the surface plane (ii–iii) (adapted with permission from Reference 14, Am. Phys. Soc.). (*b*) Photoluminescence mapping of an MoS_2 flake. Both the total PL signal (i) and individual exciton contributions (ii–iv) deconvoluted from the full image (i) are shown (reproduced with permission from Reference 86, Roy. Soc. Chem.).

In the biological sciences, interest in fluorescence SNOM techniques has now been largely surpassed by the success of other subdiffraction-limited fluorophore imaging strategies, such as stimulated emission-depletion, stochastic optical reconstruction microscopy, and photoactivated localization microscopy [89]. These tools allow imaging of fluorescently tagged biological structures over wide areas with spatial resolutions on the order of 10 nm.

Tip-enhanced Raman spectroscopy

The s-SNOM variant that has generated the largest amount of research interest over the past two decades is TERS. Using LSP resonances, near-field probes can achieve local field enhancements of 10–1,000×, and when coupled with nonlinear plasmonic processes [i.e., Raman ~ fourth power of the field enhancement [13]], normally weak, and frequently unobservable, Raman signals can be increased many orders of magnitude [90]. Another consideration is that Raman cross-sections scale with the fourth power of the excitation frequency [91], providing a strong incentive to use excitation sources in the UV-vis spectrum, as opposed to IR wavelengths. In the visible range, both Ag and Au are plasmonically active [92]. Ag has the stronger plasmon response but forms a surface oxide layer under ambient conditions that greatly reduces probe performance and lifetime [93]. Aluminum can be used for UV plasmonics [94], and in the near-IR range, both TiN_x [95] and various doped metal oxides [96] exhibit plasmon resonances. The overall enhancement values obtained in TERS experiments are large enough to allow full spectral imaging of surfaces, where a spectrum is acquired at every image pixel with a reasonable dwell time (e.g., 10 ms to a few s/pixel). This optical and chemical imaging capability is not currently available with nano-FTIR or PTIR instruments owing to prohibitively long collection times.

Examples of common TERS imaging modalities are shown in **Figure 1.9**. Individual Raman spectra can be collected at discrete sample locations and are then directly connected to local physical or chemical properties. For example, the local strain in mechanically deformed single-walled carbon nanotubes was detected through shifts in Raman modes for linear versus bent regions (**Figure 1.9a**) [97]. This illustrates a direct connection between nanoscale morphology and vibrational structure that is unique to near-field techniques, as opposed to far-field measurements that simultaneously collect signal from a single nanostructure or an ensemble. Tip enhancement of phonon scattering was used to make a hyperspectral cross-section image of an SiGe nanowire (**Figure 1.9b**) [98]. Three distinct phonon peaks associated with Ge-Ge, Si-Ge, and Si-Si in the SiGe phase were only seen when the probe was over the

35 nm dia. nanowire. If signal levels are high, a full Raman spectrum may be collected at every image pixel to form a subdiffraction-limited, chemically specific map of the surface, as demonstrated in **Figure 1.9c** for a 10-nm-thick, patterned copper phthalocyanine film [42]. Having a complete spectral dataset like this allows researchers to post-process data in numerous ways, including localization of specific vibrational band intensities, spatial correlation of shifts in peak energies/widths, or deconvolution of spectra composed of overlapping emission signals. If there is insufficient signal to efficiently collect full spectra, light can instead be focused onto a single-channel photodetector. This provides higher signal to noise at the expense of spectral resolution. Raschke and colleagues [99] used this strategy to obtain high–spatial resolution near-field images of a $BaTiO_3$ nanorod and were able to distinguish ferroelectric domains within the rod itself based on the total phonon scattering intensity (**Figure 1.9d**).

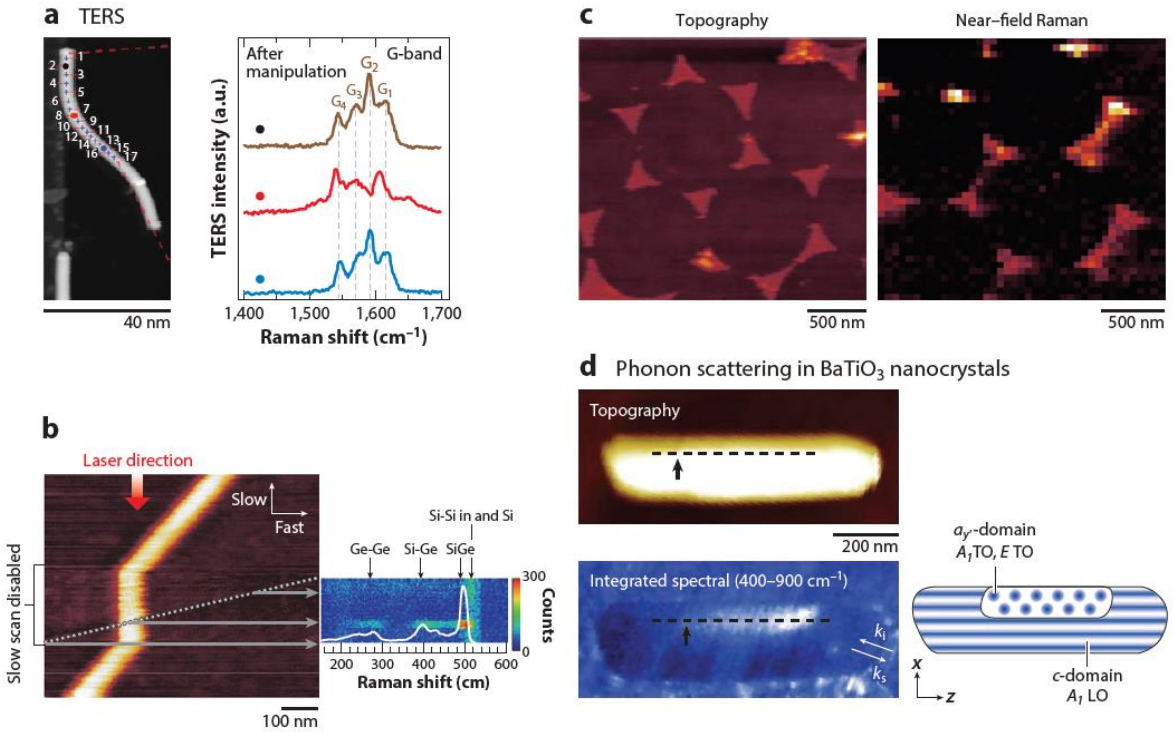

Figure 1.9 Tip-enhanced Raman spectroscopy (TERS) uses near-field probes with plasmonic resonances to generate extremely large optical enhancements. (*a*) Point spectra collected on a mechanically deformed single-walled carbon nanotube showing strain-induced changes in G-band scattering at positions with high local curvature (adapted with permission from Reference 97, Am. Chem. Soc.). (*b*) Topography and hyperspectral TERS image of various phonon modes in a SiGe nanowire (reproduced with permission from Reference 98, Am. Inst. Phys.). (*c*) Two-dimensional TERS image of a patterned copper phthalocyanine film, formed by integrating Raman peaks in the 500–1,650 cm^{-1} range from 1,681 point spectra (reproduced with permission from Reference 42, John Wiley and Sons Ltd). (*d*) TERS image resolving two distinct ferroelectric domains within a single BaTiO$_3$ nanocrystal, made by collecting the total phonon scattering intensity (adapted with permission from Reference 99, MacMillan Publ. Ltd).

There are often significant differences between far-field Raman and TERS spectra for the same molecule or material. This may result from interactions of the surface (analyte) species with the probe and/or substrate, as well as the orientation of molecular or lattice dipoles with respect to the polarization axis of the near-field, which is typically normal to the sample surface [100]. Additionally, strong electric field gradients can be generated over molecular length scales that tend to relax typical spectroscopy selection rules, allowing TERS spectra to contain both Raman and IR-active vibrational modes [101, 102]. TERS spectra may also have vibrational peaks superimposed over a broad background signal, which has been attributed to radiative decay of local plasmon resonances supported by the probe apex [103]. The latter is the same mechanism that creates weak photoluminescence observed for other plasmonic metal nanostructures [104]. Finally, when measuring a small number of molecules, or even a single molecule, thermal motion can lead to temporal changes of spectra as molecules rearrange [105].

A strategy to achieve extremely large field enhancements is to make TERS measurements above a metallic substrate. In this case, the so-called gap-mode plasmon (GMP) resonance of the combined probe-substrate structure governs the local field strength. GMP fields tend to increase the spatial resolution of TERS by localizing the enhancing region to only a fraction of the probe diameter [90, 106]. The coupling of external radiation to a GMP can be dynamically tuned by adjusting the probe-substrate gap [107, 108]. **Figure 10a** shows how both the intensity and peak emission wavelength of a GMP change as a function of the gap distance between an Au STM tip and Au (111) surface [56]. The field enhancements generated by gap geometries are enormous and were believed to be large enough to measure single molecule TERS spectra. The problem was that lateral spatial resolutions remained on the order of several nanometers, insufficient for resolving individual molecules. Early reports of single molecule TERS relied primarily on indirect evidence from the analysis of transient spectra, so-called spectral blinking [108].

Then, in 2013, Zhang et al. [110] produced an astonishing result: by carefully tuning the gap-distance using different tunneling current setpoints in STM, high-quality TERS images of the molecular structure of a single porphyrin molecule were acquired (**Figure 10b**i–iii). This was shocking because no previous efforts utilizing gap plasmons had achieved such high resolution. Additionally, the theory of light-matter interactions for gaps <1 nm is not well developed, as quantum optical effects become important. These include the finite spatial extent and transient polarizability of atomic/molecular electron densities, non-local charge screening due to electron-electron interactions and tunneling across the gap region [111]. Nevertheless, other groups have now also reported TERS experiments achieving spatial resolutions of less than 1 nm [112, 113]. These results have spurred a renewed theoretical effort from the TERS community to examine coupling of radiation fields to molecular and atomic systems from a first-principles level using time-dependent density functional theory and hydrodynamic models [114]. The hope is that this modeling will provide the necessary guidance for experimental TERS groups to consistently achieve sub-nanometer resolutions and fully open the door to single-molecule optical spectroscopy.

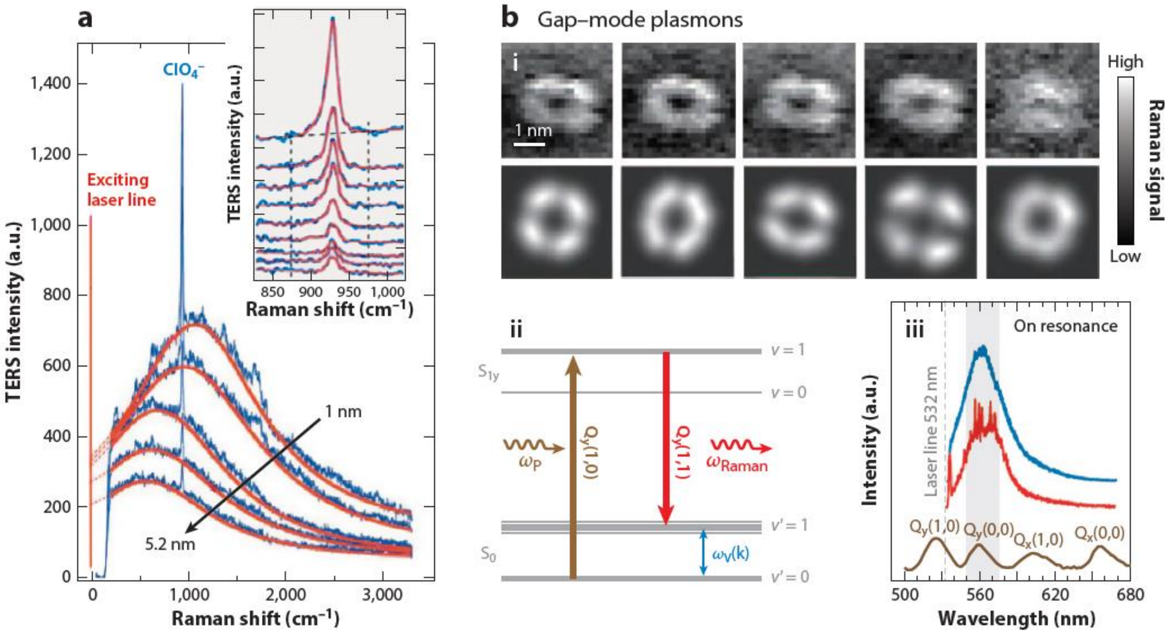

Figure 1.10 Gap-mode plasmons are formed in the small regions between two nanostructures, with at least one of them supporting plasmons. (*a*) Series of spectra showing that both gap-plasmon emission and Raman spectra of guanine depend on the distance between an Au STM probe and Au (111) surface. Both the gap-plasmon peak emission wavelength and intensity are seen to shift (reproduced with permission from Reference 107, Am. Phys. Soc.). (*b*) Tip-enhanced Raman scattering (TERS) imaging of a single H_2TBPP molecule. (i) Image series formed by integrating five different absorption bands (*top row*) and comparison to theoretical scattering signal (*bottom*). The unexpectedly high spatial resolution was achieved when the gap-plasmon resonance was adjusted to match the $Q_y(0,0)$ vibronic transition in the molecule (ii–iii) (adapted with permission from Reference 110, MacMillan Publ. Ltd).

The very high field intensities produced by LSP and GMP resonances of plasmonic probes may generate appreciable scattering from various nonlinear optical processes. Novotny and colleagues [115] have reported near-field second harmonic generation, localized to the apex of a gold probe. Kawata et al. [116] later used this effect to collect hyper-Raman spectra involving vibrational scattering from the virtual state formed through absorption of two pump photons. These spectra were taken of single-walled carbon nanotubes using a 790-nm pump laser and compared with Stokes-Raman spectra directly excited using a 395-nm source. More recently, Raschke and coauthors [117] were even able to show four-wave mixing emission from the apex of a grating-coupled near-field probe using a femtosecond pulsed excitation source. It is important to emphasize that in all of these nonlinear optical processes, the generation rate depends on the second or third power of the local field intensity, meaning that essentially all of the nonlinear optical signal originates solely from the probe apex where the fields are largest. This is quite advantageous, as it eliminates the troublesome background signals previously discussed in linear s-SNOM measurements. Review articles on TERS progress are frequent, but several recent examples can be found in References 118–120. Commercial TERS instruments are available from Bruker, NT-MDT, and Horiba.

D. Conclusions

Nanoscale physicochemical characterization and imaging of materials is a grand challenge that has seen the development of diverse instrumentation using nanoscale optical antennae (near-field probes) of all kinds to manipulate, confine, enhance, and/or transduce light-matter interactions at subdiffraction-limited ($<\lambda/2$) spatial resolutions. The SNOM methods and instruments discussed herein provide a glimpse of how the descriptive power and forensic capabilities of materials characterization with light, when combined with a scanning probe–based platform, allow us to explore heterogeneous materials over different length, energy, and timescales. Moreover, the marriage of high spatial resolution with high spectral resolution enabled by recent SNOM developments provides an unprecedented opportunity to study, understand, and engineer complex materials at or near the level of their intrinsic heterogeneity.

References

1. Abbe E. 1881. VII.—On the estimation of aperture in the microscope. J. R. Microsc. Soc. 1:388–423
2. Bazylewski P, Ezugwu S, Fanchini G. 2017. A review of three-dimensional scanning near-field optical microscopy (3D-SNOM) and its applications in nanoscale light management. Appl. Sci. 7:973
3. Zhang W, Fang Z, Zhu X. 2016. Near-field Raman spectroscopy with aperture tips. Chem. Rev. 117:5095–109
4. Morton SM, Silverstein DW, Jensen L. 2011. Theoretical studies of plasmonics using electronic structure methods. Chem. Rev. 111:3962–94
5. Liao PF, Wokaun A. 1982. Lightning rod effect in surface enhanced Raman scattering. J. Chem. Phys. 76:751–52
6. Crozier KB, Sundaramurthy A, Kino GS, Quate CF. 2003. Optical antennas: resonators for local field enhancement. J. Appl. Phys. 94:4632–42
7. Jersch J, Demming F, Hildenhagen LJ, Dickmann K. 1998. Field enhancement of optical radiation in the nearfield of scanning probe microscope tips. Appl. Phys. A 66:29–34
8. Degtyarev SA, Porfirev AP, Ustinov AV, Khonina SN. 2016. Singular laser beams nanofocusing with dielectric nanostructures: theoretical investigation. J. Opt. Soc. Am. B 33:2480–85
9. Ermushev AV, Boris VM, Oleĭnikov VA, Petukhov AV. 1993. Surface enhancement of local optical fields and the lightning-rod effect. Quantum Electron. 23:435
10. Gibbons PC, Schnatterly SE, Ritsko JJ, Fields JR. 1976. Line shape of the plasma resonance in simple metals. Phys. Rev. B 13:2451–60
11. Sambles JR, Bradbery GW, Yang F. 1991. Optical excitation of surface plasmons: an introduction. Contemp. Phys. 32:173–83
12. Schuller JA, Barnard ES, Cai W, Jun YC, White JS, Brongersma ML. 2010. Plasmonics for extreme light concentration and manipulation. Nat. Mater. 9:193
13. Kerker M, Wang D-S, Chew H. 1980. Surface enhanced Raman scattering (SERS) by molecules adsorbed at spherical particles. Appl. Opt. 19:3373–88
14. Anger P, Bharadwaj P, Novotny L. 2006. Enhancement and quenching of single-molecule fluorescence. Phys. Rev. Lett. 96:113002
15. Jensen L, Aikens CM, Schatz GC. 2008. Electronic structure methods for studying surface-enhanced Raman scattering. Chem. Soc. Rev. 37:1061–73
16. Wu DY, Liu XM, Duan S, Xu X, Ren B, Lin SH, Tian ZQ. 2008. Chemical enhancement effects in SERS spectra: a quantum chemical study of pyridine interacting with copper, silver, gold and platinum metals. J. Phys. Chem. C 112:4195–204
17. Jensen L, Zhao LL, Schatz GC. 2007. Size-dependence of the enhanced Raman scattering of pyridine adsorbed on Ag_n ($n = 2-8, 20$) clusters. J. Phys. Chem. C 111:4756–64
18. Valley N, Greeneltch N, Van Duyne RP, Schatz GC. 2013. A look at the origin and magnitude of the chemical contribution to the enhancement mechanism of surface-enhanced Raman spectroscopy (SERS): theory and experiment. J. Phys. Chem. Lett. 4:2599–604
19. Henry A-I, Ueltschi TW, McAnally MO, Van Duyne RP. 2017. Spiers Memorial Lecture. Surface enhanced Raman spectroscopy: from single particle/molecule

spectroscopy to angstrom-scale spatial resolution and femtosecond time resolution. Faraday Discuss. 205:9–30

20. Moskovits M. Persistent misconceptions regarding SERS. 2013. Phys. Chem. Chem. Phys. 15:5301–11
21. Saiki T, Mononobe S, Ohtsu M, Saito N, Kusano J. 1996. Tailoring a high-transmission fiber probe for photon scanning tunneling microscope. Appl. Phys. Lett. 68:2612–14
22. Weiner J. 2009. The physics of light transmission through subwavelength apertures and aperture arrays. Rep. Prog. Phys. 72:064401
23. Novotny L, Hafner C. 1994. Light propagation in a cylindrical waveguide with a complex, metallic, dielectric function. Phys. Rev. E 50:4094–106
24. Hayazawa N, Inouye Y, Sekkat Z, Kawata S. 2001. Near-field Raman scattering enhanced by a metallized tip. Chem. Phys. Lett. 335:369–74
25. Vasconcelos TL, Archanjo BS, Fragneaud B, Oliveira BS, Riikonen J, Li C, Ribeiro DS, Rabelo C, Rodrigues WN, Jorio A, Achete CA. 2015. Tuning localized surface plasmon resonance in scanning near-field optical microscopy probes. ACS Nano 9:6297–304
26. Ramos R, Gordon MJ. 2012. Near-field artifacts in tip-enhanced Raman spectroscopy. Appl. Phys. Lett. 100:213111
27. Farahani JN, Eisler HJ, Pohl DW, Pavius M, Flückiger P, Gasser P, Hecht B. 2007. Bow-tie optical antenna probes for single-emitter scanning near-field optical microscopy. Nanotechnology 18:125506
28. Bao W, Melli M, Caselli N, Riboli F, Wiersma DS, Staffaroni M, Choo H, Ogletree DF, Aloni S, Bokor J, Cabrini S. 2012. Mapping local charge recombination heterogeneity by multidimensional nanospectroscopic imaging. Science 338:1317–21
29. Berweger S, Atkin JM, Olmon RL, Raschke MB. 2010. Adiabatic tip-plasmon focusing for nano-Raman spectroscopy. J. Phys. Chem. Lett. 1:3427–32
30. De Angelis F, Das G, Candeloro P, Patrini M, Galli M, Bek A, Lazzarino M, Maksymov I, Liberale C, Andreani LC, Di Fabrizio E. 2010. Nanoscale chemical mapping using three-dimensional adiabatic compression of surface plasmon polaritons. Nat. Nanotechnol. 5:67–72
31. Veerman JA, Otter AM, Kuipers L, van Hulst NF. 1998. High definition aperture probes for near-field optical microscopy fabricated by focused ion beam milling. Appl. Phys. Lett. 72:3115–17
32. umurcu A, Diaz J, Lindsay ID, de Beer S, Duvigneau J, Schön P, Vancso GJ. 2015. Optical imaging beyond the diffraction limit by SNEM: effects of AFM tip modifications with thiol monolayers on imaging quality. Ultramicroscopy 150:79–87
33. Yeo B-S, Stadler J, Schmid T, Zenobi R, Zhang W. 2009. Tip-enhanced Raman spectroscopy—its status, challenges and future directions. Chem. Phys. Lett. 472:1–13
34. Agapov RL, Sokolov AP, Foster MD. 2013. Protecting TERS probes from degradation: extending mechanical and chemical stability. J. Raman Spectrosc. 44:710–16
35. Kazemi-Zanjani N, Vedraine S, Lagugne-Labarthet F. 2013. Localized enhancement of electric field in tip-enhanced Raman spectroscopy using radially and linearly polarized light. Opt. Express 21:25271–76
36. Zhang W, Smith T, Yeo B-S, Zenobi R. 2008. Near-field heating, annealing, and signal loss in tip enhanced Raman spectroscopy. J. Phys. Chem. C 112:2104–8
37. Malkovskiy AV, Malkovsky VI, Kisliuk AM, Barrios CA, Foster MD, Sokolov AP. 2009. Tip-induced heating in apertureless near-field optics. J. Raman Spectrosc. 40:1349–54

38. Bechtel HA, Muller EA, Olmon RL, Martin MC, Raschke MB. 2014. Ultrabroadband infrared nanospectroscopic imaging. PNAS 111:7191–96
39. Hermann P, Kästner B, Hoehl A, Kashcheyevs V, Patoka P, Ulrich G, Feikes J, Ries M, Tydecks T, Beckhoff B, Rühl E. 2017. Enhancing the sensitivity of nano-FTIR spectroscopy. Opt. Express 25:16574–88
40. Kehr SC, Cebula M, Mieth O, Härtling T, Seidel J, Grafström S, Eng LM, Winnerl S, Stehr D, Helm M. 2008. Anisotropy contrast in phonon-enhanced apertureless near-field microscopy using a free-electron laser. Phys. Rev. Lett. 100(25):256403
41. Zhang D, Wang X, Braun K, Egelhaaf HJ, Fleischer M, Hennemann L, Hintz H, Stanciu C, Brabec CJ, Kern DP, Meixner AJ. 2009. Parabolic mirror-assisted tip-enhanced spectroscopic imaging for non-transparent materials. J. Raman Spectrosc. 40:1371–76
42. Hermann R, Gordon MJ. 2016. Subdiffraction-limited chemical imaging of patterned phthalocyanine films using tip-enhanced near-field optical microscopy. J. Raman Spectrosc. 47:1287–92
43. Hecht B, Sick B, Wild UP, Deckert V, Zenobi R, Martin OJ, Pohl DW. 2000. Scanning near-field optical microscopy with aperture probes: fundamentals and applications. J. Chem. Phys. 112:7761–74
44. Bozhevolnyi SI, Volkov VS, Søndergaard T, Boltasseva A, Borel PI, Kristensen M. 2002. Near-field imaging of light propagation in photonic crystal waveguides: explicit role of Bloch harmonics. Phys. Rev. B 66:235204
45. Bourzeix SJ, Moison JM, Mignard F, Barthe F, Boccara AC, Licoppe C, Mersali B, Allovon M, Bruno A. 1998. Near-field optical imaging of light propagation in semiconductor waveguide structures. Appl. Phys. Lett. 73:1035–37
46. Koglin J, Fischer UC, Fuchs H. 1997. Material contrast in scanning near-field optical microscopy at 1–10 nm resolution. Phys. Rev. B 55:7977–84
47. Maier SA, Kik PG, Atwater HA, Meltzer S, Harel E, Koel BE, Requicha AA. 2003. Local detection of electromagnetic energy transport below the diffraction limit in metal nanoparticle plasmon waveguides. Nat. Mater. 2:229–32
48. Nabetani Y, Yamasaki M, Miura A, Tamai N. 2001. Fluorescence dynamics and morphology of electroluminescent polymer in small domains by time-resolved SNOM. Thin Solid Films 393:329–33
49. Richards D, Milner RG, Huang F, Festy F. 2003. Tip-enhanced Raman microscopy: practicalities and limitations. J. Raman Spectrosc. 34:663–67
50. Webster S, Batchelder DN, Smith DA. 1998. Submicron resolution measurement of stress in silicon by near-field Raman spectroscopy. Appl. Phys. Lett. 72:1478–80
51. Smith DA, Webster S, Ayad M, Evans SD, Fogherty D, Batchelder D. 1995. Development of a scanning near-field optical probe for localised Raman spectroscopy. Ultramicroscopy 61:247–52
52. Goetz M, Drews D, Zahn DRT, Wannemacher R. 1998. Near-field Raman spectroscopy of semiconductor heterostructures and CVD-diamond layers. J. Lumin. 76–77:306–9
53. Jahncke CL, Paesler MA, Hallen HD. 1995. Raman imaging with near-field scanning optical microscopy. Appl. Phys. Lett. 67:2483–85
54. Burresi M, Kampfrath T, Van Oosten D, Prangsma JC, Song BS, Noda S, Kuipers L. 2010. Magnetic light-matter interactions in a photonic crystal nanocavity. Phys. Rev. Lett. 105:123901
55. Wang Y, Srituravanich W, Sun C, Zhang X. 2008. Plasmonic nearfield scanning probe with high transmission. Nano Lett. 8:3041–45

56. Pettinger B, Domke KF, Zhang D, Schuster R, Ertl G. 2007. Direct monitoring of plasmon resonances in a tip-surface gap of varying width. Phys. Rev. B 76:113409
57. Knoll B, Keilmann F. 2000. Enhanced dielectric contrast in scattering-type scanning near-field optical microscopy. Opt. Commun. 182:321–28
58. Raschke MB, Lienau C. 2003. Apertureless near-field optical microscopy: tip–sample coupling in elastic light scattering. Appl. Phys. Lett. 83:5089–91
59. Raschke MB, Molina L, Elsaesser T, Kim DH, Knoll W, Hinrichs K. 2005. Apertureless near-field vibrational imaging of block-copolymer nanostructures with ultrahigh spatial resolution. Chem Phys Chem 6:2197–203
60. Gerton JM, Wade LA, Lessard GA, Ma Z, Quake SR. 2004. Tip-enhanced fluorescence microscopy at 10 nanometer resolution. Phys. Rev. Lett. 93:180801
61. Jones AC, Berweger S, Wei J, Cobden D, Raschke MB. 2010. Nano-optical investigations of the metal insulator phase behavior of individual VO_2 microcrystals. Nano Lett. 10:1574–81
62. Taylor RS, Leopold KE, Wendman M, Gurley G, Elings V. 1998. Scanning probe optical microscopy of evanescent fields. Rev. Sci. Instrum. 69:2981–87
63. Govyadinov AA, Amenabar I, Huth F, Carney PS, Hillenbrand R. 2013. Quantitative measurement of local infrared absorption and dielectric function with tip-enhanced near-field microscopy. J. Phys. Chem. Lett. 4:1526–31
64. Hillenbrand R, Keilmann F. 2000. Complex optical constants on a subwavelength scale. Phys. Rev. Lett. 85:3029–32
65. Adam P-M, Royer P, Laddada R, Bijeon J-L. 1998. Apertureless near-field optical microscopy: influence of the illumination conditions on the image contrast. Appl. Opt. 37:1814–19
66. Gesuele F, Pang CX, Leblond G, Blaize S, Bruyant A, Royer P, Deturche R, Maddalena P, Lerondel G. 2009. Towards routine near-field optical characterization of silicon-based photonic structures: an optical mode analysis in integrated waveguides by transmission AFM-based SNOM. Phys. E Low-Dimens. Syst. Nanostruct. 41:1130–34
67. Cumurcu A, Duvigneau J, Lindsay ID, Schön PM, Vancso GJ. 2013. Multimodal imaging of heterogeneous polymers at the nanoscale by AFM and scanning near-field ellipsometric microscopy. Eur. Polymer J. 49:1935–42
68. Hillenbrand R, Keilmann F. 2002. Material-specific mapping of metal/semiconductor/dielectric nanosystems at 10 nmresolution by backscattering near-field optical microscopy. Appl. Phys. Lett. 80:25– 27
69. Tranchida D, Diaz J, Schon P, Schonherr H, Vancso GJ. 2011. Scanning near-field ellipsometry microscopy: imaging nanomaterials with resolution below the diffraction limit. Nanoscale 3:233–39
70. Tompkins HG, Irene EA, eds. 2005. Handbook of Ellipsometry. Norwich, NY/Heidelberg, Ger.:William Andrew/Springer
71. Liu Z, Zhang Y, Kok SW, Ng BP, Soh YC. 2013. Reflection-based near-field ellipsometry for thin film characterization. Ultramicroscopy 124:26–34
72. Losurdo M, Hingerl K, eds. 2013. Ellipsometry at the Nanoscale. Berlin: Springer Verlag
73. Ocelic N, Huber A, Hillenbrand R. 2006. Pseudoheterodyne detection for background-free near-field spectroscopy. Appl. Phys. Lett. 89:101124
74. Muller EA, Pollard B, Raschke MB. 2015. Infrared chemical nano-imaging: accessing structure, coupling, and dynamics on molecular length scales. J. Phys. Chem. Lett. 6:1275–84

75. Westermeier C, Cernescu A, Amarie S, Liewald C, Keilmann F, Nickel B. 2014. Sub-micron phase coexistence in small-molecule organic thin films revealed by infrared nano-imaging. Nat. Commun. 5:4101
76. Sarriugarte P, Schnell M, Chuvilin A, Hillenbrand R. 2014. Polarization-resolved near-field characterization of nanoscale infrared modes in transmission lines fabricated by gallium and helium ion beam milling. ACS Photon. 1:604–11
77. Hammiche A, Pollock HM, Reading M, Claybourn M, Turner PH, Jewkes K. 1999. Photothermal FTIR spectroscopy: a step towards FT-IR microscopy at a resolution better than the diffraction limit. Appl. Spectrosc. 53:810–15
78. Dazzi A, Prazeres R, Glotin F, Ortega JM. 2005. Local infrared microspectroscopy with subwavelength spatial resolution with an atomic force microscope tip used as a photothermal sensor. Opt. Lett. 30:2388– 90
79. Lu F, Belkin MA. 2011. Infrared absorption nano-spectroscopy using sample photoexpansion induced by tunable quantum cascade lasers. Opt. Express 19:19942–47
80. Lu F, Jin M, Belkin MA. 2014. Tip-enhanced infrared nanospectroscopy via molecular expansion force detection. Nat. Photon. 8:307–12
81. Rosenberger MR, Wang MC, Xie X, Rogers JA, Nam S, King WP. 2017. Measuring individual carbon nanotubes and single graphene sheets using atomic force microscope infrared spectroscopy. Nanotechnology 28:355707
82. Felts JR, Law S, Roberts CM, Podolskiy V, Wasserman DM, King WP. 2013. Near-field infrared absorption of plasmonic semiconductor microparticles studied using atomic force microscope infrared spectroscopy. Appl. Phys. Lett. 102:152110
83. Centrone A. 2015. Infrared imaging and spectroscopy beyond the diffraction limit. Annu. Rev. Anal. Chem. 8:101–26
84. Dazzi A, Prater CB. 2016. AFM-IR: technology and applications in nanoscale infrared spectroscopy and chemical imaging. Chem. Rev. 117:5146–73
85. Lakowicz JR. 2005. Radiative decay engineering 5: metal-enhanced fluorescence and plasmon emission. Anal. Biochem. 337:171–94
86. Su W, Kumar N, Mignuzzi S, Crain J, Roy D. 2016. Nanoscale mapping of excitonic processes in single-layer MoS2 using tip-enhanced photoluminescence microscopy. Nanoscale 8:10564–69
87. Geddes CD, Lakowicz JR, eds. 2005. Radiative Decay Engineering. Berlin: Springer
88. Kochuveedu ST, Kim DH. 2014. Surface plasmon resonance mediated photoluminescence properties of nanostructured multicomponent fluorophore systems. Nanoscale 6:4966–84
89. Huang B. 2010. Super-resolution optical microscopy:multiple choices. Curr. Opin. Chem. Biol. 14:10–14
90. Yang Z, Aizpurua J, Xu H. 2009. Electromagnetic field enhancement in TERS configurations. J. Raman Spectrosc. 40:1343–48
91. Albrecht AC, Hutley MC. 1971. On the dependence of vibrational Raman intensity on the wavelength of incident light. J. Chem. Phys. 55:4438–43
92. Mock JJ, Barbic M, Smith DR, Schultz DA, Schultz S. 2002. Shape effects in plasmon resonance of individual colloidal silver nanoparticles. J. Chem. Phys. 116:6755–59
93. Barrios CA, Malkovskiy AV, Kisliuk AM, Sokolov AP, Foster MD. 2009. Highly stable, protected plasmonic nanostructures for tip enhanced Raman spectroscopy. J. Phys. Chem. C 113:8158–61

94. Park KD, Kim YH, Park JH, Park JS, Lee HS, Yim SY, Lee YH, Jeong MS. 2012. Ultraviolet tip-enhanced nanoscale Raman imaging. J. Raman Spectrosc. 43:1931–34
95. Scherger JD, Foster MD. 2017. Tunable, liquid resistant tip enhanced Raman spectroscopy probes: toward label-free nano-resolved imaging of biological systems. Langmuir 33:7818–25
96. Johns RW, Bechtel HA, Runnerstrom EL, Agrawal A, Lounis SD, Milliron DJ. 2016. Direct observation of narrow mid-infrared plasmon linewidths of single metal oxide nanocrystals. Nat. Commun. 7:11583
97. Liao M, Jiang S, Hu C, Zhang R, Kuang Y, Zhu J, Zhang Y, Dong Z. 2016. Tip-enhanced Raman spectroscopic imaging of individual carbon nanotubes with sub-nanometer resolution. Nano Lett. 16:4040–46
98. Ramos R, Gordon MJ. 2012. Reflection-mode, confocal, tip-enhanced Raman spectroscopy system for scanning chemical microscopy of surfaces. Rev. Sci. Instrum. 83:093706
99. Berweger S, Neacsu CC, Mao Y, Zhou H, Wong SS, Raschke MB. 2009. Optical nanocrystallography with tip-enhanced phonon Raman spectroscopy. Nat. Nanotechnol. 4:496–99
100. Ossikovski R, Nguyen Q, Picardi G. 2007. Simple model for the polarization effects in tip-enhanced Raman spectroscopy. Phys. Rev. B 75:045412
101. Sun M, Zhang Z, Chen L, Sheng S, Xu H. 2014. Plasmonic gradient effects on high vacuum tip-enhanced Raman spectroscopy. Adv. Opt. Mater. 2:74–80
102. Zhang Z, Sun M, Ruan P, Zheng H, Xu H. 2013. Electric field gradient quadrupole Raman modes observed in plasmon-driven catalytic reactions revealed by HV-TERS. Nanoscale 5:4151–55
103. Neacsu CC, Berweger S, Raschke MB. 2007. Tip-enhanced Raman imaging and nanospectroscopy: sensitivity, symmetry, and selection rules. NanoBiotechnology 3:172–96
104. Eustis S, El-Sayed MA. 2005. Why gold nanoparticles are more precious than gold. Chem. Soc. Rev. 35:209–17
105. Park KD, Muller EA, Kravtsov V, Sass PM, Dreyer J, Atkin JM, Raschke MB. 2016. Variable-temperature tip-enhanced Raman spectroscopy of single-molecule fluctuations and dynamics. Nano Lett. 16:479–87
106. Becker SF, Esmann M, Yoo K, Gross P, Vogelgesang R, Park N, Lienau C. 2016. Gap-plasmon-enhanced nanofocusing near-field microscopy. ACS Photon. 3:223–32
107. Pettinger B, Domke KF, Zhang D, Picardi G, Schuster R. 2009. Tip-enhanced Raman scattering: influence of the tip-surface geometry on optical resonance and enhancement. Surf. Sci. 603:1335–41
108. Heilman AL, Gordon MJ. 2016. Tip-enhanced near-field optical microscope with side-on and ATR mode sample excitation for super-resolution Raman imaging of surfaces. J. Appl. Phys. 119:223103
109. Pettinger B. 2010. Single-molecule surface- and tip-enhanced Raman spectroscopy. Mol. Phys. 108:2039– 59
110. Zhang R, Zhang Y, Dong ZC, Jiang S, Zhang C, Chen LG, Zhang L, Liao Y, Aizpurua J, Luo YE, Yang JL. 2013. Chemical mapping of a single molecule by plasmon-enhanced Raman scattering. Nature 498:82–86

111. Zhu W, Esteban R, Borisov AG, Baumberg JJ, Nordlander P, Lezec HJ, Aizpurua J, Crozier KB. 2016. Quantum mechanical effects in plasmonic structures with subnanometre gaps. Nat. Commun. 7:11495
112. Chen C, Hayazawa N, Kawata S. 2014. A 1.7 nm resolution chemical analysis of carbon nanotubes by tip-enhanced Raman imaging in the ambient. Nat. Commun. 5:3312
113. Chiang N, Chen X, Goubert G, Chulhai DV, Chen X, Pozzi EA, Jiang N, Hersam MC, Seideman T, Jensen L, Van Duyne RP. 2016. Conformational contrast of surface mediated molecular switches yields angstrom-scale spatial resolution in ultrahigh vacuum tip-enhanced Raman spectroscopy. Nano Lett. 16:7774–78
114. Richard-Lacroix M, Zhang Y, Dong Z, Deckert V. 2017. Mastering high resolution tip-enhanced Raman spectroscopy: towards a shift of perception. Chem. Soc. Rev. 46:3922–44
115. Bouhelier A, Beversluis M, Hartschuh A, Novotny L. 2003. Near-field second-harmonic generation induced by local field enhancement. Phys. Rev. Lett. 90:013903
116. Ikeda K, Saito Y, Hayazawa N, Kawata S, Uosaki K. 2007. Resonant hyper-Raman scattering from carbon nanotubes. Chem. Phys. Lett. 438:109–12
117. Kravtsov V, Ulbricht R, Atkin JM, Raschke MB. 2016. Plasmonic nanofocused four-wave mixing for femtosecond near-field imaging. Nat. Nanotechnol. 11:459–64
118. Kumar N, Mignuzzi S, Su W, Roy D. 2015. Tip-enhanced Raman spectroscopy: principles and applications. EPJ Tech. Instrum. 2:9
119. Verma P. 2017. Tip-enhanced Raman spectroscopy: technique and recent advances. Chem. Rev. 117:6447–66
120. Zhang Z, Sheng S, Wang R, Sun M. 2016. Tip-enhanced Raman spectroscopy. Anal. Chem. 88:9328–46

Chapter II. Construction and Validation of a Custom-built Near-field Optical Microscope

Adapted from: R. J. Hermann and M. J. Gordon, “Sub-diffraction limited chemical imaging of patterned phthalocyanine films using tip-enhanced near-field optical microscopy”, *Journal of Raman Spectroscopy*, 2016, vol. 47, pgs. 1287–1292.

Abstract

A tip-enhanced near-field optical microscope, based on a shear-force atomic force microscope with plasmonic tip coupled to an inverted, confocal optical microscope, has been constructed for nanoscale chemical (Raman) imaging of surfaces. The design and validation of the instrument, along with its application to near-field Raman mapping of patterned organic thin films (coumarin-6 and Cu(II) phthalocyanine), are described. Lateral resolution of the instrument is estimated at 50 nm (better than $\lambda/10$), which is roughly dictated by the size of the plasmonic tip apex. Additional measurements include the distance scaling of Raman enhancement and the inelastic scattering background generated by the plasmonic tip.

A. Introduction

This work discusses the design of a tip-enhanced near-field optical microscope capable of reproducible chemical- and structure-specific vibrational *imaging* of surfaces at the nanoscale. The instrument is built from the combination of a commercial optical microscope and custom-built shear-force atomic force microscope (AFM). Design choices intended to maximize the signal-to-noise ratio of near vs. far-field optical signals, such as the conversion of excitation light to a radially-polarized state, are explained in detail. Unambiguous evidence for the instrument's ability to generate and collect near-field optical signals is provided by chemical hyperspectral Raman imaging of a patterned Cu(II) phthalocyanine film at spatial resolutions below 50 nm ($\lambda/10$). Quantitative measurements of near-field enhancement factors, near-field tip-sample distance scaling, background spectral contributions, and instrument stability are also reported.

B. Designing a near-field microscope

The foundation of the tip-enhanced near-field optical microscope (TENOM) developed consists of a custom-built shear-force AFM mounted onto a Nikon Epiphot 300 metallurgical microscope. The microscope follows an inverted geometry with a 1.25 numerical aperture (NA) oil-immersion objective being used to focus light onto and collect light from the sample surface. The cost of an inverted geometry is that sample substrates must be transparent, but this is offset by an increase in the optical efficiency of the system. For example, the solid angle of collection of the 1.25 NA lens being used is nearly 120°, ensuring collection of a majority of light scattered into the substrate. Another advantage of an oil lens is that the size of the minimum diffraction spot is inversely proportional to the

NA. For near-field experiments it is critical to minimize this spot size in order to reduce the magnitude of scattering by analytes that are not in the vicinity of the tip. This optical configuration achieves a diffraction limited, focused laser spot at the sample with a size of ~250x250 nm^2, as demonstrated in **Figure 2.2(a)** by scanning a 100 nm fluorescent polystyrene bead through the laser focus

A radial polarizer (Altechna S-waveplate), center beam stop, and adjustable iris on the pump path are used to inject a ring-shaped beam of radially polarized light into the back of the objective. Radial polarization and high angle light injection from the objective are used to maximize the axial-to-lateral polarization intensity ratio at the tip; axial polarization contributes to the main dipole mode of the tip, while lateral polarization does not [1-2]. as shown schematically in **Figure 2.1**. Pump light (647 nm from a Kr$^+$ laser) is delivered to the rear of the microscope via a single mode fiber, where it is expanded, filtered, polarized and then reflected off a dichroic mirror into the rear of the objective lens.

The objective lens is mounted on a piezoelectric element for vertical focus control that fully replaces the original microscope coarse/fine manual focusing equipment. The piezoelectric mount is compatible with automated control via LabView and offers spatial precisions <100 nm. Light generated by the sample is collected with the same microscope objective, passes through the dichroic (650 nm high pass) beamsplitter and high pass Raman filter, and is focused on a 100 µm core collection fiber that acts as a confocal aperture [see **Fig. 2.2(b)**], spatially filtering out light that is not generated directly at the focal plane of the objective lens (i.e. the sample surface). The collected light is passed to a 320mm f/4.1 Horiba JY monochromator with TE-cooled CCD and PMT detectors.

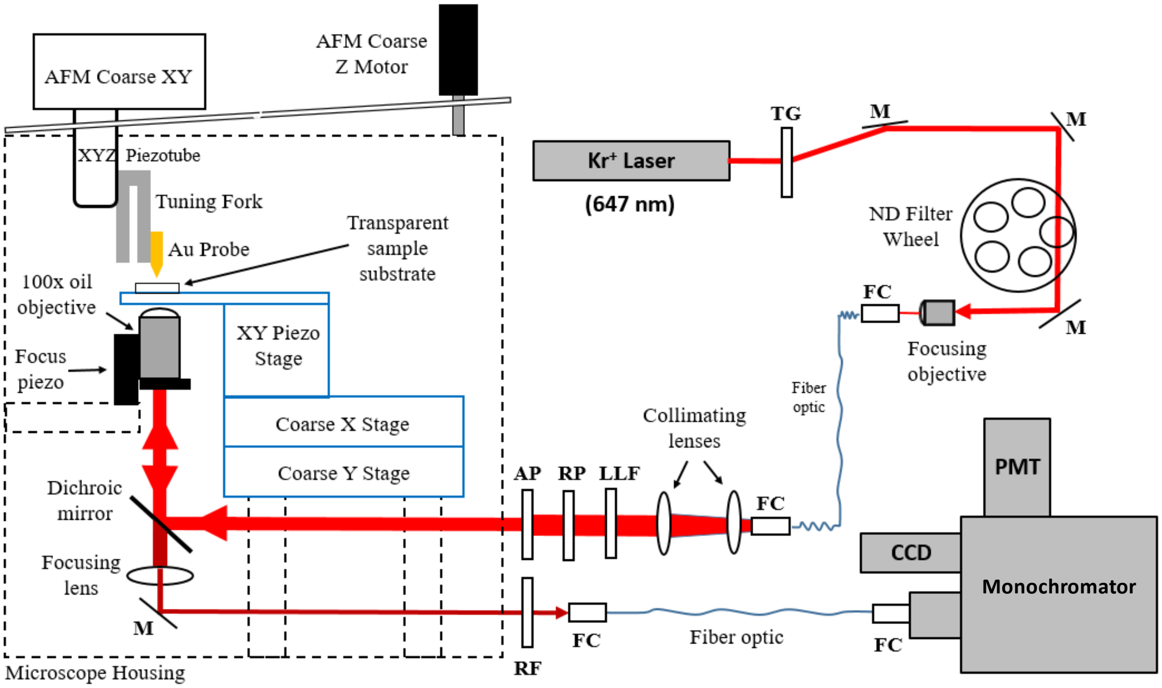

Figure 2.1 Schematic of the tip-enhanced near-field optical microscope developed in this work. TG=transmission grating; M=mirror; FC=fiber couple; LLF=laser line filter; RP=radial polarizer; AP=aperture; RF=Raman filter.

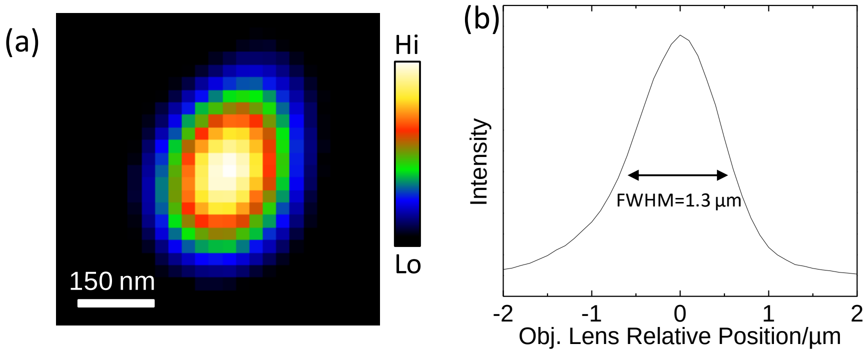

Figure 2.2 (a) Integrated fluorescence image of a 170 nm bead being raster scanned through the focused laser. The average FWHM value of the slightly oblong spot is 250 nm. (b) Integrated fluorescence intensity as the sample is scanned vertically through the microscope objective focal plane. Note, the microscope was made confocal using a 100 µm dia. collection fiber as a pinhole.

The custom-built SPM atop the optical microscope is based on an electrically excited quartz tuning fork oscillator (~2^{15} Hz) with phase-locked loop (PLL) controller (Zurich Instruments

HF2). Shifts in the amplitude and phase response of the tuning fork occur as a function of tip-surface forces. In particular, a constant phase setpoint is maintained during surface regulation using a PID control loop with the vertical piezotube voltage the tuning fork is mounted to as the output value. The noise floor of the AFM has been measured to be on the order of 1 nm across many sample surfaces. For additional details on the operation and physics behind shear-force AFM, refer to Appendix A2.3.

Au tips (apex diameter = 40-60 nm) were formed by electrochemically etching fine Au wires in ethanol/HCl using a constant voltage supply [3], and were then glued to the free tine of a quartz tuning fork. Forks were attached to an XYZ piezo tube scanner (35x35x5 μm^3) and coarse XY positioner. Shear-force feedback, where the tip oscillates parallel to the sample surface, was used for imaging. Coarse Z positioning of the tip for sample approach was provided by a gear-reduced stepper motor. After visual alignment of the tip with the microscope focus using the backscattered laser light pattern, the sample was raster scanned using a closed loop piezo XY stage to form an image. Acquisition of spatially correlated topography and spectroscopy data were synchronized using Labview control of the PLL, piezo scan stages, monochromator, and CCD camera.

C. Experimental validation of TENOM instrument

(i) Inelastic scattering from plasmonic Au tips

Optical interrogation of surfaces using metallic (plasmonic) SPM tips can result in large fluorescence backgrounds that are thought to be due to inelastic scattering from the tip itself [4]. Evidence for this comes from inelastic scattering (i.e., radiative plasmon decay) measurements on metallic nanoparticles, where the quantum efficiency is typically in the 10^{-4}-10^{-6} range [5]. Although this emission rate is low, these broad signals can still overwhelm the relatively weak Raman scattering coming from the surface. As such, it was important to characterize how tip-related photoluminescence affected our near-field optical experiments. To this end, PL spectra [**Fig. 2.3(a)**] were acquired by raster scanning the TENOM tip, engaged on a glass cover slip, in XY through the laser focus. An image was then formed by integrating the PL signal (250-2200 cm^{-1} shift from the pump line) at each pixel [**Fig. 2.3(b)**]. A consistent background signal was observed with a magnitude that strongly depended on the relative position of the tip in the laser spot, implying that the signal was generated by the tip. Once this background was identified, it could be subtracted from near-field spectra and image data.

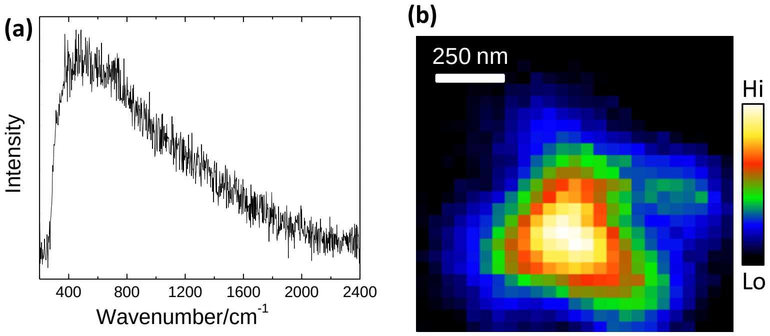

Figure 2.3 (a) Inelastic scattering spectrum from an Au tip illuminated with 647 nm light. The spectrum is primarily attributed to radiative decay from a distribution of supported surface plasmon modes. (b) Integrated scattering intensity as the tip is raster scanned through the laser spot. A maximum is observed when the tip apex is aligned with the center of the focused laser spot.

(ii) Near-field spectroscopy of coumarin-6 films

The distance dependence and enhancement of Raman, Rayleigh, and tip-related PL signals were evaluated using an Au tip and 5 nm thick film of coumarin-6 on glass [**Fig. 2.4**]. Coumarin-6 was chosen because of its lack of absorption at 647 nm [6] to specifically avoid any resonant Raman effects on signal levels. When the tip was regulated on the surface [nominally z=0, see Appendix A2.3 for an estimate of the real tip-surface distance], distinct Raman peaks from the organic were seen above the broad tip-generated PL background [**Fig. 2.4(a)**]. When the tip was fully retracted, no Raman peaks were observed using the same 1 s collection time [z=2 µm, **Fig. 2.4(a)**]. Increasing the collection time to 30 s allowed some peaks to again be resolved, and from this the near-field enhancement factor was estimated to lie between 10^3-10^4 [calculation details given in Appendix A2.2]. Another important data point was obtained when the tip was retracted only 10 nm from the dye-coated surface. The intensity of the observed Raman peaks decreased by nearly 60%, which is strong evidence for the existence of intense, localized optical fields at the tip apex. This is further supported by examining multiple spectra collected as the tip was further retracted from the surface in 10 nm increments [**Fig. 2.4(b)**]. The near-field Raman signal decreased much more rapidly than the back-scattered Rayleigh or tip PL signals, both of which can be understood as far-field effects caused by the tip moving out of the microscope focal plane.

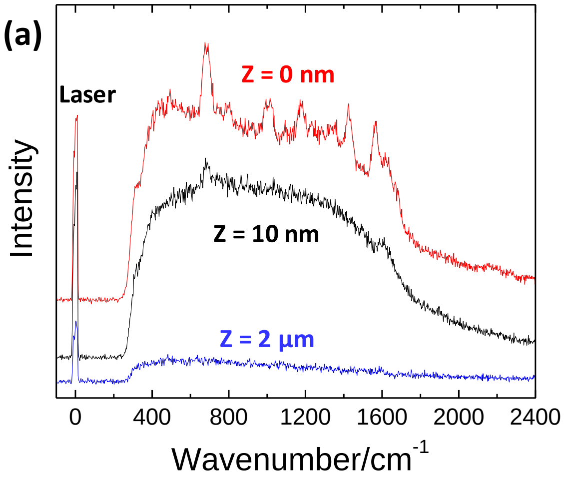

Figure 2.4 (a) Near-field spectra of a 5 nm thick coumarin-6 film on a glass coverslip taken when the tip is regulated on the sample surface (z=0 nm), slightly retracted (z=10 nm), and fully retracted (z=2 μm). (b) Integrated optical signals as a function of tip-surface distance; Raman=685 cm^{-1} peak only, Rayleigh=laser line, tip background=200-2400 cm^{-1}.

Using the same coumarin-6 sample, large variations in Raman peak intensities were observed at different positions along the film. For example, **Figure 2.5** shows several tip-enhanced coumarin-6 Raman spectra taken along a single scan line at 50 nm pitch, where the magnitudes of multiple peaks change dramatically from spectrum to spectrum. In fact, spectra 1-2 and 3-4 are each separated by only a single 50 nm step. Partial peak assignments have been made using published spectra for benzothiazole and coumarine-152 to approximate the 2-benzothiazolyl and 7-(diethylamino)coumarin moieties of the coumarin-6 molecule, as detailed in Appendix A2.1. Several peaks in the spectra could not be identified, and as such, partial decomposition of coumarin-6 cannot be ruled out. Either the thermal evaporation process or local heating caused by the Au probe could be responsible for the formation of decomposition products. This highly localized spectroscopic data is insightful (i.e., relative Raman peak intensities can provide information about local molecular orientation, contamination, etc.), but it can also make direct 'pixel-by-pixel' chemical identification and/or quantification of heterogeneous surfaces more challenging.

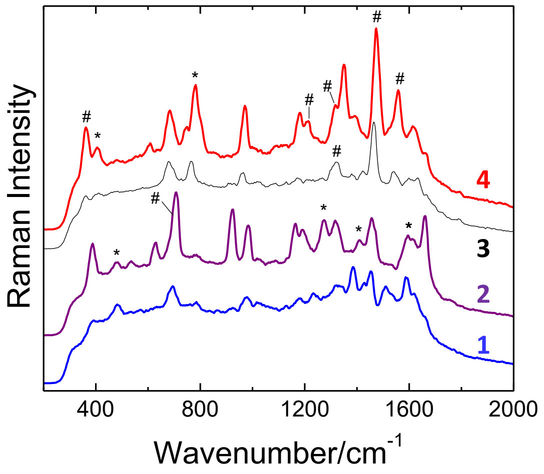

Figure 2.5 Tip-enhanced Raman spectra collected at various locations during a line scan of a coumarin-6 film. Spectra 1-2 and 3-4 were separated by a single 50 nm step. # and * denote Raman peaks associated with the 2-benzothiazolyl and 7-(diethylamino)coumarin moieties of the coumarin-6 molecule, respectively [details in Appendix A2.1].

(iii) Nanoscale optical imaging of patterned phthalocyanine films

One of the primary design goals for our TENOM was to collect full two-dimensional, chemically-specific spectral images of a surface with sub-diffraction limited spatial resolution. To test this capability, model surfaces covered with Cu(II) phthalocyanine (CuPc) nanotriangles (5 nm high x 200 nm on a side) were created using colloidal lithography (1 μm silica spheres) and thermal evaporation [**Fig. 2.6(a)**]. Nanopatterned thin films of CuPc (Sigma-Aldrich) were formed on glass via thermal evaporation (10^{-5} torr) using a colloidal crystal masking process (1 μm silica spheres) that has been described elsewhere [7]. Since the strength of the optical near-field formed at the tip apex decays rapidly with distance [8], the evaporated films were intentionally made only 5 nm thick. Two benefits of this are that absorption in the film is kept to a minimum, and the ratio of near to far-field scattering is high. After evaporation of the organic, the colloidal mask was selectively removed by sonicating the sample in water.

A collected far-field Raman spectrum from this sample [**Fig. 2.6(b)**] agrees well with published data [6], indicating the dye has not been damaged during evaporation. When the tip is engaged on a nanotriangle, a subset of the far-field CuPc spectrum peaks are observed to be strongly enhanced. Chemical and vibrational mode-specific images of the surface can then be obtained by raster-scanning the sample through the tip-laser focus and recording a full Raman spectrum at every pixel. For example, **Figure 2.6(d-f)** shows tip-enhanced near-field Raman maps of the surface created by integrating all Raman peaks from 500-1650 cm^{-1}, the strong 1540 cm^{-1} peak due to the isoindole stretch, and the weaker 625-800 cm^{-1} ring breathing modes of the CuPc macrocycle. Note that the tip PL background has been subtracted when forming these images, and that a correction for small drifts in the tip-laser alignment has been made by normalizing each pixel intensity value by its corresponding backscattered Rayleigh signal. In each TENOM Raman image, the underlying triangular array structure seen in the topography scan is present, demonstrating that chemically-specific, super resolution optical imaging of a heterogeneous organic thin film is feasible. Moreover, TENOM allows optical imaging of a single Raman mode using modest acquisition times (500 ms/pixel) and sample pump powers (500 μW).

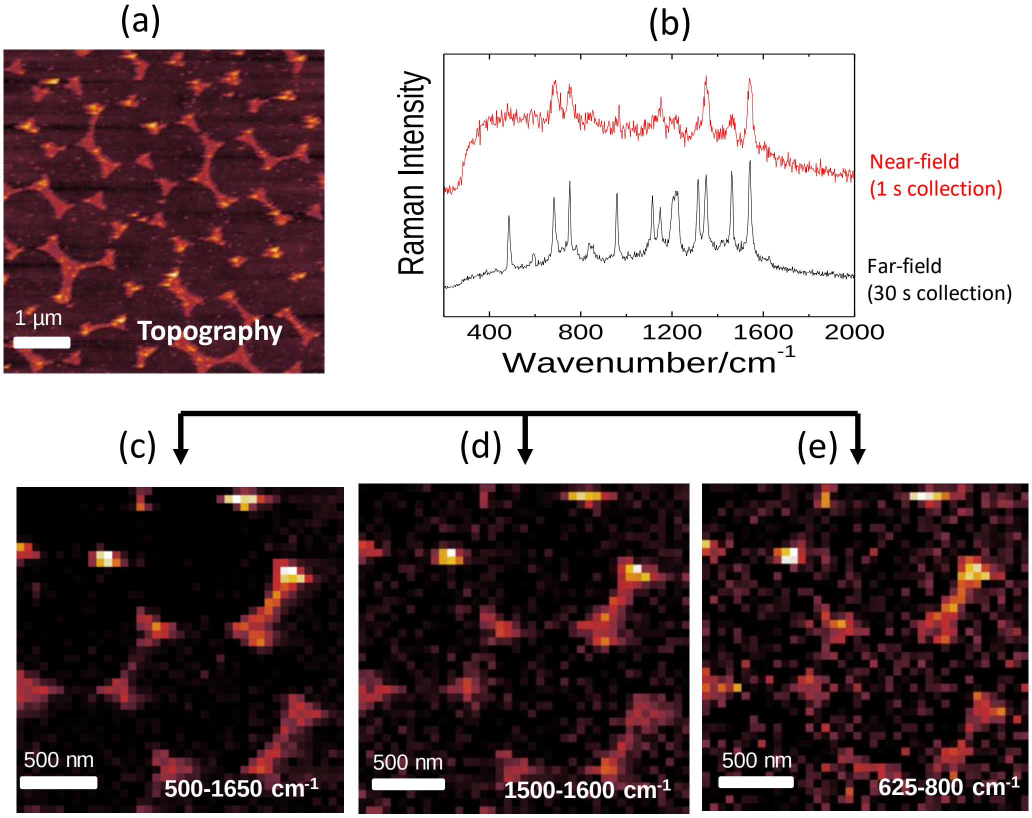

Figure 2.6 (a) Topography image of a 5 nm thick CuPc pattern after mask removal. (b) The associated far-field Raman spectrum showing the dye has not been damaged during the evaporation process and a representative tip-enhanced Raman spectrum collected over a CuPc triangle. Three spectral images were formed using different integration ranges: (c) all observed vibrational peaks, (d) isoindole group stretching, and (e) macrocycle breathing modes [6]. Note that the broad tip PL background has been subtracted from these images.

Looking at linecut profiles from the TENOM Raman image, the lateral resolution is estimated at 50 nm ($< \lambda/10$), or approximately the size of the tip apex. If wavenumber is plotted against relative position for one such linecut [Fig. 2.7(b)], a hyperspectral image can be created that shows the distinct pattern of Raman peaks for CuPc turning on and off as the tip passes over a surface feature. This latter image illustrates the type of pattern recognition that may be possible for analysis of a multi-component sample. For example, each pixel would be scored according to the similarity of its spectra to those of various known patterns;

pixels with a sufficiently high score could then be classified as a particular material, allowing multi-component 'chemical' maps of a surface to be created in one imaging pass.

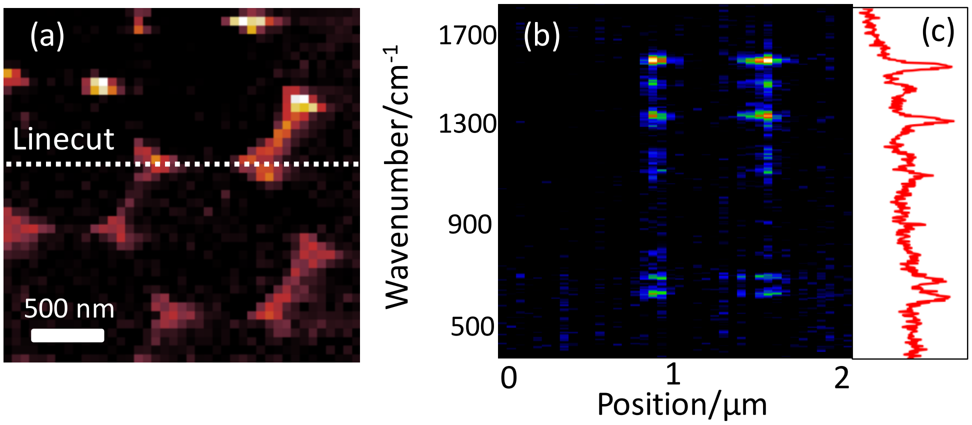

Figure 2.7 (a) TENOM Raman image of CuPc nanotriangles (500-1650 cm^{-1}). (b) Hyperspectral image showing wavenumber vs. position data taken from the indicated linecut in (a). A distinct pattern of Raman peaks (c) becomes visible only when the tip passes over regions of CuPc.

D. Conclusions

In this work, we presented the design, validation, and application of a tip-enhanced near-field optical microscope for all-optical, chemically-specific imaging of surfaces at super resolutions. The microscope was built around a tuning fork-based shear force AFM attached to an inverted optical microscope with confocal pumping and collection. Non-resonant Raman enhancement factors with the plasmonic Au tip were estimated in the 10^3-10^4 range using a coumarin-6 film. Raman signals from the surface, in contrast to Rayleigh and inelastic scattering from the tip, were seen to quickly decay as the tip was removed from the surface. Reproducible 2D spectral and hyperspectral imaging of nanopatterned Cu(II) phthalocyanine thin films was also demonstrated at lateral resolutions of 50 nm (better than $\lambda/10$). Moreover, given the SNR of tip-enhanced Raman signals, efforts will now be made to collect vibrational Raman images of more complex, multi-component surfaces with both chemical and structural heterogeneity at super resolutions.

References

1. Kazemi-Zanjani, N.; Vedraine, S.; Lagugné-Labarthet, F., Localized enhancement of electric field in tip-enhanced Raman spectroscopy using radially and linearly polarized light. *Optics express* **2013,** *21* (21), 25271-25276.
2. Pashaee, F.; Hou, R.; Gobbo, P.; Workentin, M. S.; Lagugné-Labarthet, F. o., Tip-enhanced Raman spectroscopy of self-assembled thiolated monolayers on flat gold nanoplates using Gaussian-Transverse and radially polarized excitations. *The Journal of Physical Chemistry C* **2013,** *117* (30), 15639-15646.
3. Ren, B.; Picardi, G.; Pettinger, B., Preparation of gold tips suitable for tip-enhanced Raman spectroscopy and light emission by electrochemical etching. *Review of Scientific Instruments* **2004,** *75* (4), 837-841.
4. Neacsu, C. C.; Berweger, S.; Raschke, M. B., Tip-enhanced Raman imaging and nanospectroscopy: sensitivity, symmetry, and selection rules. *NanoBiotechnology* **2007,** *3* (3-4), 172-196.
5. Eustis, S.; El-Sayed, M. A., Why gold nanoparticles are more precious than pretty gold: noble metal surface plasmon resonance and its enhancement of the radiative and nonradiative properties of nanocrystals of different shapes. *Chemical society reviews* **2006,** *35* (3), 209-217.
6. Reynolds, G.; Drexhage, K., New coumarin dyes with rigidized structure for flashlamp-pumped dye lasers. *Optics Communications* **1975,** *13* (3), 222-225.
7. Lora Gonzalez, F.; Chan, L.; Berry, A.; Morse, D. E.; Gordon, M. J., Simple colloidal lithography method to fabricate large-area moth-eye antireflective structures on Si, Ge, and GaAs for IR applications. *Journal of Vacuum Science & Technology B, Nanotechnology and Microelectronics: Materials, Processing, Measurement, and Phenomena* **2014,** *32* (5), 051213.
8. Pettinger, B.; Domke, K. F.; Zhang, D.; Picardi, G.; Schuster, R., Tip-enhanced Raman scattering: influence of the tip-surface geometry on optical resonance and enhancement. *Surface Science* **2009,** *603* (10-12), 1335-1341.

Appendix (A2)

A2.1 Peak identification for coumarin-6 spectra

Several of the Raman peaks seen in the tip-enhanced, near-field spectra of a coumarin-6 film (Fig. 2.5 in the main text) can be attributed to the 2-benzothiazolyl (Bt) and 7-(diethylamino)coumarin (C) moieties of the coumarin-6 molecule as outlined below. We have attempted to assign these peaks using Raman data for benzothiazole [1] and coumarin-152 (i.e., 7-(dimethylamino)-4-(trifluoromethyl)-2H-chromen-2-one) [2] in Table A2.1. The peaks in Figure 2.5 annotated with # or * are not directly assignable to specific vibrations of Bt or C. This analysis does not rule out the possibility that some level of coumarin-6 decomposition could have occurred, either during thermal evaporation or from local heating during TENOM measurements, and that any decomposition products may account for these unassigned peaks.

Table A2.1. Raman peak assignments for coumarin-6 spectra in Fig. 5 of the main text. The letters B and L in the assignment descriptions refer to the benzene and lactone ring substituents of 7-(diethylamino)coumarin.

Peak Location [cm^{-1}]	Moiety	Assignment
1598	C	combination 8a modes of B and L rings
1562	Bt	C-H in plane bending
1476	Bt	C-H in plane bending
1412	C	C_7-N & C_{4a}-C_4 stretch + CH_3 in phase sym. bend
1320	Bt	C-C stretching
1291	Bt	C-C stretching
1272	C	C_{8a}-O & C_2-C_3 stretch + N-(CH_3) asym. stretch + B ring deformation
1210	Bt	C-H in plane bending
783	C	12(L) + 6a(B) + $(CH_3)_2$>N-C_7 sym. stretch
706	Bt	C-C-C ring breathing
482	C	skeletal deform along (C=O)-C_{8a} axis
400-405	C	$(CH_3)_2$-N bend + C=O rock + skeletal in plane deformation
360	Bt	ring stretching

A2.2 Coumarin-6 enhancement factor calculation

The enhancement factor was estimated by estimating the far-field to near-field probe area ratio at 25:1, corresponding to 250^2:50^2 nm^2. These values come from a point spread function map using a fluorescent bead [Fig. 2.3b] and an SEM image [not shown] of the particular Au tip used in this experiment with an apex diameter of roughly 50 nm. An area ratio, instead of a volume ratio, is adequate in this case as the film is very thin (<10 nm) such that all molecules in the z-direction were assumed to be probed in both cases. A 5x ratio of Raman signal intensities was computed using characteristic near-field [Fig. A2.1 (a)] and far-field spectra [Fig. A2.1(b)]. Since several peaks were present in only the near or far-field spectra, but not both, all peaks in the 400 cm^{-1} to 1800 cm^{-1} range were integrated for this calculation. The background fluorescence or Au tip photoluminescence was subtracted out in both cases. Finally, the far-field collection time was 30 s compared to 1 s for the near-field, resulting in an additional 30x factor. The total enhancement factor (EF) was thus computed as follows: EF = 25 * 5 * 30 = 3750. Due to the very approximate nature of this calculation, the reported EF value was placed between the two nearest order of magnitude values, 10^3-10^4.

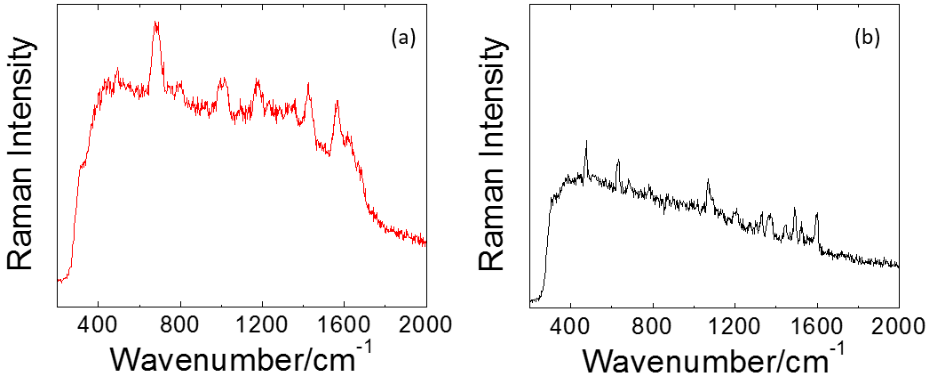

Figure A2.1 Coumarin-6 spectra used when estimating the enhancement factor. (a) Tip engaged on film; 1 s collection. (b) Tip retracted by 100+ µm; 30 s collection. The laser power was the same for both measurements.

A2.3 Estimating the tip-surface distance using shear-force AFM

In shear-force AFM, there is no simple method for measuring the real distance between the tip and surface at a given feedback set point (e.g., phase, amplitude, or resonance frequency shift). In the case of TENOM, this is problematic as the fields generated at the tip apex vary over short length scales, and hence the signal enhancement could be sensitive to the set point value chosen. We have performed a relatively simple experiment that gives an upper limit on the tip-sample distance when the tip is "engaged" on the surface. The procedure involves slowly lowering the tip onto the surface while recording changes in the phase/amplitude of the tuning fork-tip oscillator when it is excited at constant frequency. We will refer to this procedure as a “tip run-in”. The analysis presented here uses the oscillator phase data only, although a very similar procedure could be performed using amplitude data. Figure A2.2 shows the phase values recorded during one run-in experiment in which a tip was lowered onto a glass coverslip surface.

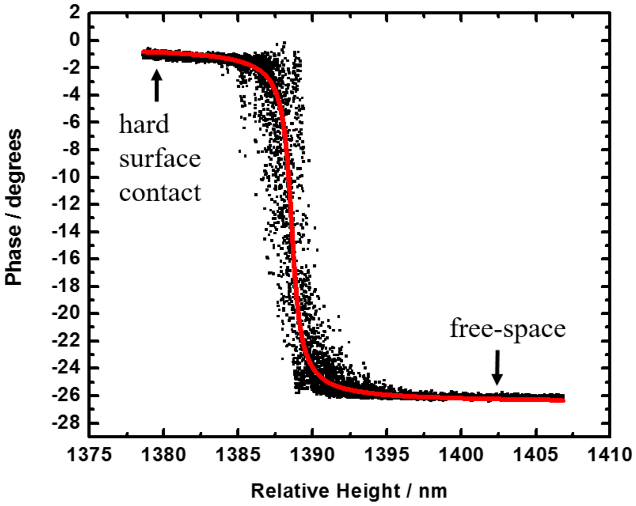

Figure A2.2

Phase of an oscillating tip-tuning fork system as it is slowly lowered onto a glass coverslip. A transition between no surface interaction (free-space) and hard surface contact is observed. The red line is an inverse tangent function that has been fit to the data.

The data above show two regions in which phase is nearly constant and a transition region between them. This is interpreted as observing the change between the tip not touching the surface at all (free-space limit) and making hard surface contact. We believe the noise present in the transition region of the dataset is due to real variations in the tip-surface distance caused by vibrations in the laboratory environment.

The observed phase shift of the tip-tuning fork oscillator upon surface contact can be understood as a shift in frequency space of the resonance mode. In fact, the resonance can be directly measured and compared for each limiting case. Figure A2.3 shows how the resonance frequency, corresponding to the amplitude maximum or central phase inflection point, is found to increase by 90 Hz upon surface contact. This data agrees well with an earlier study by Ruiter et al. [3], in which the same type of run-in experiment was performed.

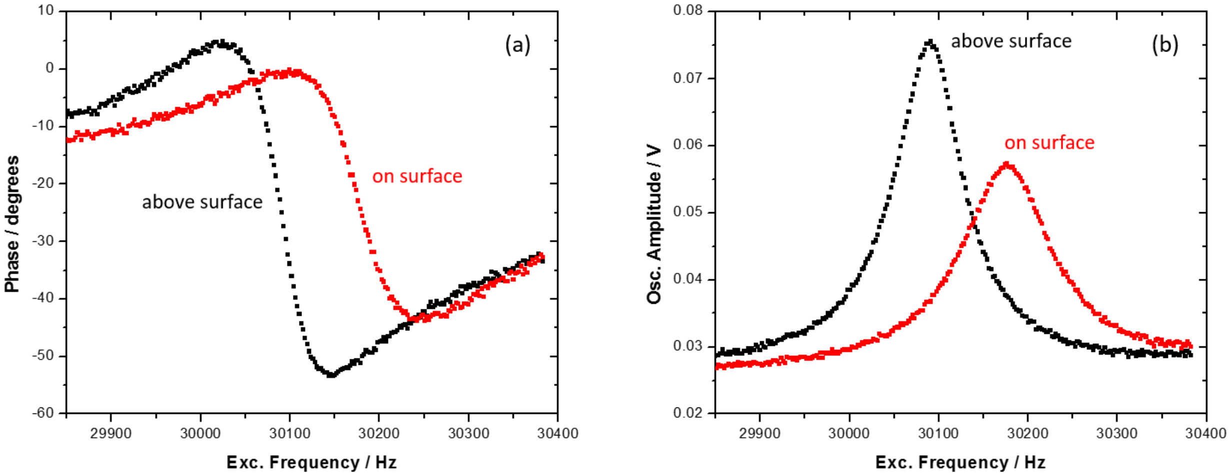

Figure A2.3 Frequency sweeps showing a shift in the (a) phase and (b) oscillation amplitude of the tip-tuning fork oscillator upon surface contact.

We now make an assumption that will allow us to connect the phase vs. distance data in Figure A2.2 to the phase vs. frequency data in Figure A2.3(a). The assumption is that changes in the phase resonance can be approximated as a simple shift of the free-space resonance along the frequency axis, i.e., the so-called linear regime. It is clear from Figure A2.3(a) that this is only a first order approximation, as both the slope and magnitude of the phase resonance change to some degree during surface contact. We proceed to convolute Figure A2.2 and Figure A2.3(a) along their shared phase axis to obtain a new frequency shift vs. distance curve [Fig. A2.4], where frequency shift is the difference between the local and free-space resonance frequencies. There are two marked positions: (1) the 2.5 Hz set point that was used for TENOM experiments in this work, and (2) the position where the frequency shift is 90% of its maximum value in this range. The distance between these positions is 3 nm, which can be taken as an upper bound on the tip-surface distance under experimental conditions.

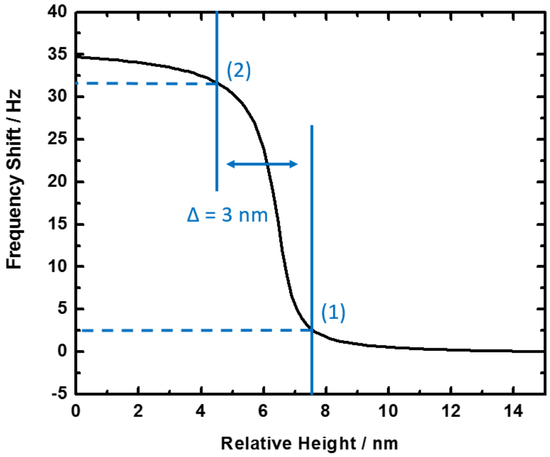

Figure A2.4

Approximate model of frequency shift vs. distance obtained by convoluting the data in Fig. A2.2 with the free-space phase resonance [Fig. A2.3(a)]. The distance between positions (1) and (2) represents a conservative estimate of the real tip-surface distance at the experimental frequency shift set point of 2.5 Hz.

Appendix 2 References

1. V. Sathyanarayanmoorthi, R. Karunathan, and V. Kannappan, *Hindawi Journal of Chemistry*, 2013, 258519.
2. Vogel, E., Gbureck, A., and W. Kiefer, *J. Molec. Struct*., 2000, **177**, 550.
3. A. Ruiter, K. van der Werf, J. Veerman, M. Garcia-Parajo, W. Rensen, and N. van Hulst, *Ultramicroscopy*, 1998, **71**, 149.

Chapter III. Imaging Intermolecular Exciton Coupling in Metal-free Phthalocyanine Nanofilms

Adapted from: R. J. Hermann and M. J. Gordon, "Imaging intermolecular exciton coupling in metal-free phthalocyanine nanofilms using tip-enhanced near-field optical microscopy", *Journal of Physical Chemistry C*, 2018, vol. 122, pgs. 14796-14804.

Abstract

Spatially correlated topography, fluorescence, and Raman scattering signals of metal-free phthalocyanine (H_2Pc) nanofilms were imaged using confocal and tip-enhanced (fluorescence and Raman) near-field optical microscopy at lateral spatial resolutions of 500 nm and ∼25 nm, respectively. The far-field fluorescence intensity was found to vary inversely with film thickness up to 10 nm, with the strongest emission coming from isolated H_2Pc molecules on samples with submonolayer coverage. Changes in the fluorescence energy distribution were imaged and were consistent with exciton coupling predictions for H_2Pc molecules lying edge-to-edge on the surface. Thicker H_2Pc films (>10 nm) were found to consist entirely of nonfluorescing aggregates and crystal domains. Tip-enhanced near-field measurements were carried out with W and Au (plasmonic) tips to investigate the local optical properties of H_2Pc films and nanostructures. In general, fluorescence increased by a factor of 2−3× compared to the far-field when the tip was engaged; these signal levels suggest a local enhancement factor of 500×. However, the fluorescence was seen to increase by ∼50% when the tip was lifted 10 nm above the surface, indicating strong coupling of molecular emissions to the metal probe over short distances (i.e., fluorescence quenching). Raman signals were strongly enhanced (>2−5×) over tip−surface distances <20 nm. X-ray diffraction and UV−vis absorption data were also acquired to help further elucidate changes in H_2Pc packing and electronic structure during the transition from submonolayer coverage to continuous films. Overall, this work provides emission based measurements of bimolecular exciton coupling in solid-state H_2Pc films, before the onset of complete fluorescence quenching, which has only been previously observed for select phthalocyanine species in solution.

A. Introduction

Phthalocyanines (Pcs), already widely used as commercial dyes and in optical recording media [1], are of interest to the research community for a myriad of applications [2-3], including organic electronics such as photovoltaics, LEDs, and transistors [4-7]; redox catalysis [8]; and as photosensitizers in optical-based cancer treatments [9]. Their popularity is due in large part to their tunability, i.e., the Pc macrocycle can be functionalized with a variety of chemical moieties (e.g., halogens, -CN, $-SO_3$-, -COOH, $-NH_2$, esters) and metal cation centers that modify their chemical, optical and electrical behavior. Pcs are also chemically and thermally stable [10], making them amenable to a wide range of processing techniques and potentially imparting long operational lifetimes to 'organic-based' devices [11-12].

The majority of work on solid-phase Pcs has focused on the structure and optical behavior of 50 nm to several micron thick films, especially for H_2Pc [13-15]. Scanning tunneling microscopy has also been used to study molecular packing of H_2Pc at sub-monolayer and monolayer coverages on a variety of surfaces [16-18]. Precise deposition of monolayer to few-layer phthalocyanine films has been achieved on a variety of substrates using Langmuir-Blodgett deposition [19-21]. The films produced are highly ordered with significant intermolecular π-electron overlap, leading to relatively high conductivities and photovoltaic currents. In this work, we combine tip-enhanced near-field microscopy (TENOM) with a variety of traditional characterization techniques (AFM, XRD, UV-Vis, confocal microscopy) to monitor the optical and structural behavior of H_2Pc molecules over the complete film thickness range, spanning sub-monolayer surface coverages to continuous films with crystalline domains. TENOM provides both optical and physical measurements on individual H_2Pc nanostructures, as well as spatially-correlated 2D images of topography, fluorescence, and Raman scattering.

B. Experimental Methods

(i) Tip-enhanced near-field optical microscopy (TENOM)

A custom-built tip-enhanced near-field optical microscope, previously described in detail [22], was used for simultaneous spectroscopic interrogation and imaging of fluorescence, Raman scattering, and topography of H_2Pc thin films and nanoscale patterns. The instrument combines an inverted optical microscope (Nikon Epiphot 300) coupled with a tuning fork-based, shear-force atomic force microscope (AFM). The 647 nm line of a Kr^+ laser is coupled to the microscope via single mode fiber, expanded to a plane wave, radially polarized, and focused using a 1.25 NA, 100X oil immersion objective lens onto the sample. The same objective collects emitted/scattered light and transmits it via a 50 μm core fiber (acting as a confocal pinhole) to a 320 mm focal length monochromator (JY iHR320) with TE-cooled CCD detector. The shear-force AFM consists of a quartz tuning fork ($f_0 \sim 2^{15}$ Hz), with electrochemically-etched Au-wire probe (apex diameter ~20-50 nm) attached to a z-piezo tube scanner. The probe is engaged on the surface with phase feedback using a 1° set point offset from the fork's free space resonance.

(ii) Deposition of nanoscale H_2Pc films

H_2Pc (Sigma-Aldrich) was thermally evaporated onto glass coverslip substrates; thickness was monitored using a quartz crystal microbalance (QCM) that was calibrated by scanning several H_2Pc step edges with a profilometer. Patterned H_2Pc films were produced using a colloidal lithography process described elsewhere [23]; briefly, silica colloids (dia. = 310 or 1000 nm, Bangs Laboratories) were functionalized with allyltrimethoxysiloxane, dip-coated onto glass coverslips using the Langmuir-Blodgett method, and subsequently used as a shadow mask for H_2Pc evaporation, followed by removal of the colloidal mask via sonication in water. Nanorod-like surface structures were also formed on some samples by annealing α-phase H_2Pc films (1-5 ML coverage) at 150-300 °C for 2 hrs. under high vacuum ($P < 5*10^{-5}$ Torr).

(iii) Additional characterization

UV-Vis absorption spectra of thin and patterned H_2Pc films and solutions were collected using a Jasco V-630 spectrophotometer; absorbance values were calculated after subtraction of a reference spectrum (a bare glass coverslip for thin film samples and pure tetrahydrofuran (THF) solvent for H_2Pc solutions). Solution fluorescence data for H_2Pc in THF were obtained using a Varian Cary Eclipse spectrophotometer. XRD data (Appendix A3.1) were collected using a PANalytical Empyrean diffractometer over Bragg angles of 5-20°. High resolution AFM topography images were collected with a Veeco Nanoscope IIIa (**Figs. 3.1 and 3.5**) and Asylum MFP-3D AFM (**Fig. 3.5**). To maximize the achievable lateral resolution in **Figure 3.1**, a cantilever with an apex diameter <5 nm was used (NanoSensors SuperSharpSilicon probe series).

C. Results and Discussion

(i) Visualizing the structure of thin H_2Pc films

AFM topography scans were collected for H_2Pc films of varying thickness deposited on clean glass coverslips [**Figs. 3.1(a-f)**]. The bare glass substrate was found to be relatively flat [**Fig. 3.1(a)**], with several small pits being the only notable surface features. As small amounts of H_2Pc were added, aggregates with a height of 1-2 nm appear uniformly distributed across the surface [**Figs. 3.1(b-c)**]. These aggregates are believed to form via coalescence of H_2Pc molecules on the surface, driven by the self-interaction potential of H_2Pc exceeding that of H_2Pc-SiO_2. This explanation is supported by previous STM studies that have shown significant thermal motion of surface phthalocyanine species at ambient temperatures on glass and HOPG substrates [18]. When ~1 monolayer of H_2Pc was deposited [**Fig. 3.1(d)**], aggregates began to coalesce and form a continuous layer. Additional H_2Pc deposition resulted in a more film-like deposit, composed of increasingly larger crystallites [**Fig. 3.1(e-f)**]. XRD data was obtained from these latter films, showing that the thicker films adopt a highly ordered, α-phase crystal structure[13] (see Appendix A3.1).

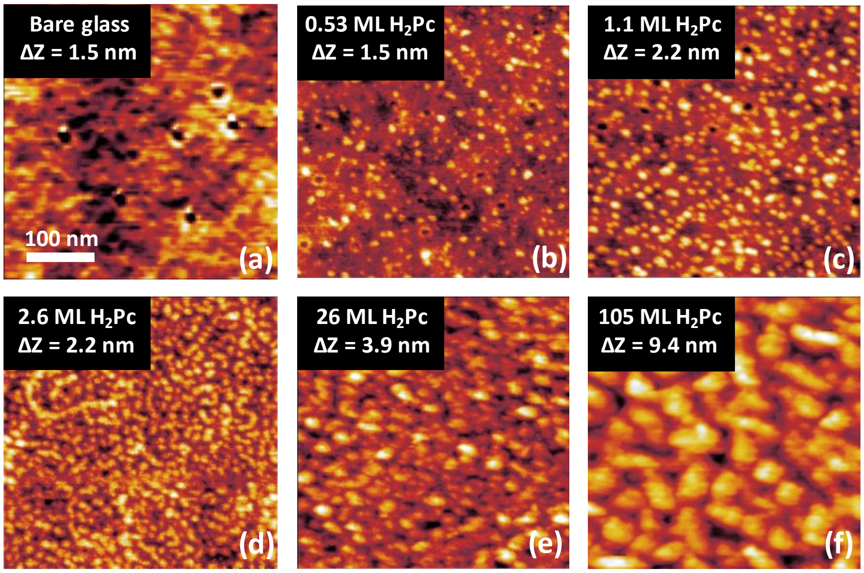

Figure 3.1 AFM topography data for various amounts of H_2Pc thermally evaporated onto glass coverslip substrates. The frequency shift of the evaporator quartz crystal microbalance was used to estimate the amount of H_2Pc deposited in each case. A calibration between film thickness and frequency shift was obtained by measuring the height of several films deposited and gave a value of roughly 10 Hz/nm. Estimates of the # of equivalent monolayers (ML) were then made using the α-phase H_2Pc crystal density and lateral area of an H_2Pc molecule lying flat on the surface. The result was 0.26 ML deposited per 1 Hz QCM shift. The lateral dimensions of each image are 400x400 nm.

(ii) Far-field optical absorption and emission data

Comprehensive studies of the optical properties of H_2Pc solutions and films have been carried out previously [13, 24-28]. In the visible portion of the spectrum, a pair of electronic excitations, referred to as the Q-band, are responsible for absorption and emission in the molecule. **Figure 3.2(a)** shows absorption measurements for both a dilute solution of H_2Pc in THF and a 40 nm thick H_2Pc film. The solution spectrum has two distinct absorption peaks at 1.80 eV (689 nm) and 1.90 eV (653 nm), which correspond to the $\pi \rightarrow \pi^*$ Q_x and Q_y transitions [2]. The absorption profile changes significantly for the 40 nm film, with the Q-band now broadened, spanning the entire 500-800 nm range. This broadening is due to Davydov splitting between interacting H_2Pc molecules that make up the α-phase crystal structure and is an expected behavior for condensed phases of many optically-active organic molecules. Such broadening occurs even in the case of two-dimensional packing, as seen in the absorption spectrum of a single CuPc monolayer on an Al surface formed using Langmuir-Blodgett deposition [21]. Absorption data could not be resolved for samples with thicknesses less than 40 nm due to the signal-to-noise limit of the spectrophotometer.

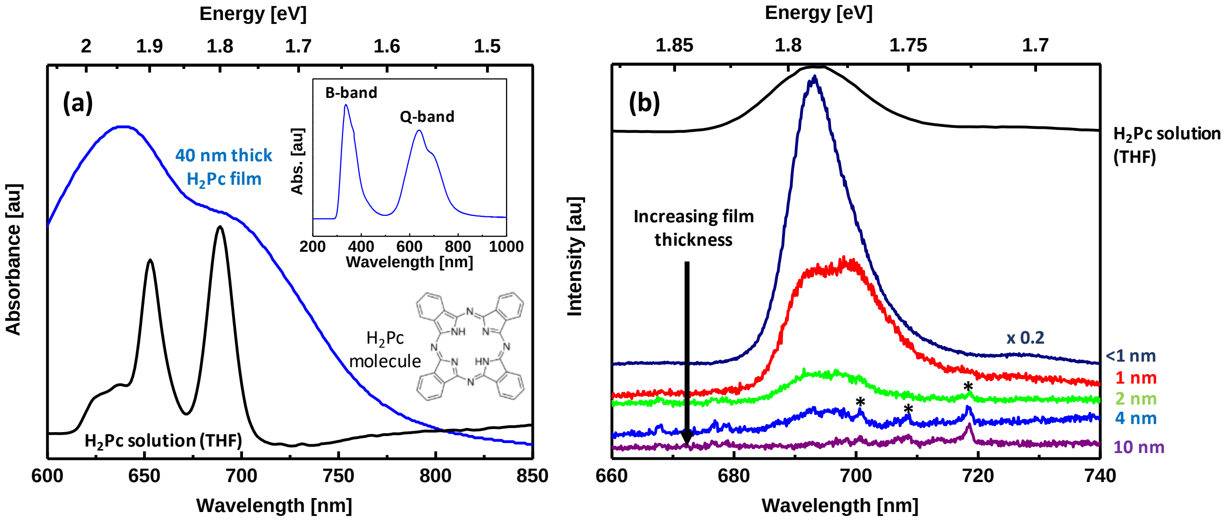

Figure 3.2 (a) Optical absorption spectra for a dilute solution of H_2Pc in THF and a 40 nm thick H_2Pc film. The full UV-Vis spectrum of the film is also included (inset) to show the broadening of both the Q- and B-bands. (b) Comparison of the optical emission from the same H_2Pc in THF solution and H_2Pc films of varying thickness. Fluorescence from the samples disappears rapidly as the film thickness increases, and Raman peaks (*) become visible for the 2, 4, and 10 nm thick films. The spectra are offset for clarity, but the intensity values have not been re-scaled except for the THF solution sample which measured on a separate UV-Vis instrument.

For very thin H_2Pc films (<10 nm), optical emission measurements were found to be a sensitive probe of the local film structure. Emission data from several H_2Pc samples, primarily collected using the confocal microscope component of the TENOM system, are shown in **Figure 3.2(b)**. For the dilute solution of H_2Pc in THF, a single fluorescence band is seen, corresponding to emission from the 1.80 eV lower energy excited state, in accordance with Kasha's rule [29]. As fluorescence disappears in the thicker films, weak Raman vibrational peaks become discernible between 660-720 nm. These peaks agree well with past results measured for H_2Pc films [13, 30] (Appendix A3.2). This indicates that H_2Pc molecules were not modified, nor decomposed, during thermal evaporation.

It is clear from the emission data that the film thickness and fluorescence intensity are inversely related in some manner. Fluorescence and photoluminescence quenching are known to occur in films due to an increase in the availability of efficient, non-radiative relaxation pathways caused by charge exchange between nearby molecules (Dexter and Förster mechanisms) [31]. Fluorescence quantum yields from H_2Pc films were previously reported to be on the order of 0.01% [25], and only a small number of Pc dimers with appreciable fluorescence yields have been reported [32-33]. These quenching effects imply that the intense fluorescence observed in very thin films originates from "isolated" H_2Pc molecules. For the < 1 nm thick sample in **Figure 3.2(b)**, coverage is estimated at ~ 0.25 monolayer for a 1 Hz QCM shift using the density of α-phase H_2Pc (1.7 molecules/nm^3), QCM calibration constant of the evaporator (10 Hz/nm), and the area of a single H_2Pc molecule lying flat on a surface being 1.55 nm^2. This coverage level is consistent with the theory that single, isolated H_2Pc molecules present on the glass surface are responsible for the strong fluorescence emission observed.

In addition to decreased intensity, another effect of direct coupling between H_2Pc molecules is that fluorescence energies are modified. The theory of molecular exciton coupling, first proposed by Kasha in 1965 [34], has been successful at explaining the optical properties of phthalocyanines as dimers or repeating structures such as crystals [35-38]. The theory considers the orientation, magnitude, and separation distance of the transition dipole moments between molecules. For H_2Pc, the Q_x and Q_y excitations have transition dipole moments that lie in the plane of the molecule [39]. The theory predicts that the Q-band of cofacially arranged Pc dimers will blue-shift, and that of edge-to-edge dimers should red-shift [2]. Experiments have found these predictions to be reasonably accurate for dimer phthalocyanine species in solution, as characterized by their absorption spectra [27, 35, 40]. **In Figure 3.2(b)**, there may be a red-shift in the fluorescence of the higher coverage films (1-4 nm), but it is hard to tell from these data alone.

To better quantify any changes in the fluorescence intensity or distribution as a function of film thickness, large 2D datasets were collected by laterally raster-scanning samples and collecting confocal fluorescence data at each location. The scans covered a 10x10 μm^2 area with 1681 individual spectra being collected (41x41 pixels, 250 nm pixel size). Figure 3 presents results from three of these scans on samples ranging from roughly 0.1 to 1 monolayer coverage, which was the range over which the fluorescence characteristics changed most rapidly. Looking first at images of total fluorescence intensity [**Figs. 3.3(a-c)**], lower coverage samples display higher intensities, but also large lateral spatial variations. These variations are believed to be caused by regions of the inhomogeneous glass surface affecting to what extent H_2Pc molecules can aggregate. Areas with relatively little aggregation appear as high intensity bright spots in the fluorescence image.

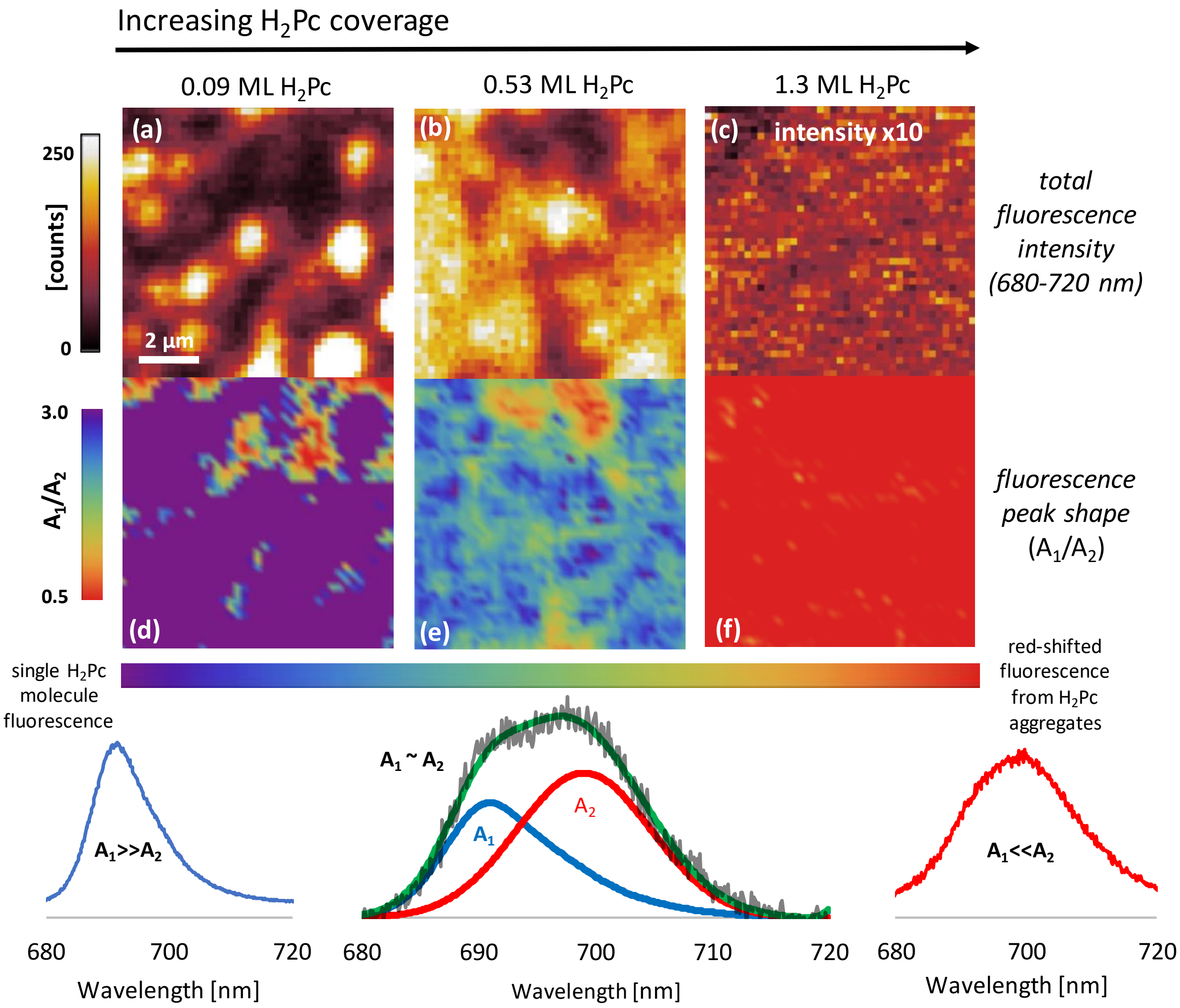

Figure 3.3 Confocal microscope images with data on the intensity and shape of H_2Pc fluorescence from samples of varying surface coverage. The top row of images (a-c) shows the total integrated fluorescence intensity over the 680-725 nm range. The bottom row (d-f) are the same datasets, now demonstrating that the fluorescence can be spatially deconvolved into single molecule vs. aggregate emission profiles (spectra below panels) using a peak area ratio metric (A_1/A_2), see Appendix A3.3 and A3.4 for details. In brief, the emission at each pixel was fit to a linear combination of H_2Pc single-molecule fluorescence (A_1) and a red-shifted Gaussian profile (A_2) that represents the average emission from H_2Pc dimers and small aggregates.

The lower set of panels [Figs. 3.3(d-f)] describe the shape of the fluorescence emission using a metric (A_1/A_2 ratio) that is explained below. The fluorescence signal at each pixel was fit to a linear combination of two distributions: A_1 represents emission from isolated

H_2Pc molecules (whose reference was collected from very low coverage samples), and A_2 represents the "average" of the red-shifted fluorescence observed in higher coverage samples (modeled with a simple Gaussian function). Exciton coupling theory provides a physical basis for assuming the film fluorescence spectra can be approximately fit in this manner. **Figure 3.3(d-f)** are plots of the ratio of the integrated peak areas of each fluorescence component. A more detailed explanation of the development and testing of the fit procedure is provided in Appendix A3.3 and A3.4. The main takeaway is that the emission evolves from single molecule-like fluorescence [**Fig. 3.3(d)**] to red-shifted fluorescence [**Fig. 3.3(f)**] over the range of 0.09 to 1.3 monolayer (ML) coverage. For example, the A_1/A_2 ratio for the brightest regions of the 0.09 ML sample is >100, and the mean value over the full image is 20. Conversely, the average ratio for the 1.3 ML sample falls to 0.3, a decrease of nearly two orders of magnitude. It is important to note that this ratio is based solely on fluorescence counts and does not correspond to the number of monomer vs. dimer+ species. Determining the fraction of monomer vs. dimers+ requires a quantitative value for the relative fluorescence intensity of isolated molecules compared to aggregated species.

(iii) Intentionally damaging H_2Pc films to produce fluorescence

The discussion thus far has shown that fluorescence is rapidly quenched as H_2Pc films exceed a coverage of roughly 1 monolayer. This observation can also be turned around to use fluorescence as an indicator of irregularities or damaged areas in thicker films. To demonstrate this idea, Fig. 4 shows a far-field optical image of a 10 nm thick H_2Pc film that was intentionally perturbed using a tungsten AFM probe. Hard surface contact was initiated by disabling the shear-force feedback, and then manually lowering the probe (20 nm) onto the H_2Pc film. The probe was dragged across the surface in a straight line and then retracted.

The fluorescence image shown was formed by raster scanning the damaged region through the focused laser spot [**Fig. 3.4(a)**], with the bright feature clearly following the line traced by the probe. Example spectra are shown from regions with and without fluorescence [**Fig. 3.4(b)**]. The exact structure of the damaged film region is not known, but a likely explanation is that the probe has scraped most of the H_2Pc away, leaving roughly a monolayer of molecules on the glass substrate. This is supported by the observation that the shape and intensity of the fluorescence seen here is close to that of the 1.3 ML sample measured previously [**Figs. 3.3(c) and (f)**].

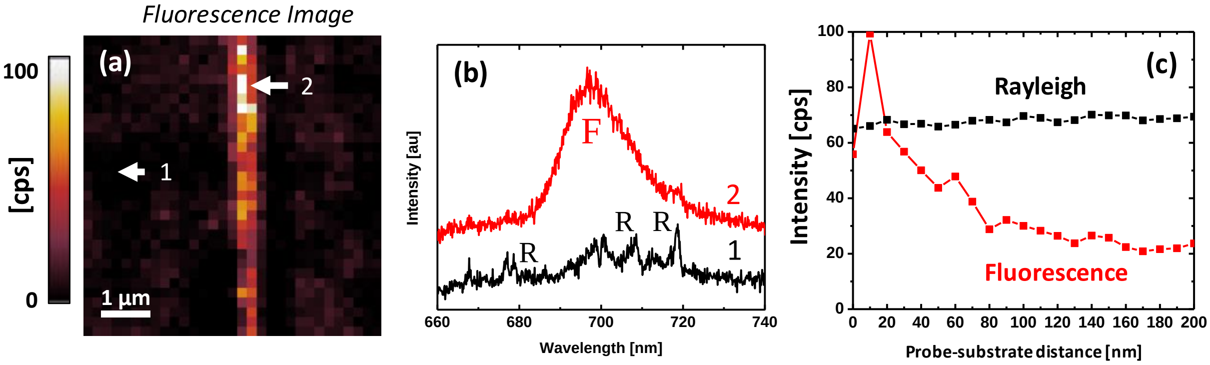

Figure 3.4 Fluorescence from areas of an H_2Pc film intentionally damaged using AFM probes. (a) A scratch in the film was created by dragging a W probe across the film for several microns. Pixel intensities correspond to the integrated fluorescence over the 680-725 nm range. (b) Example point spectra from both an undamaged (1) and damaged (2) region of the film. Fluorescence (F) and Raman (R) peaks are annotated. (c) Fluorescence data from an Au probe being retracted from a damaged film region. The initial 10 nm retraction causes a significant signal increase, indicating some amount of fluorescence quenching occurs when the probe is in direct contact with the H_2Pc surface molecules.

Similar film damage experiments were conducted with an Au probe. In this case, the frequency shift set-point of the AFM was increased significantly to force hard surface contact between the probe and film at a single location. Afterwards, the probe was retracted in a series of 10 nm steps, with spectral data being acquired at each step. **Figure 3.4(c)** shows the dependence of the total fluorescence intensity as a function of the probe-substrate separation, with 0 nm corresponding to measurement at the initially large AFM force set-point. The most striking feature of this plot is the >50% signal increase after the first 10 nm step. This appears to be a clear case of fluorescence quenching, in which the H_2Pc excited state decays non-radiatively via energy transfer to the metal probe. Quenching is most severe when fluorophores are directly adsorbed onto metal particles or surfaces, as seen when Au nanoparticles are functionalized with a metal-free phthalocyanine species [41], but energy transfer can occur over distances of several nanometers [42]. We have previously calculated an upper limit on the probe-surface distance of the near-field instrument's shear-force AFM to be 3 nm [22], making quenching feasible anytime the probe is engaged on the surface. It is also noteworthy that, even with quenching, the presence of the probe leads to a net increase in fluorescence compared to distances >100 nm. This increase was observed for all the Au probes used, indicating that the quantitative effect of local field enhancements tends to exceed any quenching effects in a scanning probe geometry, in good agreement with the data collected by Anger, Bharadwaj, and Novotny for coupling between nile blue molecules and a Au-nanoparticle functionalized AFM probe [43]. This net enhancement is leveraged in subsequent experiments to produce sub-diffraction limited images of H_2Pc surface structures using near-field fluorescence scattering.

(iv) Near-field optical microscopy of patterned H_2Pc films

Using the high spatial resolution of TENOM, it should be possible to measure connections between film thickness, morphology, and optical properties for individual H_2Pc nanostructures. A monolayer of silica colloids was used to produce patterned H_2Pc films with triangular surface features [see details in Methods section]. The masking colloids were spheres that only made direct contact with the glass substrate over a small area. It was thus expected that some undercutting of the mask edges would occur during thermal evaporation, i.e., a small amount of H_2Pc should be deposited on the glass substrate directly below the edges of the masking spheres. The goal was to measure changes in the H_2Pc properties moving across this undercut region.

Figure 3.5 presents topography and spectral images obtained from a 10 nm thick, patterned H_2Pc film, made using 1 µm dia. colloid mask. The larger area topography data [**Fig. 3.5(a)**] was collected on a separate AFM and shows how variations in the colloid packing quality lead to connected or separated interstitial H_2Pc features. TENOM fluorescence images [**Figs. 3.5(b-c)**] were formed by integrating the spectra from 680-725 nm at each collection location. Regions with good mask packing show ordered triangular features with uniform fluorescence intensity [**Fig. 3.5(b)**]. In regions where the packing was poor [**Fig. 3.5(c)**], the larger surface features formed show a dark central region with bright fluorescence boundary that should correspond to the part of the surface that experienced a greatly reduced H_2Pc flux due to mask undercutting.

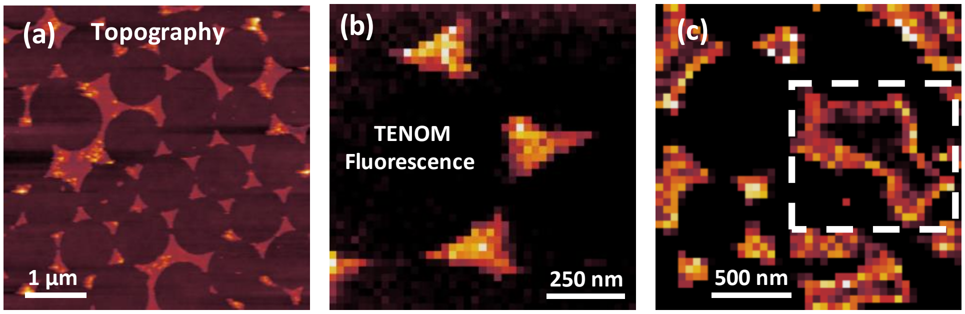

Figure 3.5 Physical and optical characterization of a 10 nm thick, patterned H_2Pc film on glass formed using a layer of 1 µm dia. close-packed silica particles as an evaporation mask. (a) Topography collected on a separate commercial AFM and (b-c) near-field fluorescence images collected with the TENOM instrument. The outlined feature in panel (c) shows an H_2Pc surface feature with a dark center region and bright fluorescent boundary. This strongly suggests that the particle mask creates spatial regions with widely varying H_2Pc coverage amounts that should produce fluorescence emission shifts similar to those characterized in Figure 3 for non-patterned H_2Pc samples.

To better resolve the undercutting region, a new sample was made using a 2 µm dia. colloidal mask, still with 10 nm of H_2Pc deposited through it. TENOM measurements on this sample yielded spatially correlated and simultaneously collected topography, Raman, and fluorescence data [Fig. 3.6]. Starting with the topography image, a transition region between the continuous H_2Pc film and the bare glass substrate can be seen, having a width of 100-200 nm. The green lines overlaid on the images show the two edges of this transition region based solely on the topography data. The left overlay line lines up very well with the maximum observed in the fluorescence signal. The Raman image shows the strongest signals on the lower-right section of the continuous film where the thickness is greatest and the number of H_2Pc molecules within the tip-enhanced volume is maximized.

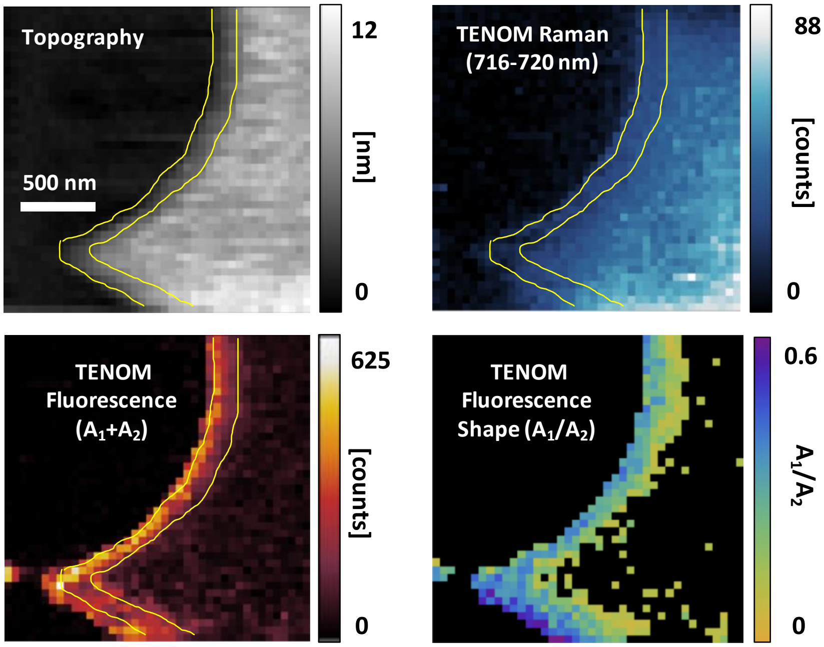

Figure 3.6 TENOM images showing correlated topography, fluorescence, and Raman data from a patterned 10 nm H_2Pc film made using 2 μm mask particles. The fluorescence is deconvolved (see Appendix A3.5 for details) into contributions from single H_2Pc molecules (A_1) vs. dimers and small aggregates (A_2). The edges of the H_2Pc surface feature display strong fluorescence while the interior region has much weaker emission. This difference is attributed to a rapid change in surface coverage at the boundaries created by undercutting of the mask particles during evaporation.

Due to some overlap between the fluorescence and Raman signals in these spectra, the procedure for fitting the fluorescence shape needed to be modified slightly. This involved restricting the data used in the fit to select wavelength bands without appreciable Raman peaks (see Appendix A3.5 for details). The fit of the fluorescence distribution shows a mix of emission from isolated molecules and small aggregates. Specifically, the A_1/A_2 ratio is 0.2-0.5 over the transition region, which corresponds most closely to values seen in the 1.3 ML studied earlier [Figs. 3.3(c) and 3.3(f)].

(v) Formation of H_2Pc nanocrystals via annealing

Previous literature studies have shown that thermal annealing of α-phase H_2Pc leads to the formation of the thermodynamically favored β-phase, which has a herringbone structure with increased tilt angle [2]. β-phase phthalocyanine structures can also be formed directly via evaporation onto a heated substrate [13], and phthalocyanine nanowires have even been produced via sublimation using a tube furnace [44-45]. To investigate these some of these effects and the resulting optical behavior of H_2Pc nanostructures, we carried out topography and TENOM fluorescence and Raman measurements on α-phase films that were vacuum-annealed at 150-300°C.

Annealed samples were first characterized using AFM topography to check for changes in surface morphology. At temperatures below 200°C, no changes were observed, with the surface remaining isotropically covered with small particles, as shown previously in **Figure 3.1**. However, for temperatures in the 225-250°C range, larger, anisotropic nanocrystals became visible [**Fig. 3.7(a)**]. The density of these nanocrystals could be controlled by varying the initial surface coverage. Crystals were seen to adopt a rod-like geometry, with heights of ~10 nm and lengths up to several hundred nanometers. These structures are believed to consist of β-phase H_2Pc, as the morphology is similar to needles previously observed in annealed, continuous films of that structure [13, 46].

Nanocrystal samples were then transferred to the TENOM instrument for additional optical and structural characterization. First, a large area optical scan was performed by measuring far-field confocal spectra at 100 points (1 μm pitch) over a 10x10 μm^2 grid. A reasonably uniform 'background' fluorescence signal with < 50% intensity variation was seen across all points, giving spectra similar to that shown in **Figure 3.7(b)**. We attribute this background, red-shifted fluorescence to a monolayer of H_2Pc molecules that remain fixed to the glass substrate during annealing; no emission from isolated H_2Pc molecules was detected. Additionally, when the annealing temperature was increased to 300°C, the uniform fluorescence remained, despite the complete disappearance of any crystals on the surface, as evidenced by AFM topography. The latter implies that H_2Pc molecules not directly deposited on the glass substrate evaporated during annealing.

When the Au TENOM probe was engaged on the same nanocrystal sample, both the fluorescence and Raman scattering increased significantly [**Fig. 3.7(b)**]. The far-field spectrum, for comparison, was collected immediately after the near-field, with a 2 sec. pause between measurements to wait for the piezotube to fully retract the probe. The near-field integrated fluorescence was ~5X larger, and assuming a far-field/near-field area ratio of 100, the enhancement factor can be estimated at a moderate value of 500. A Raman enhancement factor was not attainable, as no Raman peaks could be resolved in the far-field spectrum. However, the appearance of multiple Raman bands in the near-field data implies that the relative enhancement of Raman scattering exceeds that of the fluorescence. This makes sense in light of the earlier discussion of fluorescence quenching induced by the Au probe [**Fig. 3.4(c)**]. As Raman scattering is not susceptible to quenching, enhancement is expected to increase monotonically with the local field strength, as seen experimentally.

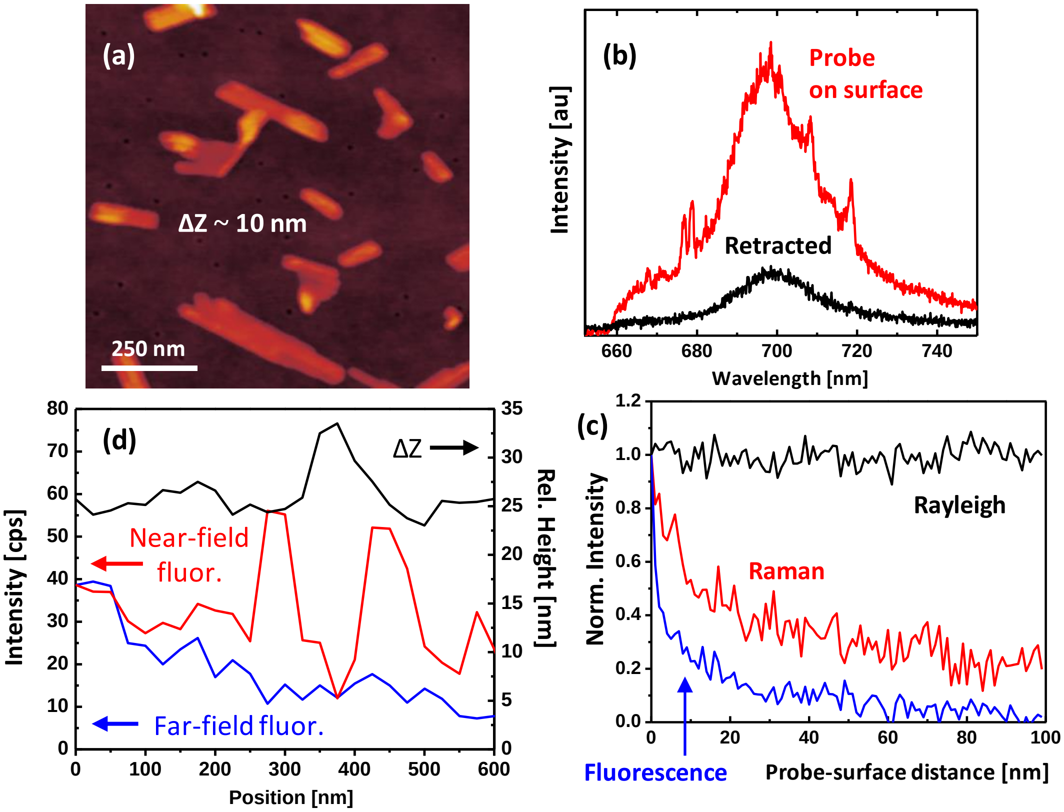

Figure 3.7 Physical and optical characterization of an annealed H_2Pc sample (5 ML initial film thickness, 225°C for 2 h). (a) High resolution topography image showing a distribution of rod-like nanocrystals on the glass surface. (b) Near-field (probe on surface) and far-field (retracted) optical spectra of the same sample. (c) Probe-surface distance dependence of normalized Rayleigh, Raman, and fluorescence scattering signals. The rapid decrease of the Raman and fluorescence signals within the first 20 nm, while the Rayleigh laser line remains constant, is consistent with near-field enhancement. The very rapid fluorescence decrease is believed to be caused by photobleaching induced by the more intense optical fields at the probe apex. (d) Near-field fluorescence and topography data were simultaneously collected while scanning over a single nanocrystal. The probe was then retracted and the confocal microscope (far-field) scan over the same area was unable to resolve any sign of the nanocrystal.

Raman and fluorescence signals were recorded during probe retraction from the surface to evaluate the distance scaling of enhancement phenomena. As the probe was lifted away from the surface, a rapid decrease in both the Raman and fluorescence signals occurred within the first 20 nm, while the Rayleigh (back-reflection) signal remained constant [Fig. 3.7(c)].

Moreover, the fluorescence signal decreased by 60% within the first 2 nm of separation. This is believed to be the result of photobleaching caused by intense local optical fields generated by the probe. Unlike the blunt Au probe used to damage the surface in **Figure 3.4(c)**, the probe had an apex radius of ~20 nm and was expected to generate more intense near-field interactions. The far-field photobleaching rate alone cannot explain such a rapid loss of fluorescence, with an equivalent exposure time of 2 s at equal excitation power producing a signal decrease <20% [see A3.6].

A series of linear spatial scans were also performed with the Au probe engaged on the nanocrystal covered surface. **Figure 3.7(d)** shows spatially-correlated near-field fluorescence and topography data extracted from one such scan; an H_2Pc nanocrystal feature ~8 nm tall and <100 nm wide can be seen in the topography trace. The fluorescence spikes with the probe positioned on either edge of the crystal and is minimized with the probe centered on the feature. The fact that the crystals themselves do no fluoresce is expected on the basis of intermolecular quenching, analogous to the complete disappearance of fluorescence in phthalocyanine nanoparticles [47]. The increased fluorescence at the crystal boundaries was unexpected. It is possible that during the annealing process, the re-organization of H_2Pc molecules on the surface leads to regions of increased coverage around the nanocrystals. It is also possible that the probe, being oscillated laterally to the sample surface, is scraping the edges of the crystal and generating local fluorescence through that interaction, in similar fashion to **Figure 3.4(a)**. Immediately after collection of the near-field data, the probe was retracted, and the same area was again scanned (far-field fluorescence). In this case, no significant variation in fluorescence intensity was discernible at the nanocrystal location.

D. Conclusions

The optical and physical properties of metal-free phthalocyanine (H_2Pc) nanofilms, ranging from sub-monolayer coverage to thicknesses exceeding 10 nm, have been characterized on glass substrates using confocal microscopy and TENOM. At surface coverages much less than one monolayer, most H_2Pc molecules are isolated from one another on the surface and emit intense fluorescence. For coverages of roughly 0.25-1.0 ML, an increasing fraction of molecules end up in an edge-to-edge dimer configuration, and exciton coupling between them leads to a red-shifted and less intense fluorescence. Finally, at coverages exceeding a monolayer, molecular aggregates and eventually α-phase crystals are formed wherein fluorescence is almost entirely quenched by efficient non-radiative decay pathways due to intermolecular energy transfer. Near-field measurements with a plasmonic Au probe showed that both enhancement of fluorescence and Raman, as well as quenching of fluorescence, can occur at probe-surface distance <50 nm. The enhancement factors responsible were estimated at ~500X compared to the far-field. Simultaneous collection of topography and near-field fluorescence / Raman spectra were acquired for nanopatterned H_2Pc films with a lateral spatial resolution of 25 nm to assess local variations in molecular packing and surface coverage. Overall, this work provides the first emission-based measurements of bimolecular exciton coupling in solid-state H_2Pc films before the onset of complete fluorescence quenching.

References

1. Chen, Q.; Gu, D.; Shu, J.; Tang, X.; Gan, F. Optical and Recording Properties of Copper Phthalocyanine Films. *Materials Science and Engineering: B* **1994**, *25*, 171-174.
2. McKeown, N. B., *Phthalocyanine Materials*; Cambridge University Press, 1998.
3. Claessens, C. G.; Hahn, U.; Torres, T. Phthalocyanines: From Outstanding Electronic Properties to Emerging Applications. *The Chemical Record* **2008**, *8*, 75-97.
4. Terao, Y.; Sasabe, H.; Adachi, C. Correlation of Hole Mobility, Exciton Diffusion Length, and Solar Cell Characteristics in Phthalocyanine/Fullerene Organic Solar Cells. *Applied Physics Letters* **2007**, *90*, 103515.
5. Ichikawa, M.; Kobayashi, K.; Koyama, T.; Taniguchi, Y. Intense and Efficient Ultraviolet Electroluminescence from Organic Light-Emitting Devices with Fluorinated Copper Phthalocyanine as Hole Injection Layer. *Thin Solid Films* **2007**, *515*, 3932-3935.
6. Yasuda, T.; Tsutsui, T. Organic Field-Effect Transistors Based on High Electron and Ambipolar Carrier Transport Properties of Copper–Phthalocyanine. *Chemical Physics Letters* **2005**, *402*, 395-398.
7. Miyake, Y., et al. High Carrier Mobility up to 1.4 Cm2·V-1·S-1in Non-Peripheral Octahexyl Phthalocyanine. *Applied Physics Express* **2011**, *4*, 021604.
8. Huang, Z.; Bao, H.; Yao, Y.; Lu, W.; Chen, W. Novel Green Activation Processes and Mechanism of Peroxymonosulfate Based on Supported Cobalt Phthalocyanine Catalyst. *Applied Catalysis B: Environmental* **2014**, *154-155*, 36-43.
9. Nishiyama, N., et al. Enhanced Photodynamic Cancer Treatment by Supramolecular Nanocarriers Charged with Dendrimer Phthalocyanine. *J Control Release* **2009**, *133*, 245-51.
10. Sadaoka, Y.; Sakai, Y.; Jones, T. A.; Göpel, W. Effects of Oxidizing Gases on Semiconductivity and Thermal Stability of Phthalocyanine Thin Films. *Journal of Materials Science* **1990**, *25*, 3024-3028.
11. Mori, T.; Mitsuoka, T.; Ishii, M.; Fujikawa, H.; Taga, Y. Improving the Thermal Stability of Organic Light-Emitting Diodes by Using a Modified Phthalocyanine Layer. *Applied Physics Letters* **2002**, *80*, 3895-3897.
12. Padma, N.; Joshi, A.; Singh, A.; Deshpande, S. K.; Aswal, D. K.; Gupta, S. K.; Yakhmi, J. V. No2 Sensors with Room Temperature Operation and Long Term Stability Using Copper Phthalocyanine Thin Films. *Sensors and Actuators B: Chemical* **2009**, *143*, 246-252.
13. M. Bayliss, S.; Heutz, S.; Rumbles, G.; S. Jones, T. Thin Film Properties and Surface Morphology of Metal Free Phthalocyanine Films Grown by Organic Molecular Beam Deposition. *Physical Chemistry Chemical Physics* **1999**, *1*, 3673-3676.
14. Hammond, R. B.; Roberts, K. J.; Docherty, R.; Edmondson, M.; Gairns, R. X-Form Metal-Free Phthalocyanine: Crystal Structure Determination Using a Combination of High-Resolution X-Ray Powder Diffraction and Molecular Modelling Techniques. *Journal of the Chemical Society, Perkin Transactions 2* **1996**, 1527-1528.
15. Mason, R.; Williams, G. A.; Fielding, P. E. Structural Chemistry of Phthalocyaninato-Cobalt(Ii) and -Manganese(Ii). *Journal of the Chemical Society, Dalton Transactions* **1979**, 676-683.
16. Nilson, K.; Ahlund, J.; Brena, B.; Gothelid, E.; Schiessling, J.; Martensson, N.; Puglia, C. Scanning Tunneling Microscopy Study of Metal-Free Phthalocyanine Monolayer Structures on Graphite. *J Chem Phys* **2007**, *127*, 114702.
17. Walzer, K.; Hietschold, M. Stm and Sts Investigation of Ultrathin Tin Phthalocyanine Layers Adsorbed on Hopg(0001) and Au(111). *Surface Science* **2001**, *471*, 1-10.
18. Wang, Y.; Wu, K.; Kröger, J.; Berndt, R. Review Article: Structures of Phthalocyanine Molecules on Surfaces Studied by Stm. *AIP Advances* **2012**, *2*, 041402.

19. Valli, L. Phthalocyanine-Based Langmuir–Blodgett Films as Chemical Sensors. *Advances in colloid and interface science* **2005**, *116*, 13-44.
20. Baker, S.; Petty, M.; Roberts, G.; Twigg, M. The Preparation and Properties of Stable Metal-Free Phthalocyanine Langmuir-Blodgett Films. *Thin Solid Films* **1983**, *99*, 53-59.
21. Yoneyama, M.; Sugi, M.; Saito, M.; Ikegami, K.; Kuroda, S.-i.; Iizima, S. Photoelectric Properties of Copper Phthalocyanine Langmuir-Blodgett Film. *Japanese journal of applied physics* **1986**, *25*, 961.
22. Hermann, R.; Gordon, M. J. Subdiffraction-Limited Chemical Imaging of Patterned Phthalocyanine Films Using Tip-Enhanced near-Field Optical Microscopy. *Journal of Raman Spectroscopy* **2016**, *47*, 1287-1292.
23. Haynes, C. L.; Van Duyne, R. P. Nanosphere Lithography: A Versatile Nanofabrication Tool for Studies of Size-Dependent Nanoparticle Optics. *The Journal of Physical Chemistry B* **2001**, *105*, 5599-5611.
24. Kobayashi, N.; Ogata, H.; Nonaka, N.; Luk'yanets, E. A. Effect of Peripheral Substitution on the Electronic Absorption and Fluorescence Spectra of Metal-Free and Zinc Phthalocyanines. *Chemistry* **2003**, *9*, 5123-34.
25. Sakakibara, Y.; Bera, R. N.; Mizutani, T.; Ishida, K.; Tokumoto, M.; Tani, T. Photoluminescence Properties of Magnesium, Chloroaluminum, Bromoaluminum, and Metal-Free Phthalocyanine Solid Films. *The Journal of Physical Chemistry B* **2001**, *105*, 1547-1553.
26. Unni, K. N.; Menon, C. Electrical and Optical Studies on Metal-Free Phthalocyanine Thin Films. *Journal of materials science letters* **2001**, *20*, 1207-1209.
27. Sharp, J. H.; Lardon, M. Spectroscopic Characterization of a New Polymorph of Metal-Free Phthalocyanine. *The Journal of Physical Chemistry* **1968**, *72*, 3230-3235.
28. Abdeldayem, H. A.; Frazier, D. O.; Penn, B. G.; Smith, D. D.; Banks, C. E. Non-Linear Optothermal Properties of Metal-Free Phthalocyanine. *Thin Solid Films* **1999**, *350*, 245-248.
29. Kasha, M. Characterization of Electronic Transitions in Complex Molecules. *Discussions of the Faraday society* **1950**, *9*, 14-19.
30. Tackley, D. R.; Dent, G.; Ewen Smith, W. Phthalocyanines: Structure and Vibrations. *Physical Chemistry Chemical Physics* **2001**, *3*, 1419-1426.
31. Lunt, R. R.; Giebink, N. C.; Belak, A. A.; Benziger, J. B.; Forrest, S. R. Exciton Diffusion Lengths of Organic Semiconductor Thin Films Measured by Spectrally Resolved Photoluminescence Quenching. *Journal of Applied Physics* **2009**, *105*, 053711.
32. FitzGerald, S.; Farren, C.; Stanley, C. F.; Beeby, A.; Bryce, M. R. Fluorescent Phthalocyanine Dimers—a Steady State and Flash Photolysis Study. *Photochemical & Photobiological Sciences* **2002**, *1*, 581-587.
33. Yoon, M.; Cheon, Y.; Kim, D. Absorption and Fluorescence Spectroscopic Studies on Dimerization of Chloroaluminum (Iii) Phthalocyanine Tetrasulfonate in Aqueous Alcoholic Solutions. *Photochemistry and photobiology* **1993**, *58*, 31-36.
34. Kasha, M.; Rawls, H.; Ashraf El-Bayoumi, M. The Exciton Model in Molecular Spectroscopy. *Pure and Applied Chemistry* **1965**, *11*, 371-392.
35. Dodsworth, E. S.; Lever, A.; Seymour, P.; Leznoff, C. Intramolecular Coupling in Metal-Free Binuclear Phthalocyanines. *The Journal of Physical Chemistry* **1985**, *89*, 5698-5705.
36. Fujiki, M.; Tabei, H.; Kurihara, T. Self-Assembling Features of Soluble Nickel Phthalocyanines. *The Journal of Physical Chemistry* **1988**, *92*, 1281-1285.
37. Schutte, W.; Sluyters-Rehbach, M.; Sluyters, J. Aggregation of an Octasubstituted Phthalocyanine in Dodecane Solution. *The Journal of Physical Chemistry* **1993**, *97*, 6069-6073.
38. Wright, J. D., *Molecular Crystals*, Second edition ed.; Cambridge University Press, 1995.

39. Toyota, K.; Hasegawa, J.-y.; Nakatsuji, H. Excited States of Free Base Phthalocyanine Studied by the Sac-Ci Method. *The Journal of Physical Chemistry A* **1997**, *101*, 446-451.
40. Ortí, E.; Brédas, J. L.; Clarisse, C. Electronic Structure of Phthalocyanines: Theoretical Investigation of the Optical Properties of Phthalocyanine Monomers, Dimers, and Crystals. *The Journal of Chemical Physics* **1990**, *92*, 1228-1235.
41. Kotiaho, A.; Lahtinen, R.; Efimov, A.; Metsberg, H.-K.; Sariola, E.; Lehtivuori, H.; Tkachenko, N. V.; Lemmetyinen, H. Photoinduced Charge and Energy Transfer in Phthalocyanine-Functionalized Gold Nanoparticles. *The Journal of Physical Chemistry C* **2009**, *114*, 162-168.
42. Lakowicz, J. R. Radiative Decay Engineering 5: Metal-Enhanced Fluorescence and Plasmon Emission. *Analytical biochemistry* **2005**, *337*, 171-194.
43. Anger, P.; Bharadwaj, P.; Novotny, L. Enhancement and Quenching of Single-Molecule Fluorescence. *Physical review letters* **2006**, *96*, 113002.
44. Tong, W.; Djurišić, A.; Ng, A.; Chan, W. Synthesis and Properties of Copper Phthalocyanine Nanowires. *Thin Solid Films* **2007**, *515*, 5270-5274.
45. Tong, W.; Djurišić, A.; Xie, M.; Ng, A.; Cheung, K.; Chan, W.; Leung, Y.; Lin, H.; Gwo, S. Metal Phthalocyanine Nanoribbons and Nanowires. *The Journal of Physical Chemistry B* **2006**, *110*, 17406-17413.
46. Karan, S.; Mallik, B. Effects of Annealing on the Morphology and Optical Property of Copper (Ii) Phthalocyanine Nanostructured Thin Films. *Solid State Communications* **2007**, *143*, 289-294.
47. Nitschke, C.; O'Flaherty, S. M.; Kröll, M.; Blau, W. J. Material Investigations and Optical Properties of Phthalocyanine Nanoparticles. *The Journal of Physical Chemistry B* **2004**, *108*, 1287-1295.

Appendix (A3)

A3.1 XRD measurements of H_2Pc film crystal structure

XRD measurements were performed on H_2Pc films of varying thickness to determine the packing arrangement adopted by the structures revealed in the AFM images. There are three known and fully characterized crystal structures of H_2Pc, termed the α, β, and X phases [1-2]. Thermal evaporation or organic molecular beam epitaxy of H_2Pc usually results in films in the α or β phases [3], which are both herringbone structures that differ in their molecular tilt angles (28° and 46°, respectively). Past literature results suggested that for the growth conditions used in this study, the α-phase should be formed. In Figure A3.1, the 20, 40, and 100 nm thick films display two diffraction peaks having d-spacings that agree with those previously reported for α-phase H_2Pc. Significant peak broadening in the 20 and 40 nm film data is believed to be a result of decreasing average crystallite size, in accordance with the Sherrer equation. For films ≤10 nm thick, there were no detectable diffraction peaks. We believe this is due to very small crystal domains that offer an insufficient number of diffracting planes to yield constructive interference. The AFM images of these samples show a smooth transition between individual nanocrystals on a glass surface and the formation of a continuous film (Fig. 3.1 main text). It cannot be determined from the available AFM and XRD data if the packing structure of these nanocrystals differs significantly from the α-H_2Pc formed in thicker films.

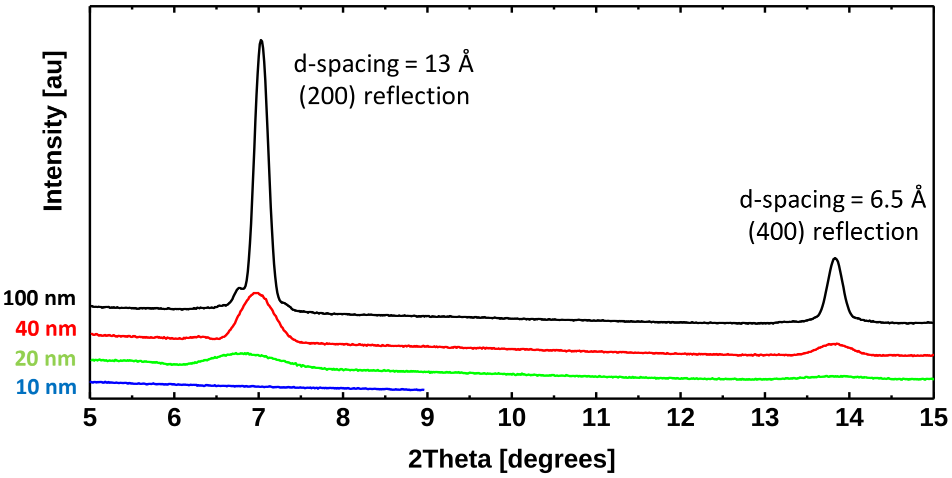

Figure A3.1 X-ray diffraction data from H_2Pc films of varying thickness grown on glass coverslips via thermal evaporation. The observed peaks at 7.1° and 13.9° are close to the reported literature values of 6.8° and 13.6° for α-phase H_2Pc [1]. The small 0.3° difference is likely due to small errors in the planarity of the sample holder or substrate. Peak broadening is observed for thinner films as the average crystallite size decreases.

A3.2 Far-field resonant Raman spectrum of metal-free phthalocyanine

The Raman spectrum shown below (Fig. A3.2) was collected from a 10 nm thick H_2Pc film using the confocal microscope mode of the TENOM instrument with 647 nm illumination. The spectrum agrees well with previous H_2Pc Raman spectra collected at excitation wavelengths of 633 and 623 nm [1, 4]. This measurement is taken as evidence that H_2Pc is not reacting or decomposing during the thermal evaporation process. The excitation energy should be accounted for when comparing H_2Pc Raman spectra, as the molecule has strong absorption in the red portion of the visible spectrum [Fig. 3.2(a) main text]. Hence, the peak intensity ratios obtained will be a strong function of excitation energy within the resonance Raman regime. At higher wavenumbers, the start of a broad photoluminescence band can also be seen. This emission was seen out to roughly 1 µm, at which point the CCD camera sensitivity drops off. This photoluminescence was only observed for films ≥2-4 nm thick.

Similar photoluminescence in α-phase H_2Pc films has been noted previously, with the effect being attributed to the radiative decay of excitons at defect sites in the films [1].

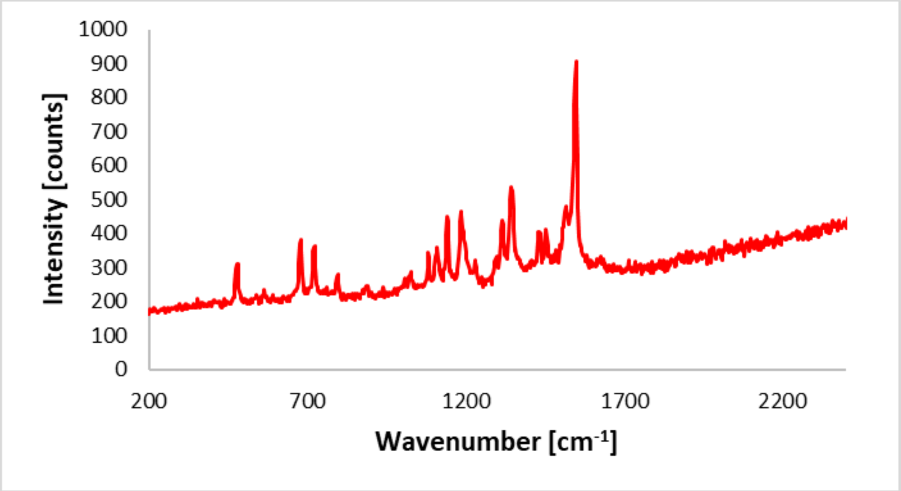

Figure A3.2 Far-field Raman spectrum of a 10 nm thick H_2Pc film thermally evaporated onto a glass coverslip. Collection time = 30 s, 647.1 nm excitation with ~1 mW at sample.

A3.3 Spectra fitting procedure for H_2Pc fluorescence

When examining far-field fluorescence spectra collected from H_2Pc nanofilms of varying thickness, it was immediately apparent that both the intensity and shape of the emission varied widely. The belief was that the observed differences were due to different H_2Pc structures distributed heterogeneously on the glass surface. These could include "isolated" H_2Pc molecules (those with no other H_2Pc molecules immediately adjacent), as well as small aggregates (dimers or several molecules). At the surface coverages measured here (0.1-0.4 ML), the lateral size of the laser spot (500 nm dia.) can be used to estimate that roughly 10^4 H_2Pc molecules are contributing to each spectrum. An effort was then made (details below) to decompose the observed fluorescence spectra into a linear combination of characteristic emission profiles from isolated H_2Pc molecules and red-shifted emission from H_2Pc aggregates.

(i) Isolated H_2Pc fluorescence spectrum

High intensity fluorescence emission was only observed in samples with very small amounts of H_2Pc (< 0.4 ML). Additionally, the shape of this emission was found to be identical across multiple samples and measurement locations. The combination of high intensity, low surface coverage, and a uniform emission profile all point to the source of this signal being isolated H_2Pc molecules. A single spectrum with very high signal intensity (to minimize detector noise) was selected to represent this emission, and a smooth interpolating function was fit to the data (Fig. A3.3). A baseline subtraction was also performed to adjust the interpolating function baseline to zero. This function is labelled "Isolated$H_2Pc[\lambda]$" in the fitting equation (Eq. A3.1) presented later in this appendix.

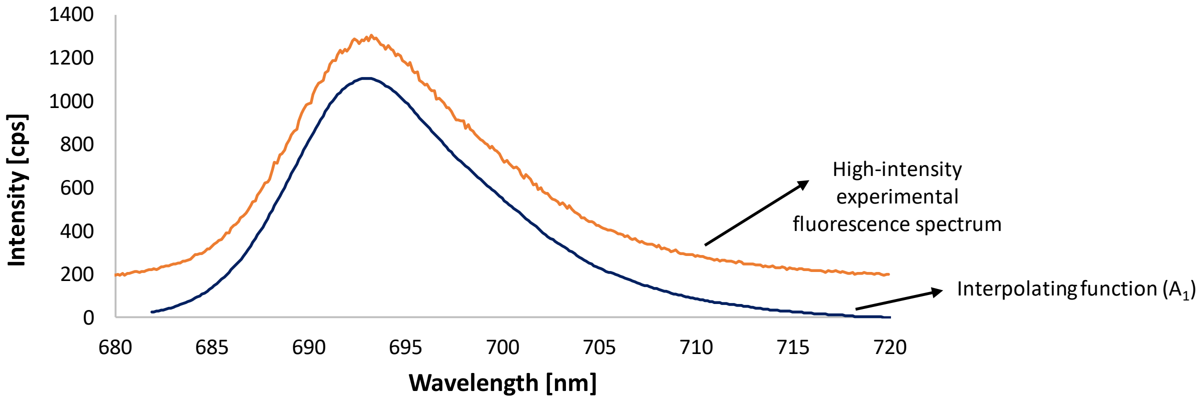

Figure A3.3 Experimental fluorescence spectrum of isolated H_2Pc molecules on a glass surface and the interpolating function "Isolated$H_2Pc[\lambda]$" used to represent this emission in Equation A3.1.

(ii) Red-shifted fluorescence from H_2Pc dimers and small aggregates

A common feature of the lower intensity fluorescence spectra was they were always red-shifted (peak λ = 696-702 nm) when compared to the isolated H_2Pc data (peak λ = 693 nm). This red-shift was attributed to intermolecular exciton coupling between adjacent H_2Pc molecules on the glass surface (see main text for details). The shape of the distribution also changed from that of isolated H_2Pc, becoming roughly symmetric about a peak wavelength. However, both the peak wavelength and width were found to vary between samples and locations. These variations were rationalized as a distribution of coupling geometries between H_2Pc molecules that are all present on the glass surface. The choice was made to represent this range of behavior using a single, characteristic profile. A Gaussian function with adjustable center wavelength (λ) and width (σ) was fit, using a sum-of-squares error minimization criterion, to a sample of 20 red-shifted fluorescence spectra picked at random from various samples (Fig. A3.4). Averaging the fit results yielded a characteristic Gaussian function with λ=699 nm and σ=6 nm. This single function was then used to fit the red-shifted fluorescence component in all the experimental data collected.

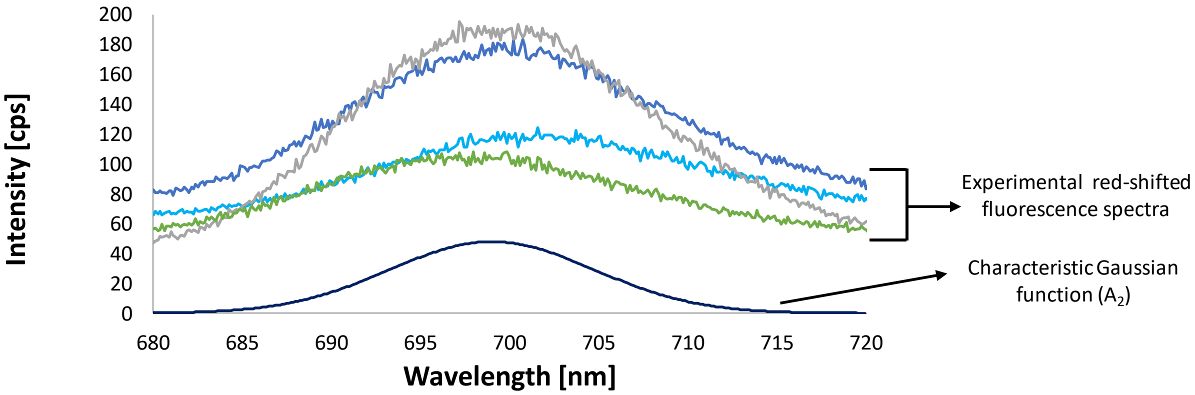

Figure A3.4 Four representative spectra showing red-shifted fluorescence from H_2Pc dimers and small aggregates. Both the peak intensity and peak width are observed to vary between spectra. This is attributed to a distribution of H_2Pc aggregates being present on the surface. These spectra are a subset of the 20 spectra averaged to produce the characteristic Gaussian function used for peak fitting.

After determining the two representative emission profiles, the fluorescence spectrum at each spatial location in three 2D datasets was fit to a linear combination of these functions scaled by the adjustable amplitudes A_1 and A_2. The fit was done using the built-in "NonlinearModelFit" algorithm in Mathematica. An example of the fit process is shown in Figure A3.5 for a fluorescence signal of intermediate intensity. Qualitatively, the fits were found to work well across all the datasets analyzed. Appendix A3.4 provides a quantitative evaluation of the fit quality.

$$Fit[\lambda] = A_1 * IsolatedH_2Pc[\lambda] + A_2 * Exp[-\frac{(\lambda-699)^2}{2\times(6)^2}] \qquad \textbf{(Equation A3.1)}$$

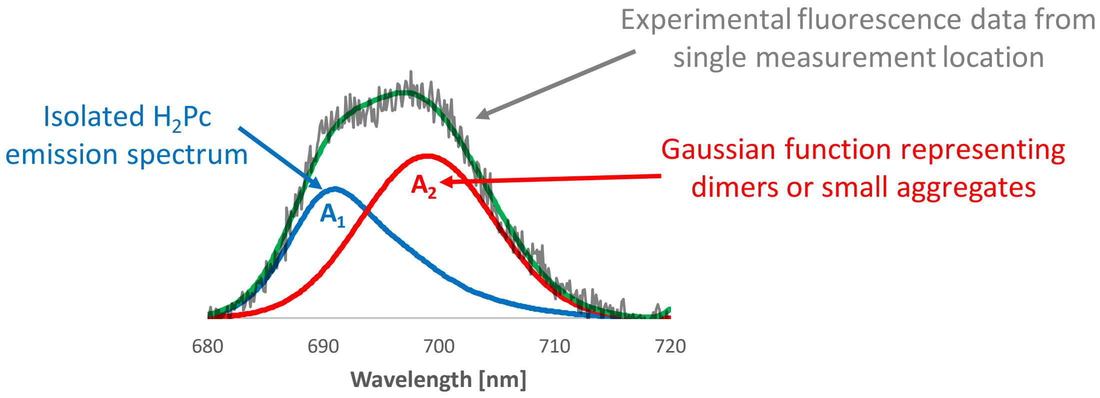

Figure A3.5 Example of the fitting procedure applied to a single fluorescence spectrum from a 0.53 ML coverage H_2Pc sample. The solid green line is the sum of the A_1 (blue) and A_2 (red) curves and can be seen to closely capture the shape of the experimental data (gray).

A final point on the fit procedure is that the reported values for A_1/A_2 in the main text (Figs. 3.3 and 3.6) are actually the ratio of areas, not amplitudes, for each fluorescence component. The area under each curve is proportional to the total fluorescent counts detected. For equal amplitudes, the area ratio of the isolated H_2Pc spectrum over the Gaussian function is 0.89. Adjustment by this factor is also why the text refers to the A_1/A_2 values as the "integral ratio".

A3.4 Assessing the quality of the spectra fitting procedure

The metric used by Mathematica for the spectra fitting was a sum-of-squares (SOS) error minimization. Plots of the SOS errors are reported on the subsequent page (Fig. A3.6) under the title “Absolute fit error”. When examining these plots, it is immediately apparent that there is a strong correlation between fluorescence intensity and error magnitude. This makes sense as even small deviations in the fit shape for high intensity spectra can produce local differences of hundreds of counts between the data and fit curve.

A more effective basis for comparison is thus to normalize each spectrum by its mean intensity value before computing the error. This metric compares the fits on an equal intensity basis and is shown in the “Normalized fit error” images. The normalized plots reveal that large relative fit error values are actually encountered in locations where the fluorescence intensity is low. This includes only certain parts of the 0.09 ML and 0.53 ML datasets but encompasses most of the 1.3 ML image. This trend is due to the fluorescence intensity at these locations approaching the noise level of the CCD detector. However, the fact that uniformly low relative errors are obtained for all the locations with medium to high fluorescence intensities is a strong indication that the fit procedure is effective at describing the spectra.

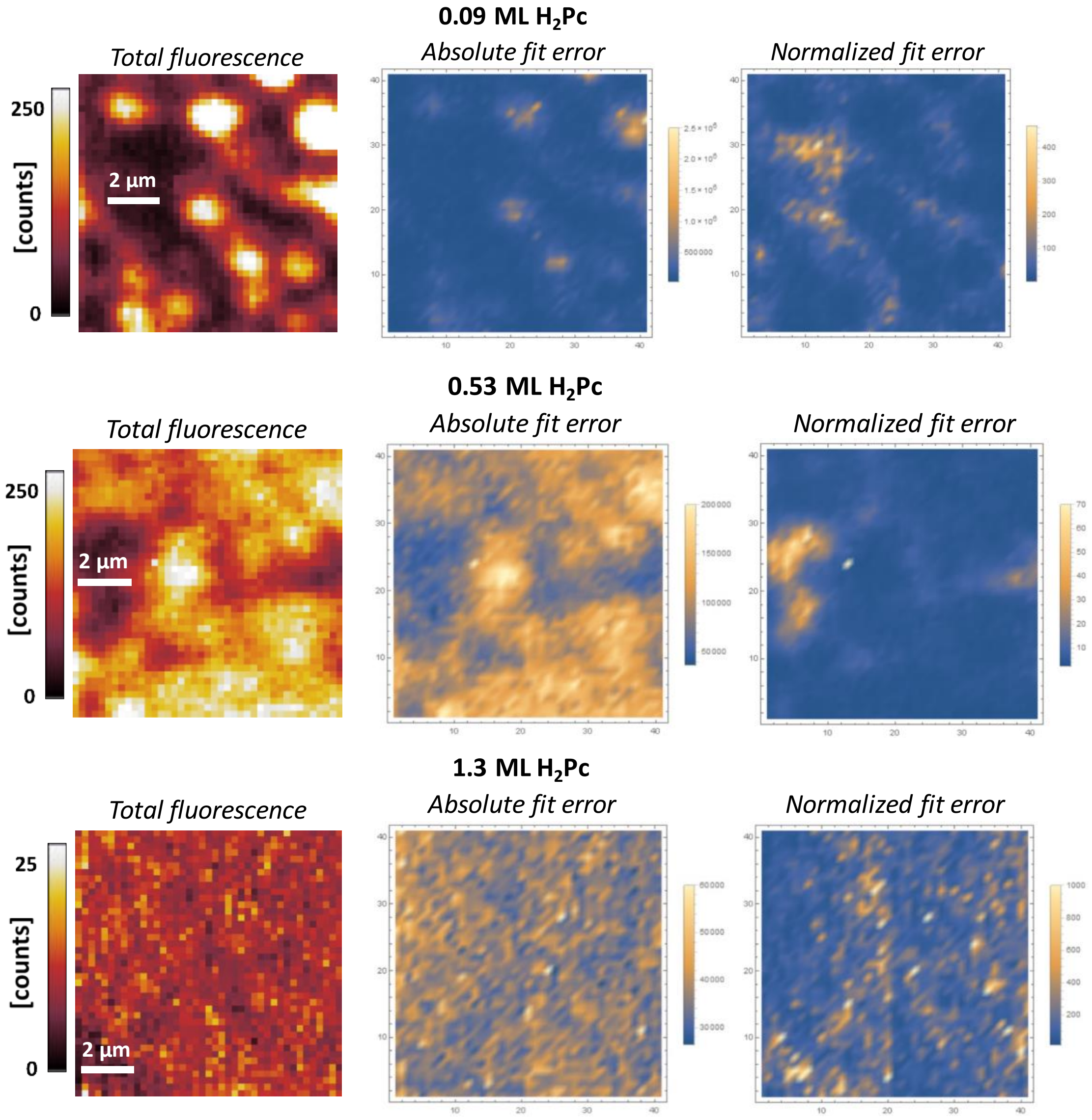

Figure A3.6 Assessing the quality of the fluorescence spectra fitting procedure for each of the three H_2Pc samples analyzed. The "Absolute fit error" images show the total sum-of-squares difference between the fit model and experimental data (calculated from 680-720 nm). The "Normalized fit error" images use the same sum-of-squares calculation, but first normalize each individual spectrum by its average signal intensity (average counts). The anomalous bright spot seen near the center of the normalized fit error image for the 0.53 ML sample is due to a cosmic ray artifact.

A3.5 Separating fluorescence and Raman signals in TENOM spectra

Figure 3.6 in the main text presents simultaneously collected TENOM fluorescence and TENOM Raman images from a patterned H_2Pc film. The energies of these two emission processes overlap, and correctly quantifying them required a means of separating their respective signals. This was accomplished by slightly modifying the A_1/A_2 fit procedure described above. Instead of fitting the fluorescence emission over the entire spectral region, the fit was restricted to consider only a pair of spectral regions that were relatively free of Raman peaks (Fig. A3.7). The integral of the A_1/A_2 fluorescence peaks found from this fit procedure was then used to create the near-field TENOM fluorescence image (Fig. 3.6 lower left panel). The near-field TENOM Raman image (Fig. 3.6 upper right panel) was subsequently formed by subtracting the A_1/A_2 fluorescence fit from the full spectrum and integrating the remaining signal over the range 716-720 nm. This integration range includes only the highest intensity Raman peak, which happens to also have the least overlap with the underlying fluorescence emission.

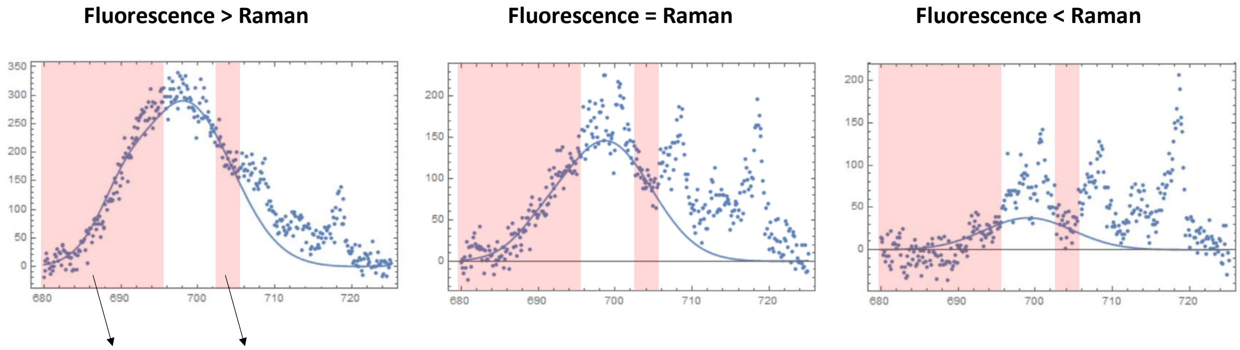

fit region #1
data points = 264
fit weight = 1

fit region #2
data points = 22
fit weight = 12

To give equal influence to each of the two highlighted regions, the relative fitting weight per data point in fit region #2 was increased by a factor of 12.

Figure A3.7 Examples of the modified fit procedure used when overlapping Raman and fluorescence optical signals were present. The two red shaded regions indicate the data points that were used to fit the fluorescence profile. These portions of the spectrum were chosen specifically to avoid contributions from Raman peaks. The three spectra show the modified fit procedure works well over a wide range of Raman-fluorescence intensity ratios.

A3.6 Photobleaching rate of H_2Pc fluorescence

For both as-deposited and annealed films of H_2Pc, photobleaching of the fluorescence emission as a function of the excitation laser power and exposure time was observed. A quantitative example of this effect is given below for a 5 ML annealed sample. The measurement was made with the confocal microscope portion of the TENOM instrument, with successive fluorescence spectra being collected over the same sample area. The laser power at the sample is roughly 100 μW and the collection time per pixel is 1 s.

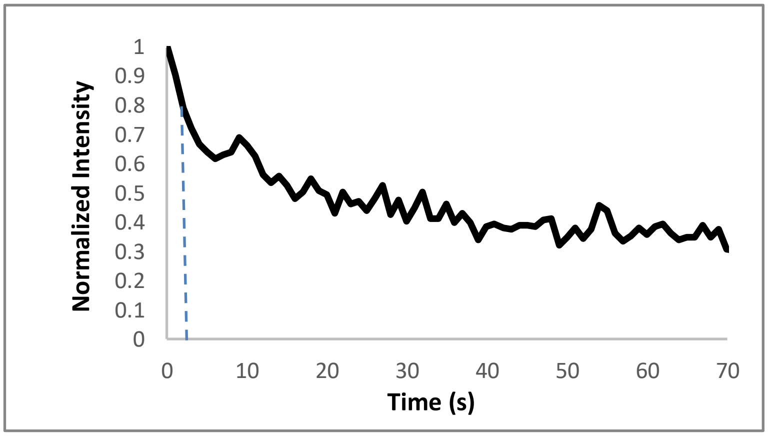

Figure A3.8 Photobleaching of fluorescence from an annealed H_2Pc sample. The intensity decays to 50% of the initial value by 30 s. The dashed line at 2 s indicates the equivalent exposure time for the 2 nm retraction point cited in the discussion of Figure 3.7(c) in the main text.

Appendix 3 References

1. M. Bayliss, S.; Heutz, S.; Rumbles, G.; S. Jones, T., Thin Film Properties and Surface Morphology of Metal Free Phthalocyanine Films Grown by Organic Molecular Beam Deposition. *Physical Chemistry Chemical Physics* **1999**, *1*, 3673-3676.
2. Hammond, R. B.; Roberts, K. J.; Docherty, R.; Edmondson, M.; Gairns, R., X-Form Metal-Free Phthalocyanine: Crystal Structure Determination Using a Combination of High-Resolution X-Ray Powder Diffraction and Molecular Modelling Techniques. *Journal of the Chemical Society, Perkin Transactions 2* **1996**, 1527-1528.
3. Mason, R.; Williams, G. A.; Fielding, P. E., Structural Chemistry of Phthalocyaninato-Cobalt(II) and Manganese(II). *Journal of the Chemical Society, Dalton Transactions* **1979**, 676-683.
4. Aroca, R.; Dilella, D. P.; Loutfy, R. O., Raman Spectra of Solid Films—I: Metal-Free Phthalocyanine. *Journal of Physics and Chemistry of Solids* **1982**, *43*, 707-711.

Chapter IV: Quantitative comparison of plasmon resonances and field enhancements of near-field optical antennae using FDTD simulations

Abstract

Plasmon resonances and electric field enhancements of different near-field optical antenna probes with engineered plasmonic nanostructures at their apexes were quantitatively compared using finite difference time domain (FDTD) optical simulations. Although many probe designs have been tested experimentally, systematic comparison of the field enhancement characteristics of different probes has not been addressed in the literature, due to differences in instrument configuration (STM vs. AFM vs. SNOM), optical system design and readout mechanism (probe excitation and light collection schemes, Raman vs. photoluminescence), and probe material and geometry. In the present study, we find that the refractive index and extinction coefficient of the probe support material, e.g., for the case of an AFM tip functionalized with a (plasmonic) nanoparticle, are critical in controlling the overall plasmonic behavior of the optical antenna. Support materials with strong absorption at optical energies (Pt, W) dampen plasmon resonances and lead to lower enhancements, while those with low absorption (SiO_2, Si_3N_4, Si) increase enhancements by modifying the extinction cross-section of the nanostructure. Using a set of physically realistic constraints, probe structures were optimized for peak plasmonic enhancement at common near-field optical wavelengths (633-647 nm). Probes with focused ion-beam milled grooves near the probe apex gave the largest local field enhancements (~30x). Moreover, when compared to an unstructured metal cone of similar size, grooved probes gave 300% improvement in field strength, which can boost tip-enhanced Raman spectroscopy signals by 1-2 orders of magnitude. Moreover, the resonance of these high-enhancement structures can be easily tuned to cover visible and near-infrared energies by varying the plasmonic metal (Ag or Au) and groove position relative to the apex. Overall, grooved probes may be very useful in near-field optical experiments where signal levels are particularly low, such as those encountered when analyzing non-metallic substrates where gap-mode plasmons cannot be leveraged.

A. Introduction

The production of plasmonic nano-antennae with reproducible large field enhancements has remained a persistent challenge in the fields of tip-enhanced near-field optical microscopy (TENOM) and tip-enhanced Raman spectroscopy (TERS). The most common methods of probe fabrication, namely metal-coating of AFM cantilevers [1] and electrochemical etching of metal wires [2], are known to produce structures with highly variable enhancements, largely caused by nano-structural differences [3-4]. One strategy that has partially mitigated issues with probe variability is the use of metallic or plasmonic substrates to operate instruments in a so-called "gap-mode" configuration [5-8], where intense (100x enhancement) and spatially localized fields are generated between the probe and substrate. Although gap-mode optical signal levels are high enough to meet the requirements of many near-field experiments, there are a wide range of dielectric, semiconductor, and organic surfaces of interest that cannot make use of this mechanism. For these substrates, maximizing probe enhancement is critical, especially for 2D near-field imaging where collection times per pixel must be small (<1 s).

In addition to increasing the magnitude of electromagnetic fields, there is also a desire to control the spatial distribution, polarization, and resonant energy of the near-field optical antenna probe. The polarization and near-field spatial distribution are known to strongly alter Raman scattering processes compared to far-field measurements [9-10]. Modeling and reproducibly controlling these effects is a prerequisite for quantitative analysis of near-field Raman spectra. Additionally, a few TERS experiments have demonstrated that extremely high spatial field confinements (<1 nm) are possible, allowing chemical images of individual molecules to be obtained [11-13]. Although the full mechanism of this confinement is still an active area of research, it is clear that tuning the local plasmon resonance of the probe to match the energy of molecular transitions is a necessary component in the process.

All the aforementioned applications would benefit from reproducible fabrication of near-field probes with precisely controlled nanostructures. Several means of accomplishing this have been proposed, including focused ion-beam milling (FIB) to create arbitrary 3D antenna shapes [14] or attachment of a plasmonic nanoparticle to the probe apex [15-16]. The common trait between these structures is that they possess localized surface plasmon (LSP) resonances that can be tuned as a function of material and geometric parameters. Direct comparison of the achievable enhancements from these designs has not been possible experimentally due to variability in the design wavelengths, instrument geometries, probe dimensions, and reporter molecules.

In the present work, finite difference time domain (FDTD) simulations were used to quantitatively assess of the performance of four different resonant probe designs that have been proposed and fabricated by groups in the near-field research community. The probe designs were then geometrically optimized to have localized surface plasmon (LSP) resonances in the 633-647 nm spectral range using a set of physically relevant constraints. The lessons learned from our analysis are intended to assist experimentalists in choosing physical parameters that maximize enhancements achievable for a given probe design.

B. Modeling methods

FDTD calculations were performed using Lumerical software. For the majority of simulations, a scalar Gaussian beam source, with 11-pt. multifrequency beam correction and 1 μm beam waist (1/*e* field points), was used in a 45° inverted illumination geometry. For the Au-coated Si cones in **Figure 4.2** and tests using optimized structures from **Figure 4.7** with varying substrate materials, a 45° side-on illumination source (i.e., above the glass substrate) was used instead, with all other source and simulation settings held constant. The advantage of a Gaussian beam source over a standard plane wave is that for optical excitation at non-normal angles, relative to the Cartesian simulation axes, the broadband frequency response can be accurately extracted from a single simulation. For probe-substrate simulations, a 1 nm gap was left between the lowest point of the probe apex and the substrate surface. Field values were recorded along a line at the center of the gap region (0.5 nm below the probe) that spanned the width of the entire probe apex. Plots that report E or E_{gap} values refer to the maximum field recorded along this line field monitor. This procedure was necessary to account for small changes in the maximum field position that occur when using angled optical sources. The same procedure with a 0.5 nm probe offset was used for simulations without a substrate [**Fig. 4.1**]. In all cases, the field values were normalized by those produced at the same spatial location under identical simulation settings, but with the probe structure entirely removed (labelled E_0). An advantage of reporting results in this manner is that the influence of source type and excitation geometry are minimized, allowing a more direct focus on the physics of the near-field probes being studied.

To minimize computation times while maintaining accuracy, adaptive meshing was utilized. A 1 nm mesh was applied over the first 100-200 nm of the probe apex, with a finer 0.25 nm mesh present only along the center of the probe-substrate gap. Perfectly matched layer boundary conditions were used in all simulations to minimize reflected light. Rigorous convergence testing was performed for all simulation parameters, including the size of custom mesh regions, minimum mesh sizes, and optical source settings. Parameters were deemed converged when subsequent refinements produced relative changes in local fields values of <5%. Experimental permittivity data for Au, Si, W, and Pt were taken from *The Handbook of Optical Constants of Solids* by E. Palik [17] and Si_3N_4 refractive index values from the work of Luke *et al.*[18]

C. A general model for the optical response of near-field probes

Extensive simulation work has been carried out using finite difference time domain (FDTD), finite element (FEM), and boundary element (BEM) methods to investigate the optical response of near-field probes as a function of their physical properties (apex radius, cone angle, probe/substrate materials) and illumination geometry [19-23]. A fundamental question when performing such work is how to accurately represent the probe, which in reality, is a spatially extended structure such as a metallized AFM tip or electrochemically etched metal wire, within a computationally feasible, microscopic simulation volume. Most studies use a metal cone to represent the general shape of a near-field probe, and investigate its optical behavior as a function of cone length, excitation source (beam or plane wave), and simulation boundary conditions [24-26]. A similar procedure was followed in the present work, with a generalized summary of the results presented in **Figure 4.1**.

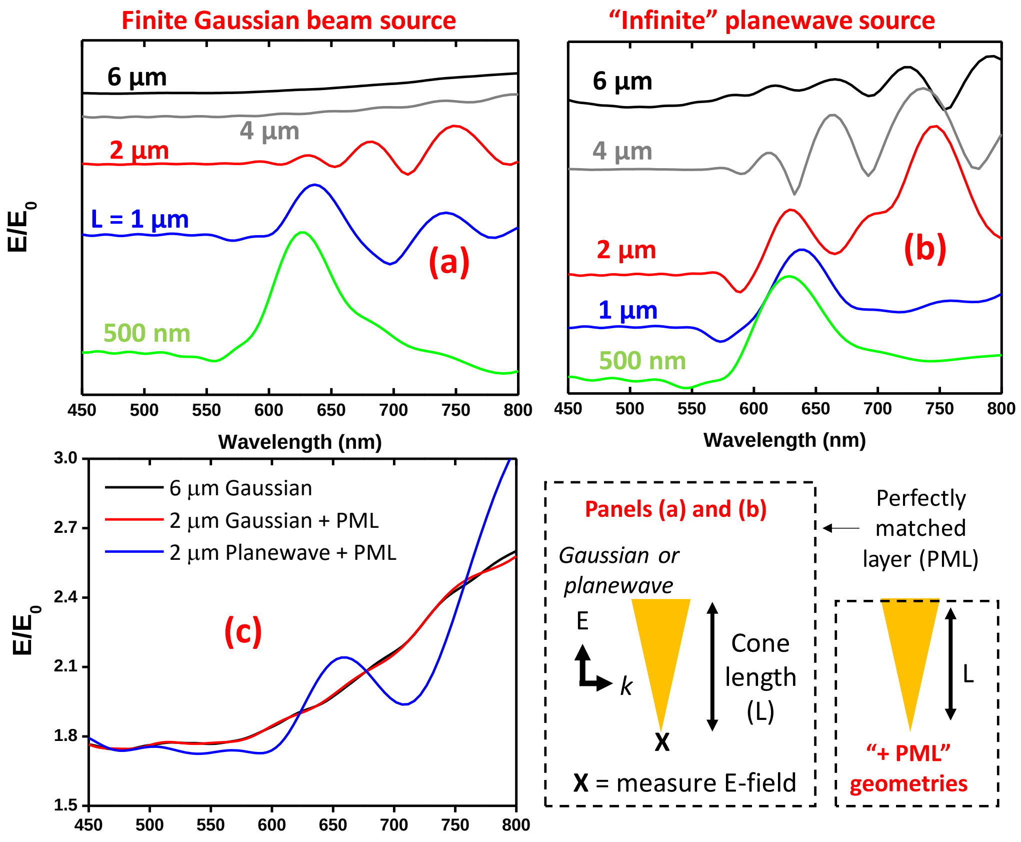

Figure 4.1 Example of how LSP modes of Au cones are very sensitive to cone length, optical excitation source, and simulation boundary conditions. (a) When using a focused beam source of finite width (1 µm), the apex fields converge to the infinite cone limit when the cone length >6 µm. (b) Field convergence is much slower when using a planewave source spanning the entire simulation cross-section, due to the launching of surface plasmon-polaritons (SPPs) along the cone lateral surface. (c) Combining a Gaussian beam source and perfectly matched layer (PML) boundary conditions along the cone's upper boundary allows a 2 µm structure to accurately reflect the infinite cone limit.

Au cones of varying length (L) were optically pumped using either a Gaussian beam source [**Fig. 4.1(a)**; FWHM=833 nm at λ_{center}=576 nm] or a planewave spanning the entire simulation cross-section [**Fig. 4.1(b)**]. The enhancement spectra of shorter cones (L = 500-2000 nm) contain peaks and oscillations that correspond to LSP resonances supported by the finite metal surface between the apex and upper cone boundary. The intensity of these oscillations decreases for longer cones, and by L = 6 µm, they are completely absent for the beam source, resulting in a smooth enhancement spectrum that does not change with further increase in cone length. This transition occurs as the cone length exceeds the attenuation length of surface plasmon-polaritons (SPPs) confined to the Au-air interface, which is <5 μm for optical wavelengths [27]. SPPs launched at the apex will be almost fully attenuated before reflecting off the upper cone boundary and returning to the apex, thus making the 6+ μm cones respond equivalently to those of infinite length. In contrast, convergence to the infinite cone limit is slower for a planewave source, which fills the entire simulation space, because SPPs are launched all along the cone. As shown in **Figure 4.1(c)**, the simulation volume can be significantly reduced (i.e., 2 μm cone, converging to the 6 μm and infinite cone limit with < 1% error across all λ) using a beam source and perfectly-matched layer (PML) placed along the upper cone surface. The PML acts as a nearly perfect absorber, eliminating reflection of SPPs from the upper boundary for the Gaussian case, but only partially for planewave excitation.

There are numerous literature examples of cones with L ~ 100-1000 nm being used as models of scanning near-field probes [28-33]. As observed for the shorter cones in **Figure 4.1**, this causes the plasmonic response of the structure to be dominated by LSP modes *and* SPP reflections. In our work, we are specifically interested in characterizing the optical physics of probes with resonant apex nanostructures, and the presence of any plasmon resonances supported by the larger probe structure will tend to obscure those effects. For this reason, all subsequent results presented use the 2 μm cone + PML model. This ensures the baseline probe optical response is relatively flat and smooth, making it straightforward to identify the appearance of new LSPs created by apex nanostructuring.

The results presented in **Figure 4.1** are exclusively for solid Au cones, but near-field probes are also commonly made by metallizing an AFM tip. Simulations of Si probes with apex radii between 5-50 nm and uniform Au coatings of varying thickness were performed to determine if significant differences existed in the physics of these two probe models. The metal coating thickness and underlying support radius were varied while keeping the total radius (support+coating) constant. Enhancement spectra were examined to determine what coating thickness was necessary to completely mask the presence of the Si support. **Figure 4.2(a)** gives an example of results for a fixed probe radius of 25 nm, where a 20 nm Au coating on 5 nm Si probe is required to produce field enhancement within 10% of the solid Au probe. It is also seen that thinner Au coatings have large enhancement variations across the visible spectrum, likely due to interference effects from reflections within the cavity formed by the Au-coated Si probe apex. This interference phenomenon may be constructive (λ= 500 nm) or destructive (λ= 650 nm), and depends on the coating thickness, excitation wavelength, and optical pumping configuration. In practice, such interference is challenging to rationally incorporate into a probe design, as it is highly dependent on the local morphology of the probe and the excitation geometry of the optical source. No experimental demonstration in the literature could be found where metal coating thickness was used to tune interference resonances of this type.

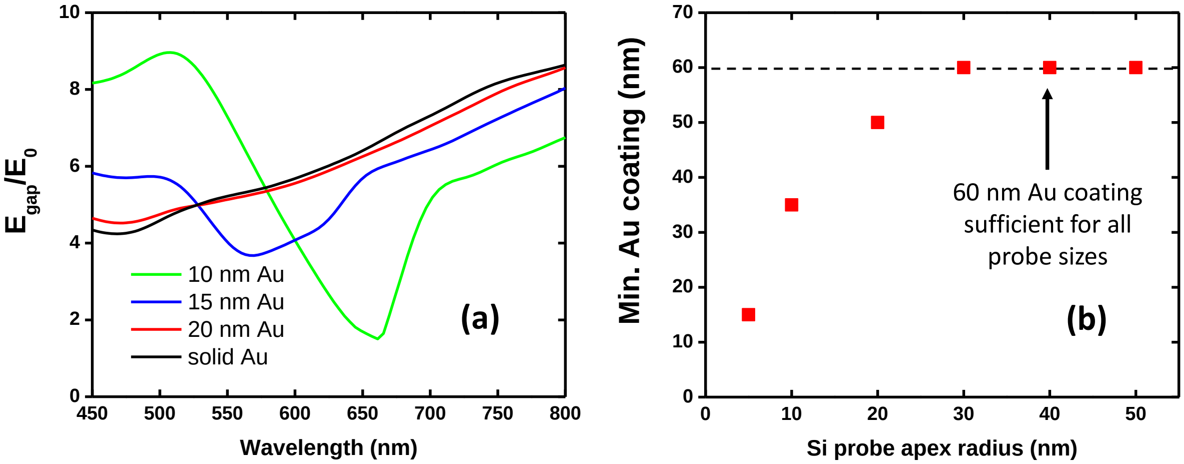

Figure 4.2 Plasmonic response of Au-coated Si probes of varying size in comparison to solid Au probes. (a) Enhancement spectra of Au-coated Si probes with a constant total radius (Si base + Au coating) of 25 nm and a cone angle of 15°. The 5 nm Si + 20 nm Au probe produces an optical response nearly identical to that of the 25 nm solid Au cone. (b) The minimum Au coating thickness required to optically mask the presence of the Si substrate as a function of apex radius. The excitation source was a 45° Gaussian beam with side-on illumination geometry with the probes placed 1 nm above a glass substrate.

The same process of varying Au/Si thickness was repeated systematically for probes with different total radius values until the minimum required Au coating thickness across a range of common near-field probe sizes could be determined [Fig. 4.2(b)]. A 60 nm Au coating was found to fully mask the presence of the Si support, regardless of the size of the Si structure. This is caused by the Au coating becoming essentially opaque, due strong absorption at optical frequencies, which prevents light from reaching the Si core. The transmission through a 60 nm Au film at normal incidence is <10% over the full visible spectrum. For smaller Si probes, the amount of Au deposited can be reduced significantly, e.g., a 5 nm Si probe requires only 15 nm of Au. The minimum amount of metal possible should be deposited to minimize the size of the probe apex, as sharper probes yield larger enhancements due to geometric field concentration (i.e., the lightning rod effect [34]), while also avoiding interference effects present for thin coatings. The general conclusion of our simulation benchmarking work is that a single model, namely the solid metal probe, can capture the important plasmon physics involved, even for metal-coated probes that would be used in practice. When combined with the local field normalization procedure used to reduce the influence of excitation geometry and optical source [see Numerical Methods], along with the 2 μm cone + PML model [**Fig. 4.1**] removing resonance contributions from the larger probe structure, a simulation procedure has been developed that allows the apex optical physics of near-field probes to be studied in a very general manner.

D. Engineering and optimizing resonant optical antennae

A quantitative comparison of several probes with specifically designed plasmonic resonances was made using the general FDTD framework developed in the previous section. The purpose in doing so is to provide the first quantitative comparison of the achievable enhancements from these structures, which is experimentally difficult due to differences in instrumentation, design wavelengths, and reporter molecules used to generate near-field scattering signals. A secondary goal is to understand how different material and geometric parameters influence the plasmonic behavior of probes, and to provide guidance on how to optimize the performance of these structures.

A straightforward means of producing a resonant near-field probe is the addition of a plasmonic nanoparticle/structure to the apex of a larger probe 'support' or tip. Attaching particles with diameters less than several hundred nanometers is challenging, but can be done by functionalizing the probe and/or nanoparticle with an organic linker (e.g., epoxy, sticky polymers, biotin-streptavadin, complementary DNA) [15-16] and then picking up a single particle by scanning the probe over a surface. Alternatively, plasmonic nanoparticles can be selectively grown at the probe apex via electrochemical reduction of metal ions in solution [35-36]. Regardless of the specific fabrication process used, the presence of the probe support material will modify the plasmon resonance of the attached nanoparticle. To characterize this effect, simulations were performed on a 50 nm dia. Au sphere with a 10 nm wide connecting junction of varying material [Fig. 4.3]. Six different junction materials were tested, three with very low extinction coefficients (SiO_2, Si_3N_4, Si) and three that strongly absorb at visible energies (Au, W, Pt). All of the high absorption materials were found to decrease local field enhancements relative to those of the isolated Au nanoparticle, due to the dipolar LSP of the sphere losing energy via absorption in the connection junction during each optical cycle. This damping contribution adds to the damping inherent to the nanoparticle and decreases the amplitude of charge oscillations in the nanoparticle when an optical field is applied.

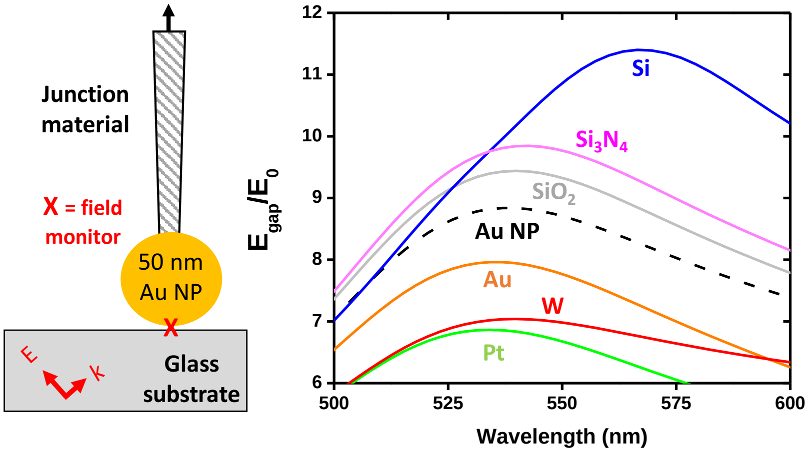

Junction Material	E_{max}	n @ E_{max}	κ @ E_{max}
Si	11.4	4.0	<0.1
Si_3N_4	9.8	2.0	<0.1
SiO_2	9.4	1.5	<0.1
Au NP only	**8.8**	**1**	**0**
Au	8.0	0.4	2.4
W	7.0	3.5	2.7
Pt	6.9	2.1	3.6

Figure 4.3 Perturbations to the dipolar LSP mode of an Au nanoparticle (dia.= 50 nm) caused by the addition of a 10 nm wide connecting junction. Materials that strongly absorb at optical energies (Au, W, Pt) cause damping of the plasmon resonance and lead to lower field enhancements, while those with small extinction coefficients (Si, Si_3N_4, SiO_2) increase the coupling of far-field radiation into the dipolar plasmon mode of the nanoparticle.

The observation that low extinction coefficient materials actually increase enhancements above those of the isolated sphere was unexpected. Justification for this effect can be found in the Mie solution for the extinction cross-section of a metal sphere in the quasistatic limit (size << λ) [37]. In this case, extinction is proportional to the polarizability of the sphere. The support material, with a refractive index greater than unity, increases the polarizability of the combined sphere-support structure, leading to a larger cross-section for coupling far-field radiation into the dipolar plasmon mode. This explanation is supported by the observation that absorption cross-sections for the apex spheres increased by ~100% for the Si junction compared to the isolated nanoparticle. Higher refractive index supports (Si) are more polarizable than low refractive index materials (SiO_2), which increases the magnitude of this effect and produces larger relative field enhancements.

The conclusion from **Figure 4.3** would appear to be that a high refractive index support material with low absorption, such as Si, is the ideal support for a nanoparticle-based near-field probe. Surprisingly, simulation and experimental data on Ag-coated conical supports show a different behavior, with low index materials yielding the largest optical fields [38-39]. This apparent contradiction was resolved when two additional resonant probe geometries were studied, namely a cone with an Au-coated apex and an Au-hemisphere on a post [**Fig. 4.4**]. The support materials that maximized enhancement were found to vary for both of these structures, as well as the nanoparticle functionalized probe discussed earlier, with refractive index values ranging from 2-4. From these data, it is clear that the idea of a universally superior support material is not correct. Instead, the support refractive index should be viewed as a parameter that can be optimized for a particular apex geometry. In general, higher index materials work well for solid plasmonic structures, where the support is connected at the surface, while low index supports are superior when the plasmonic metal is a thin film coating. Note that in all cases, the lossy Au and Pt substrates still produce weaker enhancements, consistent with the conclusions from **Figure 4.3**.

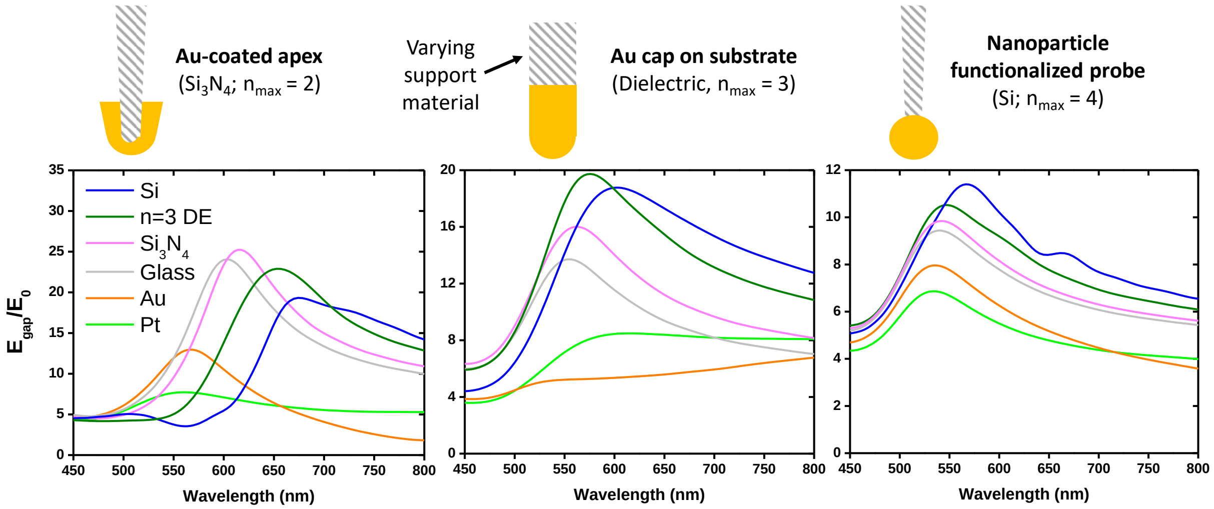

Figure 4.4 Enhancement spectra (E_{gap}/E_0) of near-field probes with resonant Au-apex nanostructures can be maximized by varying the refractive index of the support material. Probes were placed 1 nm above a glass surface with a 45° inverted beam source, and the support structures were extended to the simulation boundary, places 2 μm above the surface. The approximate refractive indices of the low absorption materials studied are: n = 1.5 (glass), 2 (Si_3N_4), 3 (a generic dielectric), and 4 (Si). Au and Pt were included as examples of lossy support materials and produced lower field enhancements for all three geometries simulated.

A resonant probe design with large potential enhancement that makes use of the aforementioned results can be constructed by FIB-milling a circular groove into a metallized commercial AFM probe a short distance above the probe apex [39-40], forming a nano-cone on the end of a dielectric post [**Fig. 4.5**]. A possible issue when applying the metal coating prior to FIB processing is that ion implantation from the FIB beam may degrade the plasmonic properties of the metal. This can be avoided by first making FIB cuts on the bare probe, and then evaporating metal normal to the probe axis so that the apex cone acts as a shadow mask

[39]. The position and size of the FIB cuts determine the apex length, post length, and post width of the final structure.

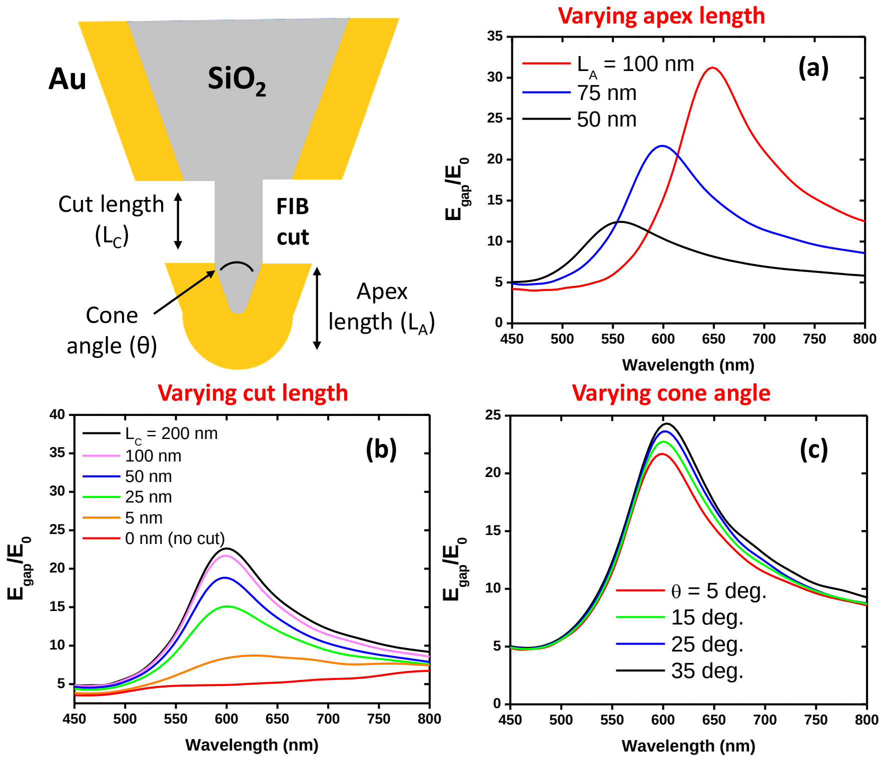

Figure 4.5 Effects of different geometric parameters on the field enhancement (E_{gap}/E_0) produced by a metal-coated SiO_2 probe with FIB structuring near the apex. (a) The LSP wavelength can be tuned by the apex length, with longer apexes producing larger enhancements. (b) A cut length of roughly 100 nm is necessary to optically decouple the metal apex from the coating on the rest of the probe surface. (c) The cone angle of the underlying support shows a weak positive correlation with enhancement. The default values of parameters not being varied in each series were: apex length = 75 nm, cut length = 100 nm, and cone angle = 15°. In all cases the SiO_2 apex radius was 5 nm with a 20 nm thick Au coating.

Simulations were used to estimate the enhancements produced by this structure as a function of the apex length, cut length, and cone angle. The apex length is the parameter used to primarily control the LSP wavelength, with longer lengths leading to red-shifting of the resonance [Fig. 4.5(a)]. The additional length of the dielectric support post also increases the total polarizability of the apex, providing stronger coupling with far-field excitation and hence larger enhancements. The cut length controls the optical coupling between the apex and support Au coatings [**Fig. 4.5(b)**]. Enhancement was found to increase with longer posts, with distances ≥100 nm being sufficient to optically isolate the apex metal layer from the rest of the probe tip. The cone angle is determined by the shape of the original probe being coated, but larger angles showing a weak positive correlation with enhancement [**Fig. 4.5(c)**]. A variation on the **Figure 4.5** structure, where FIB milling was performed parallel to the probe central axis instead of perpendicular to it, was proposed by Zou *et al.* [41]. In this design, the apex metal layer is tapered, and our simulations show that dipolar LSP modes are relatively weak; as such, this probe design was not considered in subsequent simulation studies.

Near-field probes that do not require a separate support, but instead involve direct structuring of a plasmonic material, have also been proposed. One design is a structure very similar to **Figure 4.5**, except that FIB cuts are now made in an etched, solid metal probe [42] [**Fig. 4.6(a)**]. Simulations of an Au probe of this type were run, and the trends for apex length, cut length, and cone angle were found to be similar to those given in **Figure 4.5**. A new observation was the dependence of LSP strength on the FIB cut depth. The magnitude of peak enhancement increased with cut depths up to 20-30 nm, beyond which, deeper cuts only altered the LSP peak energy. Making the cuts too deep raises concerns about the mechanical stability of the probe. For this reason, it is recommended that a probe with a wide cone angle be used, and the cut depth not exceed 20-30 nm. The original study by Vasconelos *et al.* reported a TERS signal increase of 5x, before and after the FIB process, for a probe with a relatively narrow cut length ($L_c \sim 25$ nm) [42]. Our simulations suggest that if the cut length were increased to 100 nm, while maintaining the same 20-30 nm cut depth, the apex electric field strength could be further doubled, and the TERS signal enhancement would be increased by an order of magnitude.

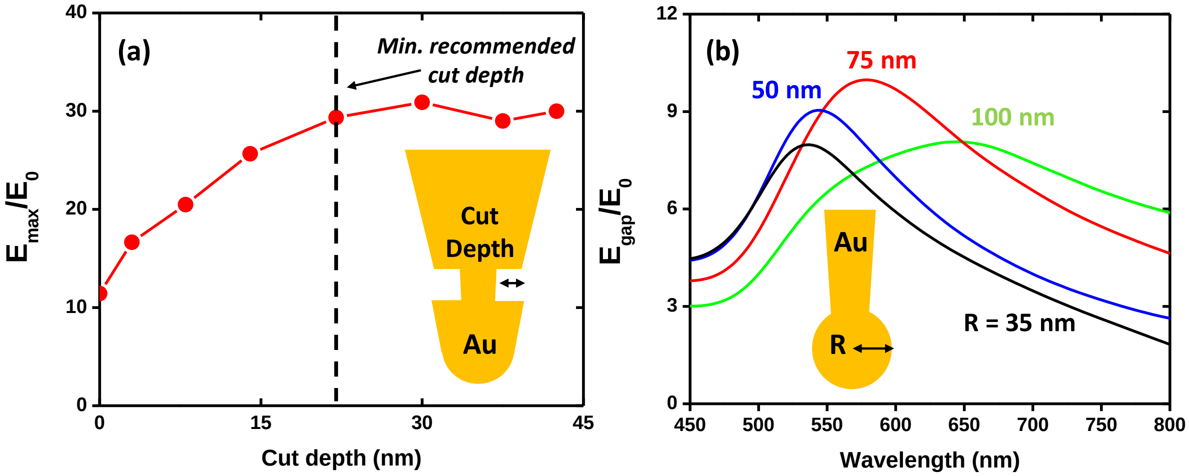

Figure 4.6 Important geometric parameters to control field enhancement of FIB-milled, solid Au near-field probes. (a) Field enhancement at the resonance peak (E_{max}) for a 35° Au cone as a function of the FIB cut depth. A minimum cut depth of approximately 20 nm is required to maximize the LSP resonance supported by the apex. (b) The apex radius of curvature is the primary LSP tuning parameter for probes with a sphere and cone geometry. This type of structure can be produced by metal coating a commercial AFM cantilever with an electron-beam deposited apex structure [36].

Another fully metallized probe design that has been proposed is to create a sphere at the end of a conical support and then apply a plasmonic metal coating [**Fig. 4.6(b)** inset]. Spherical structures can be grown on the apex of commercial AFM tips using electron-beam deposition of carbonaceous material [36, 43]. In this case, the LSP energy is primarily controlled by the radius of the apex sphere, with the connection width between the sphere and cone acting as a secondary tuning parameter. Enhancements were maximized using a sphere radius of R = 75 nm, with radii >100 nm showing a rapid decrease in field strength, corresponding to a loss of geometric field concentration (i.e., the probe is no longer sharp enough for a strong lightning rod effect). Even for spheres of moderate size, there will be some reduction in the lateral spatial localization of the enhanced fields. For example, the

FWHM of the $|E|^4$ profile along the probe-substrate gap nearly doubles from 12 nm to 22 nm for radius values of 35 nm and 75 nm, respectively.

The important physical parameters of several probe designs have now been described, and at this point, it is useful to ask which of these structures can produce the largest enhancements. To help answer this question, an effort was made to optimize the enhancements of each probe over a commonly used wavelength range (633-647 nm, for HeNe and Kr^+ laser lines) and subject to a similar set of design constraints [**Fig. 4.7(a)**]. The designs included were conical apex structures with FIB cuts in a metallized SiO_2 support (Probe 1) and solid Au etched wire (Probe 2), an Si support functionalized with an Au nanoparticle (Probe 3), a metallized sphere-cone structure (Probe 4), and a smooth semi-infinite cone (Probe 5) as a point of reference. Final values of the geometric parameters for each optimized probe are provided in **Table 4.1**, along with the constraints enforced on these parameters to maintain physically realistic structures. To eliminate the influence of probe sharpness on enhancement, the apex radius of curvature of all probes was intentionally fixed at 25 nm, except in the case of Probe 4, where increasing this value was necessary to tune the LSP energy.

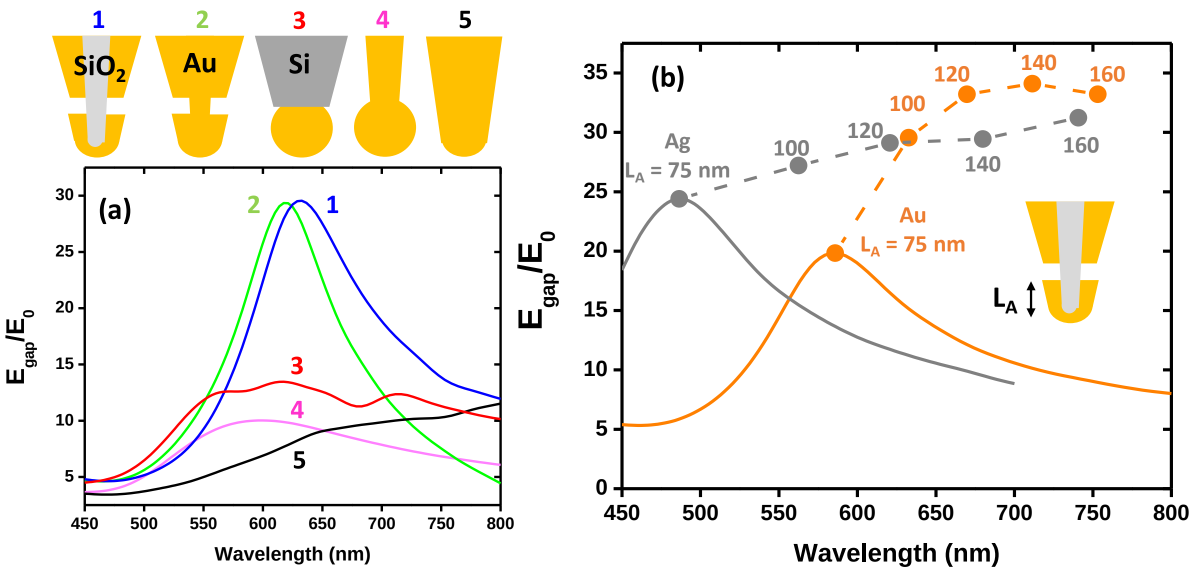

Figure 4.7 Comparison of several near-field probe designs that have been optimized for operation in the 633-647 nm wavelength range. (a) The Au-coated dielectric and solid Au designs with FIB cuts made near the apex were predicted to produce the largest apex field enhancements (E_{gap}/E_0). (b) Example of tuning the LSP energy of a metal-coated SiO_2 probe over the full visible spectrum by varying the coating metal (Ag vs. Au) and apex length. All other parameters are the same as the Probe 1 structure in panel (a). Points represent the wavelength of maximum field enhancement.

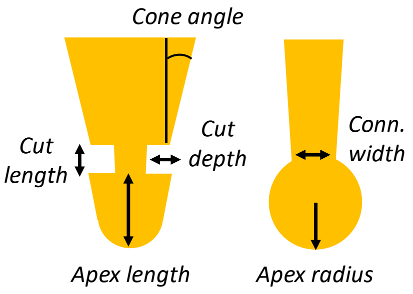

Probe #	Apex radius [nm]	Cone angle [deg.]	Apex length [nm]	Cut length [nm]	Cut depth [nm]	Conn. width [nm]
1	25	15	100	100	20	-
2	25	35	115	100	30	-
3	25	15	-	-	-	50
4	75	15	-	-	-	40
5	25	35	-	-	-	-
Constraints	≥ 25	15-35	None	≤ 100	≤ 30	≥ 40

Table 4.1 Geometric parameters of the optimized probe structures presented in Fig. 7. Cone angles in the range of 15-35° capture the apex profiles of commonly used commercial AFM tips and electrochemically etched wires. Constraints were placed on the allowed values of the cut length, cut depth, and connection width to maintain reasonable mechanical stability of the structures. Geometric constraints were imposed using conservative estimates from available experimental data on similar probes that have been fabricated and used in various scanning probe instruments.

Of the designs considered, maximum field enhancements (~30x) were achieved using probes with FIB-milled apex grooves (Probes 1 and 2). This corresponds to a 300% increase when compared to the unstructured metal cone (Probe 5), which may yield an improvement in TERS signal of two orders of magnitude, based on the typical $|E|^4$ estimation. Moreover, the resonance energy for maximum enhancement can be easily tuned by varying the chosen plasmonic material and apex length [**Fig. 4.7(b)**]. Au coatings are effective above 600 nm, where absorption from interband transitions is avoided; Ag coatings are expected to be effective over the entire visible spectrum. Experimental measurements using EELS, dark-field scattering, and TERS have verified the red-shifting of the LSP energy with increasing apex length [39-40, 42]. Although not simulated here, experiments using Au probes have also shown that the LSP dipole mode can be further extended into the near infrared range [42].

Nanoparticle functionalized structures (Probe 3) produced broadband enhancement of moderate intensity when a high refractive index support material (e.g., Si) was used. The use of metallic supports (Pt, W) led to much lower enhancements, while the use of another plasmonic material (Au) gave intermediate results, similar to the Probe 4 design. This suggests that dielectric probes with attached plasmonic nanoparticles are more effective than conductive probes with plasmonic structures selectively grown at the apex using electrochemistry. Enhancements were found to depend strongly on the nanoparticle attachment position (data not shown), with particles located on the side of probes yielding lower enhancements than attachments directly beneath the apex. This is because the nanoparticle dipolar LSP has two field nodes oriented nearly perpendicular to the sample surface, and the support more strongly influences the LSP when the support is placed directly at the position of the upper field node. It is expected that the enhancements of these probes could be further increased by 2-3x via attachment of more asymmetric nanoparticles (e.g. nanorods) with the long axis aligned perpendicular to the sample surface. The sphere and cone geometry (Probe 4) gave relatively low enhancements, as the LSP energy could not be adjusted without increasing the apex radius of curvature, thereby reducing the effect of geometric field concentration.

It should also be noted that the results presented in this work were obtained with the probes positioned 1 nm above an SiO_2 substrate. A limited set of simulations were also performed using a 45° inclined, side-on excitation geometry in which the substrate material was varied (SiO_2, Si, Pt, Au). The purpose of this study was to determine if the enhancement ratio of the resonant groove designs (Probes 1 and 2) compared to the unstructured cone (Probe 5) was a function of the substrate optical properties. For SiO_2 and Si substrates, the on-resonance enhancement ratio was ~3, while for Au substrates the ratio decreased to 1.5. The lower relative improvement for Au substrates is caused by the existence of a strong gap-mode plasmon that is supported even in the case of the unstructured cone. This situation lessens the importance of the additional apex LSP mode. A Pt substrate was also tested as an example of a metal without optical plasmonic behavior, and an intermediate enhancement ratio of 2 was obtained. Thus, resonant probes are not as critical for improving signal levels when metallic substrates are used, but they may still provide increases in electric fields of 50-100%.

E. Conclusions

FDTD simulations were used to evaluate the efficacy of several near-field probe designs with engineered localized surface plasmon modes supported at their apices. For probes with a support material separate from the plasmonic metal used for primary optical field enhancement, such as plasmonic nanoparticle functionalized AFM tips, the refractive index and extinction coefficient of the support were found to be critical in controlling the plasmonic properties. Support materials with strong absorption at optical energies (Pt, W) were found to damp plasmon resonances and lead to lower enhancements, while those with relatively low absorption (SiO_2, Si_3N_4, Si) could actually be used to increase enhancements by boosting the extinction cross-section of the nanostructure. These results imply that nanoparticle functionalized probes will yield greater enhancements than conductive structures created via electrodeposition of a plasmonic metal at the apex.

Probe designs predicted to give the largest local field enhancement (~30x) were those with grooves near the probe apex, made using focused ion-beam milling. Compared to an unstructured metal cone of similar size, FIB-milled probes provide a 300% improvement in field strength, and a potential boost in TERS signals of 1-2 orders of magnitude. Moreover, the resonance energy of these high-enhancement structures can also be tuned to cover visible and near-infrared energies by varying the plasmonic metal (Ag or Au) and the groove position relative to the apex. A barrier to more widespread use of these designs is the production cost associated with milling individual probes. However, they should be viewed as a useful option for experiments where signal levels are low, particularly for non-metallic substrates where gap-mode plasmons cannot be leveraged, or for resonant spectroscopy applications where the probe plasmon energy must be precisely tuned to match molecular transitions.

References

1. Hayazawa, N.; Inouye, Y.; Sekkat, Z.; Kawata, S., Near-field Raman scattering enhanced by a metallized tip. *Chemical Physics Letters* **2001,** *335* (5-6), 369-374.
2. Ren, B.; Picardi, G.; Pettinger, B., Preparation of gold tips suitable for tip-enhanced Raman spectroscopy and light emission by electrochemical etching. *Review of Scientific Instruments* **2004,** *75* (4), 837-841.
3. Schmid, T.; Opilik, L.; Blum, C.; Zenobi, R., Nanoscale chemical imaging using tip-enhanced Raman spectroscopy: a critical review. *Angewandte Chemie International Edition* **2013,** *52* (23), 5940-5954.
4. Blum, C.; Opilik, L.; Atkin, J. M.; Braun, K.; Kämmer, S. B.; Kravtsov, V.; Kumar, N.; Lemeshko, S.; Li, J. F.; Luszcz, K., Tip-enhanced Raman spectroscopy–an interlaboratory reproducibility and comparison study. *Journal of Raman Spectroscopy* **2014,** *45* (1), 22-31.
5. Pettinger, B.; Domke, K. F.; Zhang, D.; Schuster, R.; Ertl, G., Direct monitoring of plasmon resonances in a tip-surface gap of varying width. *Physical Review B* **2007,** *76* (11), 113409.
6. Hayazawa, N.; Ishitobi, H.; Taguchi, A.; Tarun, A.; Ikeda, K.; Kawata, S., Focused excitation of surface plasmon polaritons based on gap-mode in tip-enhanced spectroscopy. *Japanese Journal of Applied Physics* **2007,** *46* (12R), 7995.
7. Ikeda, K.; Fujimoto, N.; Uehara, H.; Uosaki, K., Raman scattering of aryl isocyanide monolayers on atomically flat Au (1 1 1) single crystal surfaces enhanced by gap-mode plasmon excitation. *Chemical Physics Letters* **2008,** *460* (1-3), 205-208.
8. Picardi, G.; Chaigneau, M.; Ossikovski, R., High resolution probing of multi wall carbon nanotubes by tip enhanced Raman spectroscopy in gap-mode. *Chemical Physics Letters* **2009,** *469* (1-3), 161-165.
9. Meng, L.; Yang, Z.; Chen, J.; Sun, M., Effect of electric field gradient on sub-nanometer spatial resolution of tip-enhanced Raman spectroscopy. *Scientific reports* **2015,** *5*, 9240.
10. Aikens, C. M.; Madison, L. R.; Schatz, G. C., Raman spectroscopy: The effect of field gradient on SERS. *Nature Photonics* **2013,** *7* (7), 508.
11. Zhang, R.; Zhang, Y.; Dong, Z.; Jiang, S.; Zhang, C.; Chen, L.; Zhang, L.; Liao, Y.; Aizpurua, J.; Luo, Y. e., Chemical mapping of a single molecule by plasmon-enhanced Raman scattering. *Nature* **2013,** *498* (7452), 82.
12. Chen, C.; Hayazawa, N.; Kawata, S., A 1.7 nm resolution chemical analysis of carbon nanotubes by tip-enhanced Raman imaging in the ambient. *Nature communications* **2014,** *5*, 3312.
13. Chiang, N.; Chen, X.; Goubert, G.; Chulhai, D. V.; Chen, X.; Pozzi, E. A.; Jiang, N.; Hersam, M. C.; Seideman, T.; Jensen, L., Conformational contrast of surface-mediated molecular switches yields Ångstrom-scale spatial resolution in ultrahigh vacuum tip-enhanced Raman spectroscopy. *Nano letters* **2016,** *16* (12), 7774-7778.
14. Shi, X.; Coca-López, N. s.; Janik, J.; Hartschuh, A., Advances in tip-enhanced near-field Raman microscopy using nanoantennas. *Chemical reviews* **2017,** *117* (7), 4945-4960.
15. Kim, W.; Kim, N.; Lee, E.; Kim, D.; Kim, Z. H.; Park, J. W., A tunable Au core–Ag shell nanoparticle tip for tip-enhanced spectroscopy. *Analyst* **2016,** *141* (17), 5066-5070.
16. Kalkbrenner, T.; Ramstein, M.; Mlynek, J.; Sandoghdar, V., A single gold particle as a probe for apertureless scanning near-field optical microscopy. *Journal of microscopy* **2001,** *202* (1), 72-76.
17. Palik, E. D., *Handbook of Optical Constants of Solids*. Elsevier: 1997; Vol. I-III.

18. Luke, K.; Okawachi, Y.; Lamont, M. R.; Gaeta, A. L.; Lipson, M., Broadband mid-infrared frequency comb generation in a Si 3 N 4 microresonator. *Optics letters* **2015,** *40* (21), 4823-4826.
19. Yang, Z.; Aizpurua, J.; Xu, H., Electromagnetic field enhancement in TERS configurations. *Journal of Raman Spectroscopy: An International Journal for Original Work in all Aspects of Raman Spectroscopy, Including Higher Order Processes, and also Brillouin and Rayleigh Scattering* **2009,** *40* (10), 1343-1348.
20. Kazemi-Zanjani, N.; Vedraine, S.; Lagugné-Labarthet, F., Localized enhancement of electric field in tip-enhanced Raman spectroscopy using radially and linearly polarized light. *Optics express* **2013,** *21* (21), 25271-25276.
21. Behr, N.; Raschke, M. B., Optical Antenna Properties of Scanning Probe Tips: Plasmonic Light Scattering, Tip− Sample Coupling, and Near-Field Enhancement. *The Journal of Physical Chemistry C* **2008,** *112* (10), 3766-3773.
22. Stadler, J.; Oswald, B.; Schmid, T.; Zenobi, R., Characterizing unusual metal substrates for gap-mode tip-enhanced Raman spectroscopy. *Journal of Raman Spectroscopy* **2013,** *44* (2), 227-233.
23. Lu, C.; Tang, P.; Lu, X.; Zhang, Q.; Liu, S.; Tian, J.; Zhong, L., Theoretical Localized Electric Field Enhancement in Tip-Enhanced Spectroscopy Using Multi-Order Radially Polarized Modes. *Plasmonics* **2018**, 1-8.
24. Zhang, W.; Cui, X.; Martin, O. J., Local field enhancement of an infinite conical metal tip illuminated by a focused beam. *Journal of Raman Spectroscopy: An International Journal for Original Work in all Aspects of Raman Spectroscopy, Including Higher Order Processes, and also Brillouin and Rayleigh Scattering* **2009,** *40* (10), 1338-1342.
25. Kitahama, Y.; Itoh, T.; Suzuki, T., Calculated shape dependence of electromagnetic field in tip-enhanced Raman scattering by using a monopole antenna model. *Spectrochimica Acta Part A: Molecular and Biomolecular Spectroscopy* **2018,** *197*, 142-147.
26. Krug, J. T.; Sánchez, E. J.; Xie, X. S., Design of near-field optical probes with optimal field enhancement by finite difference time domain electromagnetic simulation. *The Journal of chemical physics* **2002,** *116* (24), 10895-10901.
27. Kolomenski, A.; Kolomenskii, A.; Noel, J.; Peng, S.; Schuessler, H., Propagation length of surface plasmons in a metal film with roughness. *Applied optics* **2009,** *48* (30), 5683-5691.
28. Demming, A.; Festy, F.; Richards, D., Plasmon resonances on metal tips: understanding tip-enhanced Raman scattering. *The Journal of chemical physics* **2005,** *122* (18), 184716.
29. Goncharenko, A.; Chang, H.-C.; Wang, J.-K., Electric near-field enhancing properties of a finite-size metal conical nano-tip. *ultramicroscopy* **2007,** *107* (2-3), 151-157.
30. Huber, C.; Trügler, A.; Hohenester, U.; Prior, Y.; Kautek, W., Optical near-field excitation at commercial scanning probe microscopy tips: a theoretical and experimental investigation. *Physical Chemistry Chemical Physics* **2014,** *16* (6), 2289-2296.
31. Roth, R. M.; Panoiu, N. C.; Adams, M. M.; Osgood, R. M.; Neacsu, C. C.; Raschke, M. B., Resonant-plasmon field enhancement from asymmetrically illuminated conical metallic-probe tips. *Optics express* **2006,** *14* (7), 2921-2931.
32. Meng, L.; Huang, T.; Wang, X.; Chen, S.; Yang, Z.; Ren, B., Gold-coated AFM tips for tip-enhanced Raman spectroscopy: theoretical calculation and experimental demonstration. *Optics express* **2015,** *23* (11), 13804-13813.
33. Sukharev, M.; Seideman, T., Optical properties of metal tips for tip-enhanced spectroscopies. *The Journal of Physical Chemistry A* **2009,** *113* (26), 7508-7513.

34. Liao, P.; Wokaun, A., Lightning rod effect in surface enhanced Raman scattering. *The Journal of Chemical Physics* **1982,** *76* (1), 751-752.
35. Wang, H.; Tian, T.; Zhang, Y.; Pan, Z.; Wang, Y.; Xiao, Z., Sequential electrochemical oxidation and site-selective growth of nanoparticles onto AFM probes. *Langmuir* **2008,** *24* (16), 8918-8922.
36. Sanders, A.; Zhang, L.; Bowman, R. W.; Herrmann, L. O.; Baumberg, J. J., Facile Fabrication of Spherical Nanoparticle-Tipped AFM Probes for Plasmonic Applications. *Particle & Particle Systems Characterization* **2015,** *32* (2), 182-187.
37. Lakowicz, J. R., Radiative decay engineering 5: metal-enhanced fluorescence and plasmon emission. *Analytical biochemistry* **2005,** *337* (2), 171-194.
38. Taguchi, A.; Hayazawa, N.; Saito, Y.; Ishitobi, H.; Tarun, A.; Kawata, S., Controlling the plasmon resonance wavelength in metal-coated probe using refractive index modification. *Optics express* **2009,** *17* (8), 6509-6518.
39. Maouli, I.; Taguchi, A.; Saito, Y.; Kawata, S.; Verma, P., Optical antennas for tunable enhancement in tip-enhanced Raman spectroscopy imaging. *Applied Physics Express* **2015,** *8* (3), 032401.
40. Zhu, L.; Georgi, C.; Hecker, M.; Rinderknecht, J.; Mai, A.; Ritz, Y.; Zschech, E., Nano-Raman spectroscopy with metallized atomic force microscopy tips on strained silicon structures. *Journal of Applied Physics* **2007,** *101* (10), 104305.
41. Zou, Y.; Steinvurzel, P.; Yang, T.; Crozier, K. B., Surface plasmon resonances of optical antenna atomic force microscope tips. *Applied Physics Letters* **2009,** *94* (17), 171107.
42. Vasconcelos, T. L.; Archanjo, B. S.; Fragneaud, B.; Oliveira, B. S.; Riikonen, J.; Li, C.; Ribeiro, D. S.; Rabelo, C.; Rodrigues, W. N.; Jorio, A., Tuning localized surface plasmon resonance in scanning near-field optical microscopy probes. *ACS nano* **2015,** *9* (6), 6297-6304.
43. Sanders, A.; Bowman, R. W.; Zhang, L.; Turek, V.; Sigle, D. O.; Lombardi, A.; Weller, L.; Baumberg, J. J., Understanding the plasmonics of nanostructured atomic force microscopy tips. *Applied Physics Letters* **2016,** *109* (15), 153110.

Chapter V. Importance of Physically Relevant Length Scales in Predicting Field Enhancements of Plasmonic Nanoparticle Dimers

Abstract

The optical properties of two Au spheres with varying inter-particle distance were characterized using finite-difference time-domain simulations, with an emphasis on geometries where the particles are fused along a common boundary. Previous modeling efforts on this system predicted that fused geometries would produce very large surface-enhanced Raman scattering (SERS) enhancements, significantly greater than those of the corresponding separated spheres. We demonstrate that these large enhancements are a numerical artifact caused by divergence of fields at the point of sphere surface intersection. The use of sub-nanometer spatial discretization within this region leads to the generation of arbitrarily large, highly-confined optical fields. Our own simulations, using a metal bridging structure to enforce physically relevant minimum gap distances on the order of 5-20 Å, yield much smaller field enhancements that are comparable to those estimated using more extensive non-local and quantum optical models. The effects of experimentally relevant geometric parameters, such as the inter-sphere contact area, surface intersection angle, and dielectric coating thickness, on the plasmon resonances of the separated and fused dimer structures are also examined. Fused sphere dimers are predicted to produce strong, tunable enhancements throughout the near-infrared spectrum, but the extreme sensitivity of these plasmon modes to small structural variations may hinder the reproducible fabrication of such optical antennae.

A. Introduction

Near-field optical simulations are crucial for the rational design of structures that control and manipulate light over sub-λ length scales. This is critical for both surface and tip-enhanced near-field optical spectroscopies, such as SERS, TERS, and SNOM. Numerical solutions of Maxwell's equations provide a general framework for modeling electromagnetic fields in complex geometries, but appropriate physical models must be chosen to represent the system of interest. We will define classical optical models as those with locally defined permittivity values and discontinuous transitions between materials at interfaces. When using such models, there are several geometries known to produce divergent (infinite) electromagnetic fields. These include "sharp" features, such as spikes, corners, or edges with zero radius of curvature, as well as small gaps between structures. In the present work, we focus on the modeling of a particular plasmonic antenna geometry in which two spheres are joined along a common boundary [**Fig. 5.1**]. When treated classically, these structures produce divergent optical fields at the intersection of surface boundaries. Previous studies have not identified the singular nature of fields in this region, which has led to predictions of very large local electric fields [1-4]. Our own classical optical simulations of fused Au spheres circumvent this issue by incorporating a cylindrical metal bridge that allows the minimum gap distance between sphere surfaces to be directly controlled. When physically relevant gaps in the range of 5-20 Å were tested, the resulting fields decreased significantly, on par with predictions from more detailed non-local and quantum optical models [5-7].

Figure 5.1 illustrates the joined sphere geometry with and without a metal bridging structure present. Pairs of joined spheres will be referred to as fused dimers, while the more commonly studied system, spheres with a finite gap between them, will be separated dimers.

Although only a two-sphere model is discussed, the results obtained are generally relevant for understanding the optical transitions that occur during the joining of any two plasmonic nanostructures. The bridge is an Au cylinder with a radius that can be adjusted to determine the minimum gap length scale (L_{min}). Previous work incorporating bridges into the simulation of sphere dimers has included distance-dependent conduction channels [7-8] and rounded metal toroids [9]. Our contribution to this discussion is the first calculation of the electromagnetic enhancement factors using physically relevant minimum gap distances. Some important questions about dimer antennae may then be answered, including: Do separated or fused dimer structures offer the largest electromagnetic enhancements? How does the wavelength dependence of enhancement differ between these structures? What are the dominant geometric parameters that control resonant phenomena? We provide answers to all these questions in the subsequent sections.

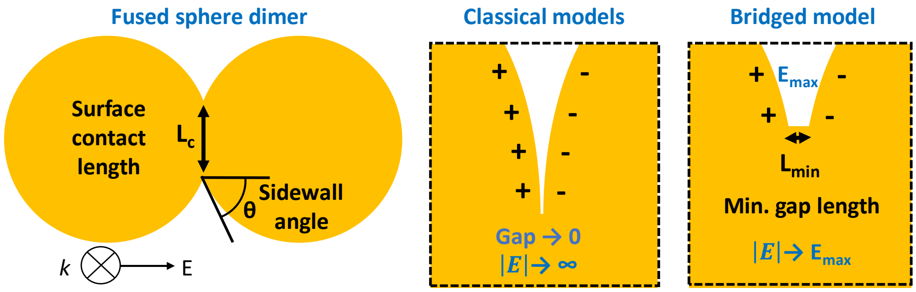

Figure 5.1 Diagram of a fused sphere dimer geometry in which two Au spheres are joined along a common interface. The expanded views illustrate the difference between classical and bridged optical models at the point of surface intersection between the spheres. Several geometric parameters (L_c, θ, L_{min}) are introduced that will subsequently be used to describe different structures under investigation.

Several physical justifications exist for the use of a conductive bridge to help model very small gap distances. A direct argument is that transmission electron microscopy (TEM) images of fused nanoparticles display rounded points of intersection between particle surfaces, with a minimum gap width of roughly 1 nm [2, 10]. This rounding is caused by atomic rearrangements that occur during the fusing process. Even if some dimers do contain sub-nanometer gaps, the physical size of analyte molecules may still limit the accessibility of these regions. For example, the size of a rhodamine 6G molecule, one of the most widely studied analytes in near-field Raman experiments, is on the order of 1 nm [11].

Another argument for the use of metallic bridges is that they emulate certain features of more advanced optical models. Some of these latter techniques construct non-local permittivity functions that attempt to mimic the electron dynamics of real materials [12-16]. Maxwell's equations are then solved simultaneously with the constitutive permittivity equation. In the context of small gaps, most non-local models predict significant spatially spreading of charge at material boundaries, in contrast to the highly localized surface charging of classical models. At the smallest length scales, quantum optical calculations using time-dependent density functional theory are feasible. Fully atomistic studies are limited to nanoscale systems with relatively few electrons [17-18], but Jellium models, those that explicitly consider only valence electrons, can increase this size limit into the range of larger plasmonic nanoparticles [5-6]. Quantum models also predict electron tunneling over sub-nanometer gaps, allowing charge to be exchanged between structures. Both non-local and quantum models predict the emergence of novel charge-transfer plasmon (CTP) modes near the point of surface contact (fusing). Solid metal bridging structures partially imitate these effects by creating an artificial direct conduction pathway, the length scale of which is controlled solely by the inter-particle size of the bridge.

It is important to note that there are variations in field predictions with different non-local and quantum optical models, but the plurality of the results can be summarized using two guidelines. The first is that, for gaps in the 5-20 Å range, quantitative differences between classical and non-local/quantum models become significant (>50%), with classical models universally overpredicting local field strengths. The second is that at separations <5 Å, classical models give qualitatively incorrect results, showing increasing fields strengths, while non-local/quantum predictions show decreasing fields and a smooth emergence of CTP modes. Optical and electrical measurements on metal nanogaps have universally supported the non-local and quantum predictions [10, 19-24]. Thus, it can be asserted that classical optical simulations of gaps below ~5Å do not produce physically meaningful results. It is still common to find literature examples of classical optical solvers applied to gaps on this length scale [9, 25-29]. In some cases, qualifiers are included stating that the results for such small gaps may be unreliable. These can be easy to miss, and it is ultimately up to researchers to be well-informed on the subject and actively discern whether the results of optical simulations correspond to reality.

B. Modeling Methods

Finite-difference time-domain (FDTD) optical simulations using the Lumerical software package were used to characterize the optical response of plasmonic dimer geometries. The simulations consisted of a cubic volume (0.5 x 0.5 x 0.5 μm^3) with perfectly matched layer boundary conditions and the dimer structures centered at the origin. A total-field scattered field broadband optical source, which is equivalent to a planewave, with linear polarization along the interparticle axis was placed 50 nm away from the dimer. Adaptive meshing was used to define a 0.25 nm mesh region over the volume of the dimers, with an additional fine mesh region equal to ¼ the gap distance being implemented for geometries with gaps less than 1 nm. Extensive convergence testing was performed on all simulation parameters to confirm that results were free of numerical artifacts. Optical data for Au at visible and near-infrared energies was obtained from *The Handbook of Optical Solids* [30].

Calculating the electromagnetic enhancement factor (EM-EF) of a dimer antenna requires integration of the electric field over the full surface of the structure. In three dimensions, this can generate excessively large data files that are cumbersome to store and analyze. A simplified procedure was developed in which field data from a single plane monitor, or two plane monitors in the case of fused dimers, was sufficient to approximate the full surface field integrals with errors below 1%. This was possible because the antenna sizes were small (<10%) compared to the optical excitation wavelengths, and the polarization was along a symmetry plane of the dimer structure. The full details of this procedure are provided in Appendix A5.1.

C. Demonstration of field divergence in classical optical models

Before presenting results on dimer systems, it is useful to examine a quantitative example of what field divergence looks like in classical optical simulations. The effect has been well-characterized for separated dimers as the inter-sphere distance approaches zero [9, 31]. In this case, the sphere surfaces undergo transient charging in the presence of an applied oscillatory electric field (light). Classical models do not allow charge transfer to occur between the surfaces over any gap distance. Thus, as the surfaces are brought together, the field magnitude between them will increase in an unbounded manner, with the divergence scaling approximately as $|E| \sim 1/(\text{gap-width})^n$ [3, 32-33]. The exact exponent (n) is usually close to 1 but depends on the specific geometry and materials involved in the gap formation.

The situation changes in the case of fused dimers, as there is now a direct conduction pathway between the spheres (the fused segment). In light of this, it is not obvious that divergent fields would persist. To show this is in fact the case, a simple 2D model using a triangular notch in a planar substrate was studied [**Fig. 5.2**]. A broadband plane wave (450-800 nm) was directed at normal incidence onto the 10 nm deep notch. For the first set of tests, the notch angle was held constant at 80° while the simulation mesh size was reduced over two orders of magnitude (10 to 0.1 Å). The maximum electric field, selected over the entire visible spectrum, was recorded at the base of the notch for each mesh size [**Fig. 5.2(a)**]. The field values were found to monotonically increase and were well-described by a power law relation. The divergence was strongest for visible light active plasmonic materials, both Au and Ag, with scaling exponents around 0.9. In contrast, the scaling for a non-plasmonic metal like Ti was only 0.35, and that of SiO_2 was <0.1. The exponents were also found to depend on the notch angle; for example, the Au exponent decreased to 0.64 with a 60° notch angle. These results show that the predicted field values can be varied over several orders of magnitude simply by changing the discretization used at the singular simulation region, with arbitrarily small meshes producing arbitrarily large local fields.

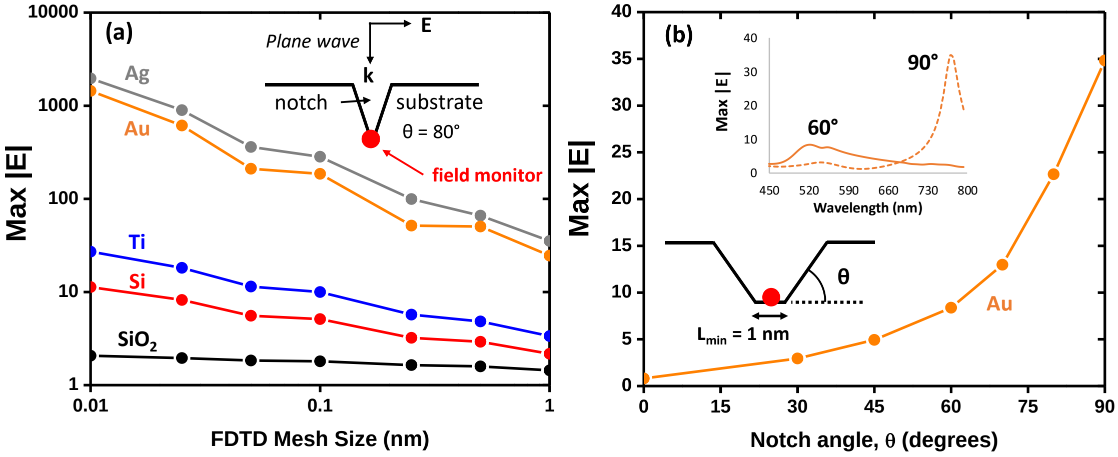

Figure 5.2 Classical 2D FDTD simulation results for a notch in a uniform substrate under plane wave illumination; λ=450-800 nm. (a) For surfaces intersecting at a common point, the maximum E-fields increase monotonically as the mesh size is reduced. The divergence is most pronounced for plasmonic materials (Au/Ag). The angle is held constant at 80°. (b) E-field values at the base of a notch with 1 nm min. width at varying sidewall angles. This geometry is similar to the crevices between fused plasmonic structures with a min. length scale enforced. The inset shows a large red-shift in resonance as the notch angle is changed from 60° to 90°. Connecting lines are only intended to guide the eye.

The field response of the notch with a bridging structure of 1 nm included was also evaluated [Fig. 5.2(b)] for different notch angles. These simulations mimic the point of surface intersection in bridged sphere dimers that will be subsequently discussed. A mesh size of 1Å gave fully converged results. The sidewall angle was varied between the limits of a flat substrate (0°) and a 1 nm x 10 nm vertical, rectangular channel (90°). The electric field at the base of the notch was found to be a strong function of this angle, with a maximum enhancement of 35 times the free-space value being achieved at 90°. The wavelength of peak enhancement was also observed to red-shift significantly at higher angles, similar to the effect observed for decreasing the gap distance of separated dimers [31]. Overall, the notch results indicate that field divergence should be expected when modeling fused spheres of plasmonic materials, with parameters such as the mesh size, bridge distance (L_{min}), and surface contact angle (θ) all affecting the rate at which divergence occurs.

D. Optical field enhancements of separated and fused dimers

(i) Varying separation and overlap length

In near-field optical spectroscopy, the net increase in scattering signal (e.g., Rayleigh, Raman, photoluminescence) generated by a structure is more important than the local field strength itself. This is referred to as an enhancement factor (EF). Both local and global EF values can be defined. A local EF is the ratio of the scattering signal produced by an analyte placed at a single point in space, with and without an enhancing structure present. A global EF is a 2D or 3D spatial average of local EFs. For surface-enhanced Raman scattering (SERS) structures, this is frequently the entire surface of the structure. Global EFs can be experimentally accessed by measuring the signal ratio between an enhancing surface and an appropriate blank, normally a bare substrate.

We will exclusively focus our subsequent discussion on enhancements of Raman optical scattering, where the dominant enhancement contribution is the electromagnetic concentration and amplification of light. The global enhancement of a structure via this mechanism will be referred to as the electromagnetic enhancement factor (EM-EF). Secondary effects, such as chemical enhancement, remain challenging to predict and quantify, but are known to play a much smaller role in enhancement for the vast majority of systems [34-35]. The standard method for estimating EM-EF values of Raman scattering is to compute the spatial average of the fourth-power of the local electric fields ($<E^4>$). The fourth power comes from both the focusing of incident radiation and amplification of scattered light from an analyte [36]. If dipole re-radiation of analyte molecules is included in the analysis, the scattering enhancement can change significantly for certain geometries [37]. Nevertheless, computing $<E^4>$, with no analyte present, has become the standard metric to gauge enhancement of near-field antennae, and allows quick comparisons to be made between different structures and simulation methods.

Figure 5.3 presents EM-EF values for a series of separated and fused dimer structures with varying gap and L_{min} distances. The dimers consist of two 50 nm dia. Au spheres. The separated dimers have gaps of 0.5, 1, and 2 nm, while the fused dimers all have a 0 nm gap, but varying L_{min} values of 0.5, 1, and 2 nm. EM-EFs were calculated by averaging the field values 1 nm above the dimer surface, except in the smallest gap regions where the mid-point between surfaces was used. A detailed description of the EM-EF calculation is given in Appendix A5.1, with the procedure designed to replicate that used by McMahon *et al.* [1].

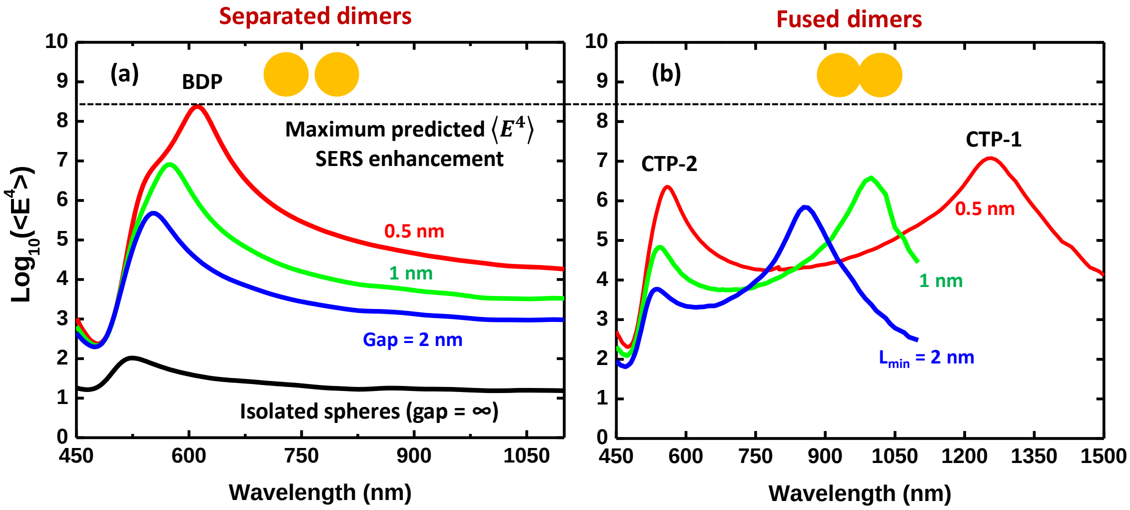

Figure 5.3 Estimates of electromagnetic Raman enhancements for separated (a) and fused (b) Au spheres. The supported plasmon modes of each structure are labeled as either a bonding dipole plasmon (BDP) or charge-transfer plasmon (CTP-1 and CTP-2). The electric fields were integrated at a distance 1 nm above the metal surface, except for small gap regions where the field values at the center of the gap were always used. See Appendix A5.1 for the full details of this calculation.

The separated dimers have a single peak in the visible spectrum that is attributed to the bonding dipole plasmon (BDP) mode, while the fused dimers display two peaks across the vis-to-NIR range attributed to charge-transfer plasmon (CTP) modes. It is clear that, for both separated and fused dimers, smaller gap distances produce increasingly larger EM-EF values. As discussed previously, this is caused by singular fields formed in small gaps between plasmonic materials. The EM-EFs are expected to increase further with a continued reduction the gap and L_{min} lengths, but this becomes computationally expensive in three dimensions. Instead, the analogous 2D geometry, corresponding to fused cylinders instead of spheres, was examined for gaps spanning 20 to 1.25 Å (see Appendix A5.2). The 2D fused cylinder EM-EFs increase by nearly 6 orders of magnitude over this range, a clear demonstration of continued field divergence. It should be noted that the volume of space containing the largest electric fields is always decreasing as the gap and L_{min} lengths are made smaller. The EM-EF increases, despite this volume decrease, because of the non-linear E^4 relation.

Figure 5.4 presents images of the electric field distributions associated with both BDP and CTP modes excited at their respective resonance energies. The BDP mode has a single field node centered between the spheres, while the CTP modes have a pair of nodes on each side of the connecting junction. A plot of the cumulative $\langle E^4 \rangle$ (EM-EF) signal fraction as a function of the integration distance along the surface contour of the dimers is also provided. A position of 0 nm corresponds to the start of the gap region where the integration is initialized. The cumulative signal plot shows that all of the modes have fields that are highly localized to the gap volume. Specifically, 90% of the EM-EF for the BDP and CTP-2 modes is generated within the first 3.5 nm, and within 5.5 nm for the CTP-1 mode. The lower spatial confinement of the CTP-1 mode is clear when comparing the images of each resonance, with enhanced fields being noticeably more spread out over the entire dimer surface.

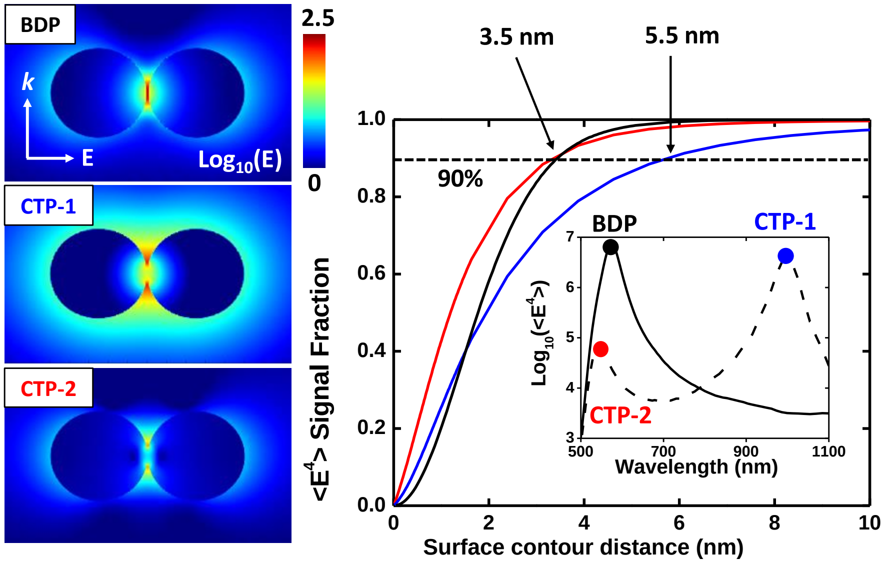

Figure 5.4 Electric field plots for the BDP and CTP modes of dimer structures excited on-resonance. For visual clarity, the fields are displayed using a logarithmic scale with equal limits. A cumulative plot of the fractional contribution to the total <E^4> values (EM-EF) of both structures are also given to measure the spatial confinement of the modes. A surface contour distance of 0 nm corresponds to the position at the start of the gap region, with positive values corresponding to integration over the sphere surfaces at an offset distance of 1 nm.

At gap and L_{min} values of 0.5 nm, the maximum EM-EF value of the separated dimer is more than an order of magnitude larger than that of the fused structure [Fig. 5.3]. This is in stark contrast to previous reports on fused dimers that assign them EM-EF values 1-4 orders of magnitude larger than the comparable separated dimers [1-3]. Other authors do not report EM-EF, but, based on stated local field strengths [9] or scattering spectra [4], the results are indicative of gaps well below 1 nm being simulated. The field values in all these studies differ somewhat, due to varying sphere sizes and materials, but there is no indication that the presence and importance of singular behavior for fused dimers was considered. Romero *et al.* identified this effect, but did not mention that singularities are present for all overlap distances, not only at small overlaps where divergence is strongest [9]. In the absence of a clearly defined minimum gap distance, preferably related to real physical constraints, the calculation of maximum electric field strengths around fused structures (dimers or larger) can vary over many orders of magnitude, simply by manipulating the mesh size implemented at the point of intersection. Only one example of fused dimer simulations with clearly defined gap discretizations could be found. Pendry *et al*. used a 1 nm mesh to calculate EM-EF values for a periodic array of fused Ag half-cylinders along a substrate surface. In this case, the mesh was coarse enough to keep enhancements $<50 * E_0$ [39].

It would be useful to also examine EM-EF values of fused dimers given by non-local or quantum models. Unfortunately, such calculations have not been included in reports using these methods. Both absorption [5] and scattering spectra [8] are available, but these are not directly correlated with enhancement. The best available comparison may be the local field values reported for CTP modes of SiO_2/Au core-shell NPs with a variable conductive bridge between them [7]. Local fields in the gap region were 160-250 * E_0, which compares well to the max field value of 180 for the L_{min}= 0.5 nm dimer we consider here. Both values are significantly less than previously reported fields exceeding 1000 * E_0 [1]. The Lumerical FDTD software does not allow incorporation of non-local material models, but researchers with expertise in this area may be interested in carrying out such calculations on dimer antennae.

Comparisons can also be made between theoretical predictions and experiments performed on dimer geometries. The body of work on separated dimers is particularly extensive, with ongoing efforts targeting quantum effects for sub-nanometer gaps [17-18, 20, 40]. The discussion here will be restricted only to experiments with measurements on individual separated or fused dimer nanostructures. Such studies are the most direct way of connecting optical properties to specific geometries. Broadband detection of individual dimer plasmonic resonances has been carried out via optical scattering [2, 24, 41-42] and electron energy loss spectroscopy [10, 43]. These results all show red-shifting BDP modes as gap distances are reduced, and the emergence of lower energy CTP modes near the onset of fusing. Unfortunately, the signals from these techniques for a particular plasmonic mode are not correlated to the EM-EF of that mode. They can be used to identify the presence of plasmon resonances and their energies, but not the associated local field strengths. The disconnect between far-field scattering and near-field enhancement has been well-established through both theory and experiment in the SERS community [44-48].

The only way to definitively quantify enhancement is by measuring it directly using Raman reporter molecules deposited onto nanostructures of interest. Wustholtz *et al.* collected SERS spectra of Au NP dimers and larger aggregates using monochromatic excitation at 632.8 nm [2]. Enhancements were found to vary over roughly two orders of magnitude, but the TEM images of specific dimers were not correlated with optical measurements. Thus, it was impossible to associate the measured enhancements to individual separated or fused structures. Broadband SERS experiments are even more challenging, although a recent example using a supercontinuum source and custom set of tunable filters was provided by Lombardi *et al.* [49]. The best alternative is to measure enhancement at several discrete wavelengths on the same instrument. Only a single experiment of this type has been performed on dimer structures [48], but the resolution of the SEM images was insufficient to discern if individual nanostructures should be categorized as separated or fused. Thus, present experimental data are inconclusive on quantifying the general enhancement of separated vs. fused dimers.

(ii) Varying the surface contact area

When making real plasmonic dimers, the particles will not consist of perfect spheres of uniform size, and electron microscopy images of colloidally grown Au/Ag nanoparticles typically display faceted surfaces [50-53]. When these particles aggregate, the length of the gap or fused segment will vary based on the two particles faces that join [2, 10, 22]. To our knowledge, no previous studies exist on the sensitivity of the dimer plasmon resonances to changes in this surface contact area. Simulations characterizing this effect were performed in terms of a single geometric parameter: the contact length (L_c). **Figures 5.5 and 5.6** provide diagrams defining L_c for both separated and fused dimers. For the separated case, the spheres have one face flattened over a circle of radius L_c, turning the gap region into a thin disc of uniform width. For fused dimers, the flattened sphere surfaces are directly joined.

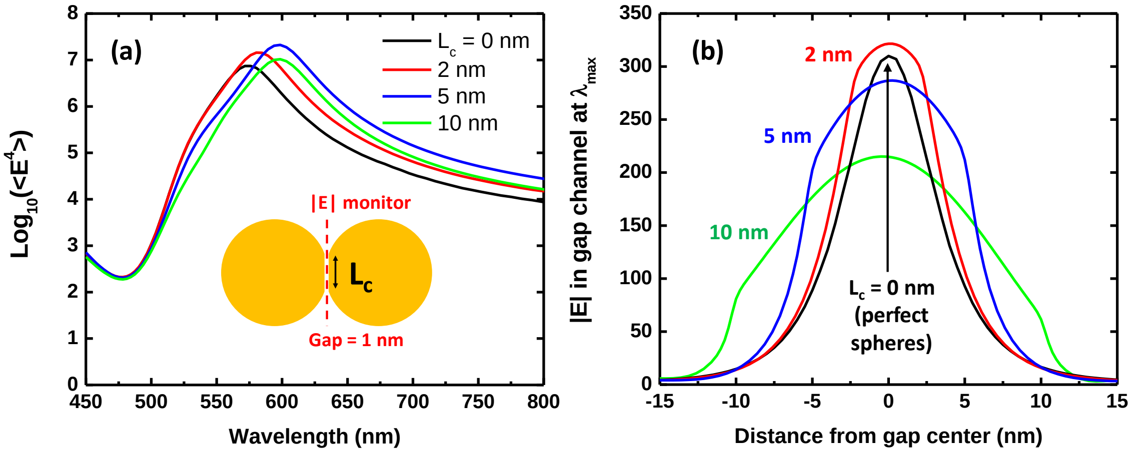

Figure 5.5 Enhancement properties of separated Au dimers as a function of the contact length (L_c). The sphere radii are 25 nm and the gap width is held at a constant value of 1 nm. (a) Broadband EM-EF plots of structures with contact lengths of 0, 2, 5, and 10 nm. The resonant frequency and maximum enhancement values change relatively little. (b) Plots of the electric field strength through the center of the gap region at the BDP resonant λ. Other than an initial uptick between the 0 to 2 nm cases, increasing L_c causes the gap mode volume to expand and the maximum field strength to decrease. These effects partially cancel in the EM-EF calculation, causing the peak values to remain within a factor of 3.

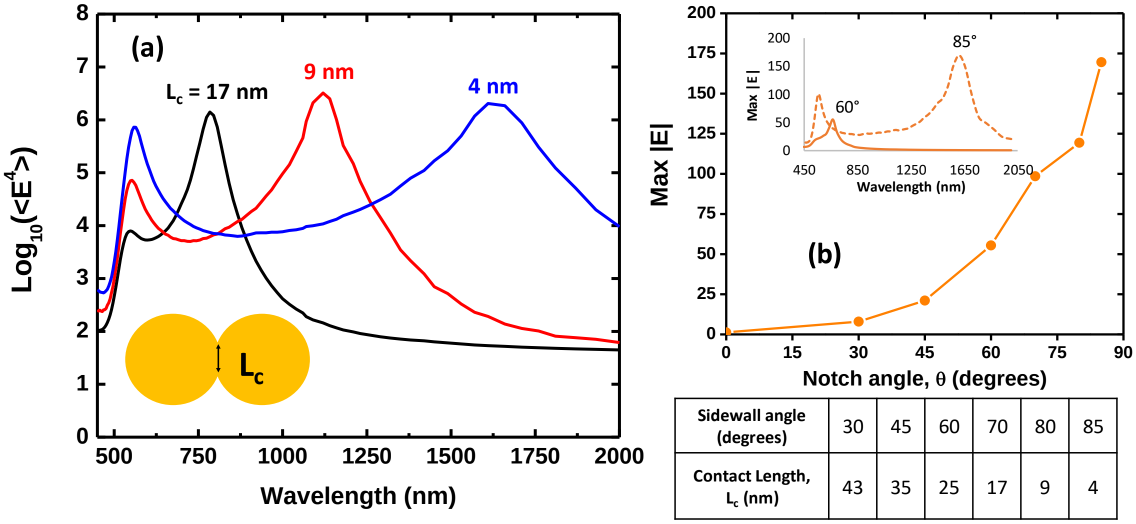

Sidewall angle (degrees)	30	45	60	70	80	85
Contact Length, L_c (nm)	43	35	25	17	9	4

Figure 5.6 Enhancement (EM-EF) and maximum field values for fused dimers as a function of contact length (L_c). Large L_c values correspond to steeper sidewall angles. (a) Decreasing contact length produces larger EM-EF values and CTP modes that are red-shifted into the infrared. (b) Maximum electric field values in the gap region increase with steeper sidewall angles (smaller L_c). Simulation parameters: 50 nm dia. Au spheres with a constant L_{min} value of 1 nm. For reference, the L_{min} = 1 nm fused dimer in Fig. 3 had a sidewall angle of 78° and L_c = 10 nm.

Changing the L_c value affects the separated and fused structure enhancement spectra in drastically different ways. The separated dimers appear relatively insensitive to this parameter. For L_c spanning 0-10 nm, the BDP peak wavelength varies by only 25 nm, and the peak EM-EF values remain within a factor of three [**Fig. 5.5(a)**]. This is somewhat surprising as the electric field profile in the gap region is changing significantly for different L_c [**Fig. 5.5(b)**]. For wider gaps, the peak field intensity decreases, and the fields are extended laterally. These effects partially offset in the EM-EF calculation, as the local $<E^4>$ values are integrated over the entire gap. The 5 nm contact length structure actually yields the largest enhancement value and has a gap field profile with FWHM = 12 nm, almost twice that of the perfect spheres (L_c = 0 nm). Thus, moderate increases in contact area allow the gap electric fields to be moderately decreased without sacrificing enhancement. This may be useful if analyte molecules are sensitive to photodegradation. It should also be noted that the 2D field profile over the disc-shaped gap region is almost perfectly rotationally symmetric, as the dimer sizes are much smaller than optical wavelengths.

In contrast to the relatively constant BDP response of separated dimers, the CTP modes of fused dimers were found to strongly depend on L_c [**Fig. 5.6(a)**]. The low-energy CTP mode shifted from 780 nm all the way to 1630 nm for L_c values of 17 and 4 nm, respectively. The EM-EF peak magnitude changed by <50% during this shift. The high-energy CTP mode, in the visible portion of the spectrum, displayed essentially the opposite behavior, with the peak wavelength changing very little, but the peak EM-EF increasing by almost two orders of magnitude. These trends make sense as the spatial confinement of the low energy CTP in the crevice region is not as great as that of the high-energy mode [**Fig. 5.4**]. This makes the low-energy CTP sensitive to the total surface contour length, which increases for smaller values of L_c, and leads to a red-shift. These same arguments explain the similarities between **Figure 5.6(a)** and **Figure 5.3(b)**, where the surface contour length is also changing as a function of decreasing L_{min} value. The choice of L_c, at a fixed value of L_{min}, uniquely determines the angle that the sphere surfaces make at the bridge point. The maximum gap fields (max |E|), as a function of this angle, are provided over the range of 0-85° in **Figure 5.6(b)**. The inset shows the full spectrum for the 60° and 85° geometries, where a large CTP red-shift is observed. The trends are very similar to those presented in **Figure 5.2(b)** for a two-dimensional notch. Relaxing the geometric constraint that the particles must be spherical (e.g., elliptical) would allow the surface angle, L_{min}, and L_c parameters to vary independently.

(iii) Dielectric encapsulation of plasmonic antennas

Encapsulated plasmonic antennae are useful as SERS tags [51, 54], as enhancers in shell-isolated nanoparticle enhanced Raman spectroscopy [55], and as means of precisely controlling gap distances for the quantitative study of optical enhancement [56-57]. Coatings can be applied after the adsorption of reporter molecules to effectively isolate them from the environment and create an enhancing structure with long shelf-life. Reporter molecules can also diffuse into polymer coatings and reach the metal surface [58]. Here, we focus specifically on dielectric layers that represent oxide or organic coatings. A refractive index of 1.5 was chosen, with the coating applied uniformly over the entire dimer surface. Various coating thicknesses were studied, but the results can be summarized using only two examples, a thin 2 nm coating and a thick 20 nm coating. The difference in EM-EF between a 20 nm coating and an infinite coating, where the simulation background refractive index is $n = 1.5$ everywhere, was found to be only 10%.

It should be emphasized that the electric field values used in the EM-EF calculations are still measured 1 nm from the metal sphere surfaces, which is now within the dielectric. The fields outside the coating are less than those around the corresponding bare metal particle for all coating thicknesses. These conclusions are in agreement with the field profiles around glass-coated Ag nanoparticles previously calculated by Shanthil *et al.* [59]. Hence, dielectric encapsulation is a not a general strategy for increasing the enhancement of SERS structures, but may be beneficial in specific cases where analyte molecules are either trapped inside the coating, can diffuse into the coating, or if the coating itself is optically active.

Figure 5.7 shows the calculated EM-EF values for dielectric-coated separated and fused dimers, along with those of the corresponding bare metal structures. In all cases, coatings cause the plasmon resonances to red-shift. This effect has been previously characterized for a variety of Au nanostructures [60], and is caused by the spatial compression of light within the higher index dielectric material. For the separated spheres, coatings are found to increase EM-EF, with the 20 nm coating yielding an enhancement 10x greater than the bare metal dimer [**Fig. 5.7(a)**]. Surprisingly, this increase does not correspond to a change in the spatial extent of the gap field; the FWHM of the bare and 20 nm coating gap profiles are almost identical at roughly 6 nm. Instead, it is the result of the peak absorption cross-section doubling for the 20 nm coating, indicating that significantly more energy from the excitation plane wave is being coupled into the BDP resonance. This appears to result from the higher polarizability of a dielectric coating such as glass than that of the air or vacuum surroundings otherwise present.

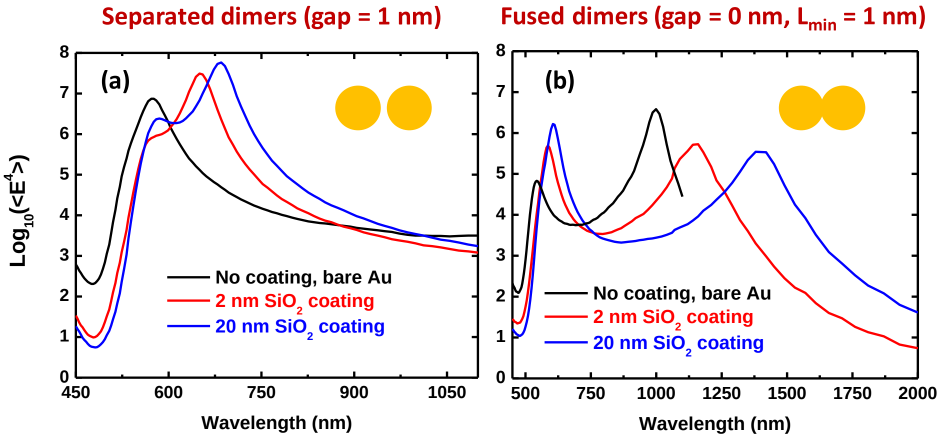

Figure 5.7 EM-EF values for dielectric (n = 1.5) coated Au separated (b) and fused (b) dimers. The coatings represent either SiO2 or polymer encapsulation of the underlying plasmonic structure. The fields used in the EM-EF calculation are recorded 1 nm above the metal surface, which resides within the dielectric.

The difference between the 2 and 20 nm coatings is relatively small, indicating that the presence of dielectric in the gap region is the dominant factor, with the rest of the coating playing only a secondary role. To test this, a simulation was run with a 10 nm dia. dielectric disk filling only the gap region, and the EM-EF profile was indeed found to be almost identical to that of the uniform 2 nm coating. For fused dimers [**Fig. 5.7(b)**], the trend in the peak wavelengths of the CTP-1 and CTP-2 modes are again similar to that shown in **Figure 5.3(b)** and **Figure 5.6(a)**. However, in this case, the surface contour length of the dimers is not changing due to geometric variations. Instead, the wavelength of the plasmon modes along the surface is being spatially compressed by the presence of the higher refractive index dielectric. This allows the surface contour of the same sized dimer to effectively become larger for the same excitation wavelength.

E. Conclusions

The main conclusion from our simulations is that separated dimers produce larger optical field enhancements than comparable fused geometries. Previous reports of fused dimers yielding extraordinary enhancement values are believed to be suspect, due to the use of very fine (<<1 nm) spatial discretization at the region of surface intersection. Classical optical models are prone to field divergence in this type of geometry, with increasingly small discretizations yielding arbitrarily large field values. One method of eliminating these divergence phenomena is to add a metal bridging structure of adjustable diameter that enables direct control of the minimum gap distance. Using physically relevant gap distances in the range of 5-20 Å, maximum local field enhancements of 50-180 were predicted for fused dimers. These modest values agree with the available predictions from more advanced non-local or quantum optical models.

Although fused dimers do not outperform separated dimers in the visible spectrum, they still achieve relatively large enhancements at infrared frequencies. For example, the total Raman enhancement of a fused Au dimer with 5 Å minimum gap distance is roughly 2 orders of magnitude greater than a 300 nm Au nanorod with a plasmon peak of similar wavelength. Wen *et al.* have demonstrated that the low energy charge-transfer plasmon modes of fused structures can be red-shifted even further into the mid-IR spectrum by using spatially elongated metal bridges that produce a dumbbell shape [41]. It should be noted that these structures do not contain the same narrow gaps of the directly fused dimers, so the field enhancements will be significantly lower.

The main barrier to the rational design and production of fused dimer antennae is their sensitivity to geometry. As was discussed at length, the minimum crevice distance, sidewall angle, contact area, and presence of dielectric coatings all strongly modify the charge-transfer plasmon modes of the structures. If a SERS experiment was performed with a sample composed of a distribution of fused geometries, the expectation is that broadband optical enhancement would be observed across the entire visible and near-infrared spectrum. Experimental measurements of enhancement spectra from individual nanostructures remain challenging, in part due to the difficulty of performing broadband optical Raman experiments. As instrumentation improves and these capabilities improve, more quantitative comparisons between theory and experimental enhancements will be possible, and antenna geometries can be more precisely characterized and optimized to yield maximum enhancements over a range of energies.

References

1. McMahon, J. M.; Henry, A.-I.; Wustholz, K. L.; Natan, M. J.; Freeman, R. G.; Van Duyne, R. P.; Schatz, G. C. Gold Nanoparticle Dimer Plasmonics: Finite Element Method Calculations of the Electromagnetic Enhancement to Surface-Enhanced Raman Spectroscopy. *Analytical and bioanalytical chemistry* **2009**, *394*, 1819-1825.
2. Wustholz, K. L.; Henry, A.-I.; McMahon, J. M.; Freeman, R. G.; Valley, N.; Piotti, M. E.; Natan, M. J.; Schatz, G. C.; Duyne, R. P. V. Structure− Activity Relationships in Gold Nanoparticle Dimers and Trimers for Surface-Enhanced Raman Spectroscopy. *Journal of the American Chemical Society* **2010**, *132*, 10903-10910.
3. McMahon, J. M.; Li, S.; Ausman, L. K.; Schatz, G. C. Modeling the Effect of Small Gaps in Surface-Enhanced Raman Spectroscopy. *The Journal of Physical Chemistry C* **2011**, *116*, 1627-1637.
4. Kottmann, J. P.; Martin, O. J. Plasmon Resonant Coupling in Metallic Nanowires. *Optics Express* **2001**, *8*, 655-663.
5. Marinica, D.; Kazansky, A.; Nordlander, P.; Aizpurua, J.; Borisov, A. Quantum Plasmonics: Nonlinear Effects in the Field Enhancement of a Plasmonic Nanoparticle Dimer. *Nano letters* **2012**, *12*, 1333-1339.
6. Zuloaga, J.; Prodan, E.; Nordlander, P. Quantum Description of the Plasmon Resonances of a Nanoparticle Dimer. *Nano letters* **2009**, *9*, 887-891.
7. Pérez-González, O.; Zabala, N.; Borisov, A.; Halas, N.; Nordlander, P.; Aizpurua, J. Optical Spectroscopy of Conductive Junctions in Plasmonic Cavities. *Nano letters* **2010**, *10*, 3090-3095.
8. Esteban, R.; Borisov, A. G.; Nordlander, P.; Aizpurua, J. Bridging Quantum and Classical Plasmonics with a Quantum-Corrected Model. *Nature communications* **2012**, *3*, 825.
9. Romero, I.; Aizpurua, J.; Bryant, G. W.; De Abajo, F. J. G. Plasmons in Nearly Touching Metallic Nanoparticles: Singular Response in the Limit of Touching Dimers. *Optics express* **2006**, *14*, 9988-9999.
10. Scholl, J. A.; García-Etxarri, A.; Koh, A. L.; Dionne, J. A. Observation of Quantum Tunneling between Two Plasmonic Nanoparticles. *Nano letters* **2013**, *13*, 564-569.
11. Bain, A.; Chandna, P.; Butcher, G.; Bryant, J. Picosecond Polarized Fluorescence Studies of Anisotropic Fluid Media. Ii. Experimental Studies of Molecular Order and Motion in Jet Aligned Rhodamine 6g and Resorufin Solutions. *The Journal of Chemical Physics* **2000**, *112*, 10435-10449.
12. Toscano, G.; Raza, S.; Jauho, A.-P.; Mortensen, N. A.; Wubs, M. Modified Field Enhancement and Extinction by Plasmonic Nanowire Dimers Due to Nonlocal Response. *Optics express* **2012**, *20*, 4176-4188.
13. Khurgin, J.; Tsai, W.-Y.; Tsai, D. P.; Sun, G. Landau Damping and Limit to Field Confinement and Enhancement in Plasmonic Dimers. *ACS Photonics* **2017**, *4,* 2871-2880.
14. Garcia de Abajo, F. J. Nonlocal Effects in the Plasmons of Strongly Interacting Nanoparticles, Dimers, and Waveguides. *The Journal of Physical Chemistry C* **2008**, *112*, 17983-17987.
15. Mortensen, N. A.; Raza, S.; Wubs, M.; Søndergaard, T.; Bozhevolnyi, S. I. A Generalized Non-Local Optical Response Theory for Plasmonic Nanostructures. *Nature communications* **2014**, *5*, 3809.

16. Christensen, T.; Yan, W.; Jauho, A.-P.; Soljačić, M.; Mortensen, N. A. Quantum Corrections in Nanoplasmonics: Shape, Scale, and Material. *Physical review letters* **2017**, *118*, 157402.
17. Liu, P.; Chulhai, D. V.; Jensen, L. Single-Molecule Imaging Using Atomistic near-Field Tip-Enhanced Raman Spectroscopy. *ACS nano* **2017**, *11*, 5094-5102.
18. Barbry, M.; Koval, P.; Marchesin, F.; Esteban, R.; Borisov, A.; Aizpurua, J.; Sánchez-Portal, D. Atomistic near-Field Nanoplasmonics: Reaching Atomic-Scale Resolution in Nanooptics. *Nano letters* **2015**, *15*, 3410-3419.
19. Ward, D. R.; Hüser, F.; Pauly, F.; Cuevas, J. C.; Natelson, D. Optical Rectification and Field Enhancement in a Plasmonic Nanogap. *Nature nanotechnology* **2010**, *5*, 732.
20. Natelson, D.; Li, Y.; Herzog, J. B. Nanogap Structures: Combining Enhanced Raman Spectroscopy and Electronic Transport. *Physical Chemistry Chemical Physics* **2013**, *15*, 5262-5275.
21. Zhang, Y.; Voronine, D. V.; Qiu, S.; Sinyukov, A. M.; Hamilton, M.; Liege, Z.; Sokolov, A. V.; Zhang, Z.; Scully, M. O. Improving Resolution in Quantum Subnanometre-Gap Tip-Enhanced Raman Nanoimaging. *Scientific reports* **2016**, *6*, 25788.
22. Zhu, W.; Crozier, K. B. Quantum Mechanical Limit to Plasmonic Enhancement as Observed by Surface-Enhanced Raman Scattering. *Nature communications* **2014**, *5*, 5228.
23. Sanders, A.; Bowman, R. W.; Baumberg, J. J. Tracking Optical and Electronic Behaviour of Quantum Contacts in Sub-Nanometre Plasmonic Cavities. *Scientific reports* **2016**, *6*, 32988.
24. Savage, K. J.; Hawkeye, M. M.; Esteban, R.; Borisov, A. G.; Aizpurua, J.; Baumberg, J. J. Revealing the Quantum Regime in Tunnelling Plasmonics. *Nature* **2012**, *491*, 574.
25. García-Martín, A.; Ward, D. R.; Natelson, D.; Cuevas, J. C. Field Enhancement in Subnanometer Metallic Gaps. *Physical Review B* **2011**, *83*, 193404.
26. Di Vece, M. Very Long Plasmon Oscillation Lifetimes in the Gap between Two Gold Particles. *Plasmonics* **2017**, 1-5.
27. Lassiter, J. B.; Aizpurua, J.; Hernandez, L. I.; Brandl, D. W.; Romero, I.; Lal, S.; Hafner, J. H.; Nordlander, P.; Halas, N. J. Close Encounters between Two Nanoshells. *Nano letters* **2008**, *8*, 1212-1218.
28. Long, J.; Yi, H.; Li, H.; Lei, Z.; Yang, T. Reproducible Ultrahigh Sers Enhancement in Single Deterministic Hotspots Using Nanosphere-Plane Antennas under Radially Polarized Excitation. *Scientific reports* **2016**, *6*, 33218.
29. Porto, J.; Johansson, P.; Apell, S.; Lopez-Rios, T. Resonance Shift Effects in Apertureless Scanning near-Field Optical Microscopy. *Physical Review B* **2003**, *67*, 085409.
30. Palik, E. D., *Handbook of Optical Constants of Solids*; Elsevier, 1997; Vol. I-III.
31. Dong, T.; Ma, X.; Mittra, R. Optical Response in Subnanometer Gaps Due to Nonlocal Response and Quantum Tunneling. *Applied Physics Letters* **2012**, *101*, 233111.
32. Xu, H.; Bjerneld, E. J.; Aizpurua, J.; Apell, P.; Gunnarsson, L.; Petronis, S.; Kasemo, B.; Larsson, C.; Hook, F.; Kall, M. In *Interparticle Coupling Effects in Surface-Enhanced Raman Scattering*, Nanoparticles and Nanostructured Surfaces: Novel Reporters with Biological Applications, International Society for Optics and Photonics: 2001; pp 35-43.
33. Huang, Y.; Zhou, Q.; Hou, M.; Ma, L.; Zhang, Z. Nanogap Effects on near-and Far-Field Plasmonic Behaviors of Metallic Nanoparticle Dimers. *Physical Chemistry Chemical Physics* **2015**, *17*, 29293-29298.
34. Moskovits, M. Persistent Misconceptions Regarding Sers. *Physical Chemistry Chemical Physics* **2013**, *15*, 5301-5311.
35. Valley, N.; Greeneltch, N.; Van Duyne, R. P.; Schatz, G. C. A Look at the Origin and Magnitude of the Chemical Contribution to the Enhancement Mechanism of Surface-Enhanced Raman Spectroscopy (Sers): Theory and Experiment. *The Journal of Physical Chemistry Letters* **2013**, *4*, 2599-2604.
36. Kerker, M.; Wang, D.-S.; Chew, H. Surface Enhanced Raman Scattering (Sers) by Molecules Adsorbed at Spherical Particles: Errata. *Applied optics* **1980**, *19*, 4159-4174.

37. Ausman, L. K.; Schatz, G. C. On the Importance of Incorporating Dipole Reradiation in the Modeling of Surface Enhanced Raman Scattering from Spheres. *The Journal of chemical physics* **2009**, *131*, 084708.
38. Lynch, D. W.; Hunter, W., -Comments on the Optical Constants of Metals and an Introduction to the Data for Several Metals. In *Handbook of Optical Constants of Solids*, Elsevier: 1997; pp 275-367.
39. García-Vidal, F. J.; Pendry, J. Collective Theory for Surface Enhanced Raman Scattering. *Physical Review Letters* **1996**, *77*, 1163.
40. Urbieta, M.; Barbry, M.; Zhang, Y.; Koval, P.; Sánchez-Portal, D.; Zabala, N.; Aizpurua, J. Atomic-Scale Lightning Rod Effect in Plasmonic Picocavities: A Classical View to a Quantum Effect. *ACS nano* **2018**.
41. Wen, F.; Zhang, Y.; Gottheim, S.; King, N. S.; Zhang, Y.; Nordlander, P.; Halas, N. J. Charge Transfer Plasmons: Optical Frequency Conductances and Tunable Infrared Resonances. *ACS nano* **2015**, *9*, 6428-6435.
42. Atay, T.; Song, J.-H.; Nurmikko, A. V. Strongly Interacting Plasmon Nanoparticle Pairs: From Dipole− Dipole Interaction to Conductively Coupled Regime. *Nano letters* **2004**, *4*, 1627-1631.
43. Koh, A. L.; Bao, K.; Khan, I.; Smith, W. E.; Kothleitner, G.; Nordlander, P.; Maier, S. A.; McComb, D. W. Electron Energy-Loss Spectroscopy (Eels) of Surface Plasmons in Single Silver Nanoparticles and Dimers: Influence of Beam Damage and Mapping of Dark Modes. *ACS nano* **2009**, *3*, 3015-3022.
44. Huang, S.; Ming, T.; Lin, Y.; Ling, X.; Ruan, Q.; Palacios, T.; Wang, J.; Dresselhaus, M.; Kong, J. Ultrasmall Mode Volumes in Plasmonic Cavities of Nanoparticle-on-Mirror Structures. *Small* **2016**, *12*, 5190-5199.
45. Litz, J. P.; Camden, J. P.; Masiello, D. J. Spatial, Spectral, and Coherence Mapping of Single-Molecule Sers Active Hot Spots Via the Discrete-Dipole Approximation. *The Journal of Physical Chemistry Letters* **2011**, *2*, 1695-1700.
46. Doherty, M. D.; Murphy, A.; McPhillips, J.; Pollard, R. J.; Dawson, P. Wavelength Dependence of Raman Enhancement from Gold Nanorod Arrays: Quantitative Experiment and Modeling of a Hot Spot Dominated System. *The Journal of Physical Chemistry C* **2010**, *114*, 19913-19919.
47. Le Ru, E.; Galloway, C.; Etchegoin, P. On the Connection between Optical Absorption/Extinction and Sers Enhancements. *Physical Chemistry Chemical Physics* **2006**, *8*, 3083-3087.
48. Kleinman, S. L.; Sharma, B.; Blaber, M. G.; Henry, A.-I.; Valley, N.; Freeman, R. G.; Natan, M. J.; Schatz, G. C.; Van Duyne, R. P. Structure Enhancement Factor Relationships in Single Gold Nanoantennas by Surface-Enhanced Raman Excitation Spectroscopy. *Journal of the American Chemical Society* **2012**, *135*, 301-308.
49. Lombardi, A.; Demetriadou, A.; Weller, L.; Andrae, P.; Benz, F.; Chikkaraddy, R.; Aizpurua, J.; Baumberg, J. J. Anomalous Spectral Shift of near-and Far-Field Plasmonic Resonances in Nanogaps. *ACS photonics* **2016**, *3*, 471-477.
50. Xu, H.; Aizpurua, J.; Käll, M.; Apell, P. Electromagnetic Contributions to Single-Molecule Sensitivity in Surface-Enhanced Raman Scattering. *Physical Review E* **2000**, *62*, 4318.
51. Wang, Y.; Yan, B.; Chen, L. Sers Tags: Novel Optical Nanoprobes for Bioanalysis. *Chemical reviews* **2012**, *113*, 1391-1428.
52. Wei, H.; Xu, H. Hot Spots in Different Metal Nanostructures for Plasmon-Enhanced Raman Spectroscopy. *Nanoscale* **2013**, *5*, 10794-10805.
53. Sergiienko, S.; Moor, K.; Gudun, K.; Yelemessova, Z.; Bukasov, R. Nanoparticle–Nanoparticle Vs. Nanoparticle–Substrate Hot Spot Contributions to the Sers Signal: Studying Raman Labelled Monomers, Dimers and Trimers. *Physical Chemistry Chemical Physics* **2017**, *19*, 4478-4487.

54. Shen, W.; Lin, X.; Jiang, C.; Li, C.; Lin, H.; Huang, J.; Wang, S.; Liu, G.; Yan, X.; Zhong, Q. Reliable Quantitative Sers Analysis Facilitated by Core–Shell Nanoparticles with Embedded Internal Standards. *Angewandte Chemie International Edition* **2015**, *54*, 7308-7312.
55. Anema, J. R.; Li, J.-F.; Yang, Z.-L.; Ren, B.; Tian, Z.-Q. Shell-Isolated Nanoparticle-Enhanced Raman Spectroscopy: Expanding the Versatility of Surface-Enhanced Raman Scattering. *Annual Review of Analytical Chemistry* **2011**, *4*, 129-150.
56. Taylor, R. W.; Lee, T.-C.; Scherman, O. A.; Esteban, R.; Aizpurua, J.; Huang, F. M.; Baumberg, J. J.; Mahajan, S. Precise Subnanometer Plasmonic Junctions for Sers within Gold Nanoparticle Assemblies Using Cucurbit [N] Uril "Glue". *Acs Nano* **2011**, *5*, 3878-3887.
57. Lee, H.; Kim, G.-H.; Lee, J.-H.; Kim, N. H.; Nam, J.-M.; Suh, Y. D. Quantitative Plasmon Mode and Surface-Enhanced Raman Scattering Analyses of Strongly Coupled Plasmonic Nanotrimers with Diverse Geometries. *Nano Lett* **2015**, *15*, 4628-4636.
58. Braun, G. B.; Lee, S. J.; Laurence, T.; Fera, N.; Fabris, L.; Bazan, G. C.; Moskovits, M.; Reich, N. O. Generalized Approach to Sers-Active Nanomaterials Via Controlled Nanoparticle Linking, Polymer Encapsulation, and Small-Molecule Infusion. *The Journal of Physical Chemistry C* **2009**, *113*, 13622-13629.
59. Shanthil, M.; Thomas, R.; Swathi, R.; George Thomas, K. Ag@ Sio2 Core–Shell Nanostructures: Distance-Dependent Plasmon Coupling and Sers Investigation. *The Journal of Physical Chemistry Letters* **2012**, *3*, 1459-1464.
60. Miller, M. M.; Lazarides, A. A. Sensitivity of Metal Nanoparticle Surface Plasmon Resonance to the Dielectric Environment. *The Journal of Physical Chemistry B* **2005**, *109*, 21556-21565.

Appendix (A5)

A5.1 Calculating global Raman enhancement factors (<E^4>)

Estimating the electromagnetic enhancement factor (EM-EF) requires the electric field values at every point where analyte is expected to be present, in this case over the entire surface of the dimer structure. As discussed in the main text, the fourth power of the local electric field will be used to estimate the near-field Raman enhancement. This calculation is only technically correct for point dipoles near a spherical antenna with a Stokes shift of zero for the scattered radiation [1]. Despite these approximations, the E^4 calculation method is the accepted standard for analysis of enhancing structures.

We follow the procedure of McMahon *et al.* [2] in computing EM-EF using a surface integral. The first step in the calculation is choosing the surface offset distance at which the fields will be sampled. This is somewhat arbitrary, but we have used a value of 1 nm. A complicating factor is that the dimer structures investigated here contain very small gaps, where a surface offset of 1 nm is larger than the entire gap width. To account for this, field values in gap regions, defined as those below the point of intersection of the standard 1 nm offset contours, are always recorded at the center of the gap. As is shown in Appendix A5.3, the gap regions dominate the EM-EF calculation, making the results fairly insensitive to the surface offset value chosen. For example, the largest difference in EM-EF for a 1 nm gap, separated dimer between surface offsets of 0.5 nm and 1 nm is only 3%.

The Lumerical FDTD software does not currently support the direct implementation of curved field monitors that could be placed over the surface of the spheres. One solution is to record the field values in the entire 3D volume of a box encompassing the dimer, and then extract the desired fields from the surface only. Unfortunately, the small mesh size needed for convergence of these simulations (0.25 nm or less), and the 101 separate wavelengths recorded to capture the broadband response of the structures, lead the data output size of the required 3D field monitor to become unwieldy.

A solution to this problem was found when it was observed that the dimer field profiles in the plane normal to the incident polarization were nearly radially symmetric. This occurs for two reasons. The first is that the dimer dimensions (sphere dia. = 50 nm) are much less than the wavelengths of the excitation radiation considered (>450 nm). This causes retardation effects to be minimal. The second reason is that the incident plane wave is linearly polarized along the inter-sphere axis, making the resultant fields symmetric with respect to the dimer geometry. Tests were then performed to ascertain if a single 2D plane monitor cutting through the center of the dimer structures could be used to give a very accurate approximation of the fields over the entire surface of the sphere. Simulations were run with fields recorded by several 2D plane monitors cutting the spheres at different locations [Fig. A5.1].

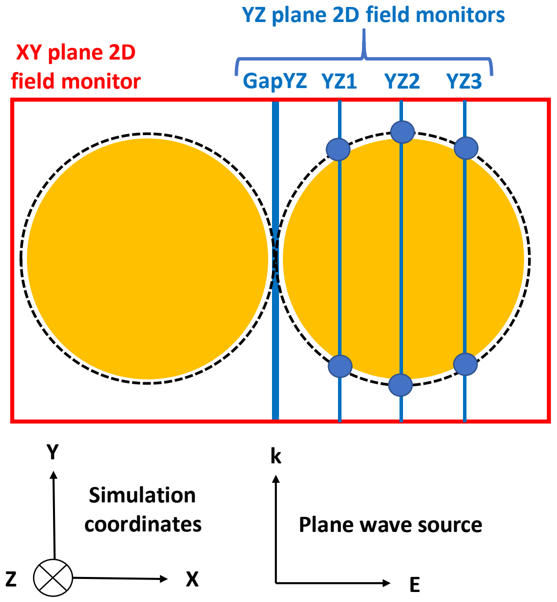

Figure A5.1 Diagram of the field monitors used to compute <E^4> values over the surface of the dimer structures. It was found that using only the field values from a single XY plane through the center of the spheres **(red)** gave a very accurate approximation of the total fields around the sphere surface **(blue YZ monitors)**.

The fields around the surface of the sphere at the location of each monitor in the YZ plane were calculated using two procedures. The more accurate method averaged all the field values around the sphere circumference given by a YZ monitor. The second method only averaged the field data from two points in the YZ monitor, those intersecting the XY plane. If the second method was found to give approximately the same values as the first, then it could be concluded that a single XY monitor through the center of the dimers would be sufficient for EM-EF calculations.

Figures A5.2 and A5.3 compare the results of the two field averaging procedures applied to a typical separated or fused dimer for each of the four YZ plane monitors. It is clear that the differences between the two methods are very small in all cases, with typical discrepancies <1%. The only exception is the GapYZ monitor for the fused dimer [Fig. A5.3], where the differences are large enough to yield a 10-20% in the $<E^4>$ values. For this reason, data were recorded for the GapYZ plane monitor in the case of all fused dimer simulations, and the complete monitor data were then used to calculate EM-EF. The final result of this simplified analysis procedure is that both <E> and $<E^4>$ values can be computed over the surfaces of the separated and fused dimers with data output sizes <500 MB and almost no decrease in the accuracy of the calculations.

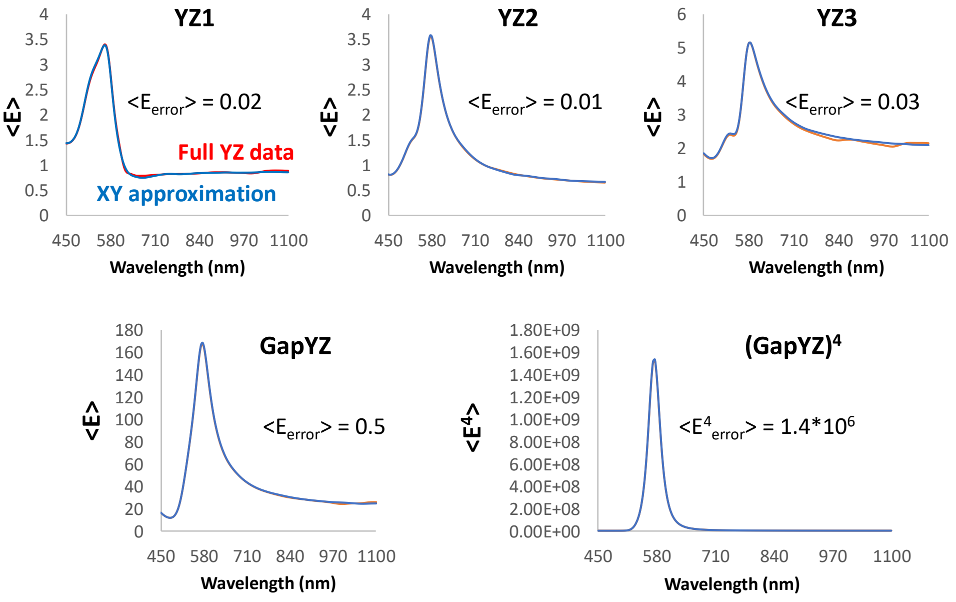

Figure A5.2 Average surface electric field values for a separated dimer (1 nm gap) calculated using the monitors shown in Figure A5.1. The blue curves use data from 2D plane monitors in the YZ plane, while the red curves only use data from a single XY plane monitor. The relative difference between the two methods is <1% for all of the monitor positions and field values computed.

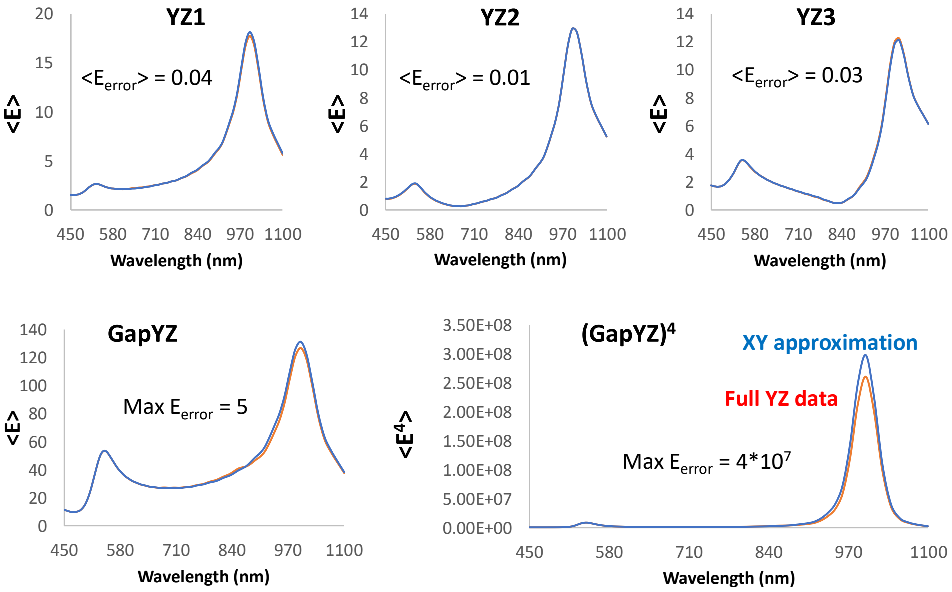

Figure A5.3 Average surface electric field values for a fused dimer (0 nm overlap, 1 nm L_{min}) calculated using the monitors shown in Figure A5.1. The blue curves use data from 2D plane monitors in the YZ plane, while the red curves only use data from a single XY plane monitor. The largest errors are for the gap $<E^4>$ values where the methods differ by about 10% at certain wavelengths. For this reason, GapYZ monitors are included for all the fused structures and used to compute the $<E^4>$ values reported in Figure 5.2 of the main text.

A5.2 Field enhancements of Au cylinders

The computational requirements for simulating 3D spheres with very small gaps became prohibitive as the gap distances approached 5 Å. Identical simulations were performed in a 2D FDTD environment, modeling parallel Au cylinders. The minimum gap distances could then be reduced to 1.25 Å. The maximum EM-EFs for both the separated and fused dimers were found to increase over the entire range of gap distances studied [Fig. A5.4]. The maximum local fields were well fit by a power law relationship of the form: $|E| \sim 1/gap^n$ with exponent values of n=1.15 and n=1.09 for the separated and fused dimers, respectively. This field scaling is very similar to that of the notch geometry results presented in Figure 5.2(a) of the main text.

It is also worth noting the differences between the 2D results and the corresponding 3D data shown in Figure 5.3 of the main text. One trend is that, at equal gap or L_{min} distances, the EM-EFs of the cylinders are smaller by 1-2 orders of magnitude than the sphere results. This is because the cylinder surfaces have curvature over only a single spatial axis, as opposed to the two axes of the spheres. The higher local curvature of the spheres creates more confined and intense gap fields, a type of geometric field enhancement termed the “lightning rod effect” in the near-field optics literature. Additionally, the cylinder plasmon resonances are blue-shifted relative to those of spheres. For example, the enhancement λ_{max} of the 0.5 nm separated cylinder dimer is 578 nm, compared to 611 nm for the similar sphere dimer.

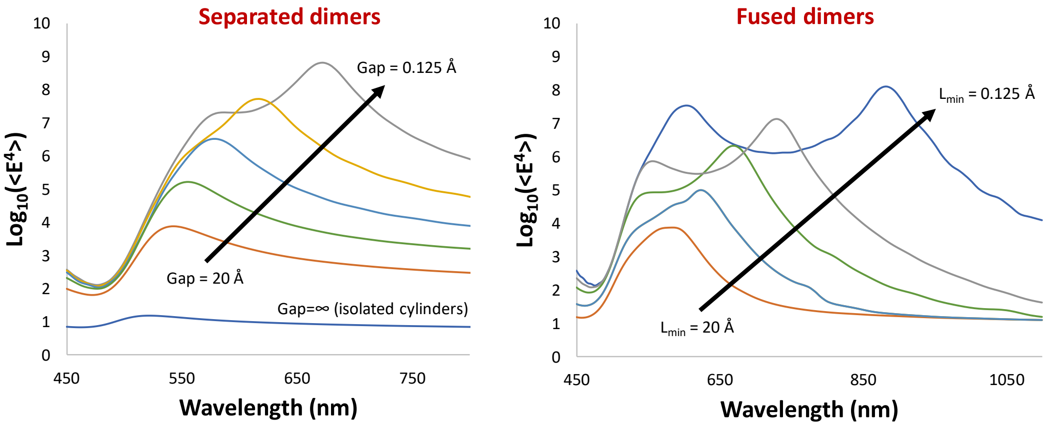

Figure A5.4 EM-EF calculations for separated and fused Au cylinders for gap distances of 20, 10, 5, 2.5, and 1.25 Å. The monotonic increase in enhancement with decreasing gap/L_{min} distance is a symptom of the field divergence present when studying these structures with classical optical models.

Appendix 5 References

1. Kerker, M.; Wang, D.-S.; Chew, H. Surface Enhanced Raman Scattering (Sers) by Molecules Adsorbed at Spherical Particles: Errata. *Applied optics* **1980**, *19*, 4159-4174.
2. McMahon, J. M.; Henry, A.-I.; Wustholz, K. L.; Natan, M. J.; Freeman, R. G.; Van Duyne, R. P.; Schatz, G. C. Gold Nanoparticle Dimer Plasmonics: Finite Element Method Calculations of the Electromagnetic Enhancement to Surface-Enhanced Raman Spectroscopy. *Analytical and bioanalytical chemistry* **2009**, *394*, 1819-1825.

SUMMARY

This work described the operating principles and theory of tip-enhanced near-field optical microscopy (TENOM) as a flexible method of surface characterization, capable of extending optical spectroscopy to true nanoscale dimensions. The general principle of coupling radiation to a nanoscale antenna has found applications across a wide range of energy scales (UV-Vis-IR), and when combined with the many variants of scanning probe microscopy (mechanical, electrical, magnetic, etc.), the combined optical and physical characterization capabilities of these instruments are useful across many disciplines.

Chapter 2 presented the design, construction, and experimental validation of a TENOM instrument that combines a commercial optical microscope with a custom-built shear-force atomic force microscope. Relevant instrument performance metrics including the optical microscope point-spread-function, atomic force microscope noise floor, and thermal stability of the full system were measured. Unambiguous enhancement of near-field optical signals was verified through multiple experiments: tip up-down tests with coumarin-6 dye molecules, optical signal scaling with probe-sample distance, and chemical imaging of patterned copper phthalocyanine films at spatial resolutions <50 nm ($<\lambda/10$).

In Chapter 3, these efforts were extended to study the more complex optical properties of metal-free phthalocyanine (H_2Pc). Exciton-coupling between adjacent H_2Pc molecules leads to changes in the energy and intensity of the molecular fluorescence. The TENOM instrument was used to simultaneously collect spatially correlated fluorescence, Raman, and topographic data from a patterned H_2Pc film, and these measurements allowed the aggregation state of molecules to be mapped, with nanoscale spatial resolution, across a wide range of surface coverages including isolated molecules, dimers, and continuous films.

Chapter 4 presented work using finite-difference time-domain (FDTD) simulations to study the fundamental optical physics of antenna nanostructures. Tuning the optical properties of support structures with attached plasmonic nanocavities was shown to be critical for either enhancing or quenching local field strengths, with materials possessing low extinction coefficients demonstrating superior performance. A quantitative comparative study of several proposed near-field antenna designs was also carried out, with architectures fabricated using focused ion-beam milling of the antenna apex identified as the most promising. FDTD simulations were also used in Chapter 5 to study pairs of plasmonic nanoparticles relevant for surface-enhanced Raman spectroscopy applications. It was shown that previous work on this system significantly over-predicted field enhancements due to numerical effects present at nano-gap features. Metal bridging structures were used to halt the field divergence at physically relevant lengths scales, allowing accurate study of experimentally relevant parameters including the fused contact area and presence of a dielectric encapsulation layer.

Advancements across multiple fields are helping to push the TENOM technique forward. Improvements in high-intensity broadband laser sources will enable flexible measurement of both the electronic and vibrational structure of materials, and general improvements in nano-manufacturing are expected to reduce the time and cost of producing high-enhancement resonant antennae with well-defined plasmonic structure. The future is bright for TENOM to find use as a versatile optical and physical surface characterization technique.